ABSTRACT

Title of dissertation: QUANTUM IMPURITY REGIME OF
CIRCUIT QUANTUM ELECTRODYNAMICS

Nitish Jitendrakumar Mehta, Doctor of Philosophy, 2022

Dissertation directed by: Professor Vladimir E Manucharyan
Department of Physics

In this thesis we describe a novel regime of cavity quantum electrodynamics, where a single atom is coupled to a multi-mode Fabry-Perot cavity with a strength much larger than its free spectral range. In this regime, the atom acting as a quantum impurity mediates interactions between many-body states of radiation in the multi-mode cavity. This novel regime of cavity QED is experimentally realized by coupling superconducting artificial atoms to a high impedance 1-D superconducting transmission line cavity. We study the problem of single photon decay in these strongly non-linear cavities with discrete energy levels. By engineering the properties of the artificial atoms, we alter interaction and connectivity between many-body states of radiation, and we observe two distinct effects. For the case of a multi-mode Fabry-Perot coupled to a fluxonium artificial atom, the interactions mediated by the atom attempts to down convert a single photon into many low frequency photons but fails because of limited connectivity in the many-body Fock space. This phenomenon of many-body localization of radiation gives rise to striking spectral features where a single standing wave resonance of the cavity is replaced by a fine structure of satellite peaks. On the other hand, for the case of a transmon coupled galvanically to the cavity, the interaction splits a single photon at high energy into a shower of odd number of lower energy photons. In this case the single standing wave resonance of the cavity acquires a shorter lifetime which can be calculated using Fermi's

golden rule and matches our theoretical model without any adjustable parameters.

QUANTUM IMPURITY REGIME OF CIRCUIT QUANTUM ELECTRODYNAMICS

by

Nitish Jitendrakumar Mehta

Dissertation submitted to the Faculty of the Graduate School of the
University of Maryland, College Park in partial fulfillment
of the requirements for the degree of
Doctor of Philosophy
2022

Dissertation Committee:
Professor Vladimir E. Manucharyan, Advisor
Professor Alicia Kollár
Professor Alexey Gorshkov
Professor Victor Yakovenko
Professor Andrew Childs, Dean's Representative

Acknowledgments

During the course of my graduate career at UMD, I have had the pleasure to interact with and learn from a wide range of people with diverse backgrounds and I have greatly benefited from their support, wisdom and guidance. So, it is my pleasure to start this thesis by acknowledging my gratitude to all the incredible people who have made this thesis possible.

I would like to begin by thanking my advisor, Professor Vladimir Manucharyan for giving me the invaluable opportunity to work in the superconducting circuits lab at UMD. I will forever be grateful for the time, energy and patience with which Vlad taught me everything there is to know about becoming a good scientist. From fundamental concepts in physics to the right choice of colors in a paper plot. Some of my most fond memories of graduate school have been the times when we discussed physics in his office (and later during COVID on Zoom). It is impossible to understate his impact on the work described in this thesis and the impact, he has had on me as a scientist.

I am also very grateful to Professor Cristiano Ciuti, who has gradually become my second (theory) advisor during our two years of collaboration. Cristiano was a constant companion in the long and often frustrating road to come up with the theory for the fluxonium impurity experiments described in chapter 5. Cristiano taught me the nuances of condensed matter theory and offered me tremendous help throughout the project. He also rescued me numerous times when I got stuck in calculations.

Thanks are due to Professor Alicia Kollar, Professor Alexey Gorshkov, Professor Victor Yakovenko,

and Professor Andrew Childs for agreeing to serve on my thesis committee and for sparing their invaluable time reviewing the manuscript. I would especially like to thank Professor Yakovenko and Professor Gorshkov on joining the committee on a short notice.

With a separate paragraph I would like to thank Dr. Roman Kuzmin who was my direct mentor in the lab. All the projects described in this thesis have been done in either direct guidance or collaboration with Roman. I will forever be grateful to Roman for teaching me everything from theoretical calculations about quantum impurity models to operating the dilution refrigerator and being patient even when I made mistakes repeatedly. I hope in the future I can adopt the methodical and thorough approach towards science that Roman epitomizes.

My colleagues at the Superconducting Circuits laboratory (both past and present) have contributed to this work in many ways, they deserve a special mention. I would like to thank Nick Grabon and Ray Mencia for fabricating a subset of the devices described in this thesis and for training me in the dark arts of nanofabrication. On the fabrication side, I am also thankful of Natalia Pankratova who devised the original recipe to make Josephson junction arrays in our lab. I would like to thank postdoc Dr. Ivan Pechenezhskiy for our numerous discussions on my projects and also writing the superconducting circuits simulation python package. It was only because of your initial code base that I was able to simulate the spectra for more complicated circuits later in my PhD. I thank Dr. Yen-Hsiang Lin and Haonan Xiong for designing the 3-D waveguide sample holder used in this work. It was an absolute pleasure to work closely with Aaron on the Spin chain project in the last half of my PhD. Although I did not work directly with Nathaneal Cottet, Long Nuygen, and Hanho Lee, it was always fun to learn about their experiments in the lab, that helped me broaden my vision.

I would also like to acknowledge help and support from the administrative staff of the Physics department especially Josiland Chambers. She was incredibly kind and patient and helped me

navigate all the administrative tasks right from starting my PhD to defense. I would be lost without her help.

Outside of UMD, I would like to thank Professor Vijayraghavan at TIFR, who gave me, a confused electrical engineering and physics undergrad a chance to work in his lab without prior research experience. Vijay was also the person who introduced me to the fascinating world of circuit QED and connected me to Vlad. In retrospect his advice of coming to Maryland and joining Vlad's group was easily one of the best pieces of advice I have received.

I owe my deepest thanks to my family - my brother, my mother and my father who have always stood by me and guided me through my career. Words cannot express the gratitude I owe them. To my loving wife, Aggie, thank you for your support and being by my side, it was a pleasure to go on this graduate school journey with you. I cannot imagine finishing this PhD without my family and I dedicate this thesis to you all.

Contents

List of Figures

List of Tables

Nomenclatures

Abbreviations

1-D	One dimensional
AC	Alternating current
cQED	Circuit quantum electrodynamics
dB	decibels
DC	Direct current
FSR	Free spectral range
GHz	gigahertz
HEMT	High Electron Mobility Transistor
IPA	Isopropyl Alcohol
MBL	many-body localization
MMA	Methyl methacrylate
PMMA	Poly (methyl methacrylate)

SEM Scanning electron microscope

SQuID Superconducting quantum interference device

VNA Vector network analyzer

Physical constants

ϵ_0 Vacuum permittivity

$\hbar$ Reduced Planck constant

μ_0 Vacuum premeability

Φ_0 Magnetic flux quantum

c Speed of light in vacuum

e Electron charge

h Planck constant

k_B Boltzman constant

R_Q Resistance quantum

Symbols

χ_{ij} Cross-Kerr interaction between cavity mode i, j

Δ Free spectral range of Fabry-Perot cavity

$\Delta^{(3)}$ Spacing of 3-particle states in a Fabry-Perot cavity

$\Delta^{(5)}$ Spacing of 5-particle states in a Fabry-Perot cavity

ℓ Length of Fabry-Perot cavity

Γ	Radiative linewidth of atom
γ	Decay rate
γ_{in}	Intrinsic decay rate
$\hat{a}$	annihilation operator
$\hat{b}$	annihilation operator
$\hat{c}$	annihilation operator
$\hat{n}$	Cooper pair number operator
κ	Decay rate
$\mathfrak{L}$	lagrangian
e	Second atomic state index
f	Third atomic state index
g	First atomic state index; atom cavity coupling constant
h	Forth atomic state index
i	$\sqrt{-1}$
ν	Width of the first bloch band of a transmon qubit
ω	frequency in radians
ω_p	Plasma frequency of a Josephson junction
ω_{eg}	Transition frequency of an atom from ground to excited state
π	Area of unit circle

φ	Superconducting phase across a Josephson junction
φ_{ext}	external phase bias of a superconducting loop
$\|\Psi_i\rangle$	Wavefunction of i^{th} eigenstate of a many-body Hamiltonian
a	Unit cell size
c	Capacitance per unit length
C_g	Capacitance to ground
C_J	Capacitance of Josephson junction
E_C	Charging energy, defined as $E_C = e^2/2C$
E_J	Josephson energy
E_k	Energy of k^{th} Fabry-Perot mode
E_L	Inductive energy, defined as $E_L = (\Phi_0/2\pi)^2/L$
f_{eg}	$\omega_{\mathrm{eg}}/2\pi$
H	Hamiltonian
I	Current
i	Summation index
I_c	Critical current of Josephson junction
j	Summation index
k	Summation index; Wave-vector
l	Inductance per unit length

L_J	Linearized inductance of a Josephson junction
N	Number of junctions/modes in a transmission line
n_g	Gate charge
O	Big-O notation
P	Power
Q	Charge operator
Q^{ext}	Extrinsic quality factor
Q^{int}	Intrinsic quality factor
R	Resistance
t	Time
U	Unitary transformation
V	Voltage; Purturbation to Hamiltonian
Y	admittance
Z	impedance
Z_∞	wave impedance of a transmission line

Citations to Published Work

Parts of chapters 2, 4, 5, and 6 have appeared in the following papers:

- **N. Mehta**, C. Ciuti, R. Kuzmin, and V. E. Manucharyan. Down-conversion of a single photon as a probe of many-body localization. *arXiv:2203.17186*
- **N. Mehta**, C. Ciuti, R. Kuzmin, and V. E. Manucharyan. Superstrong coupling circuit quantum electrodynamics revisited. *in preparation*
- R. Kuzmin, N. Grabon, **N. Mehta**, A. Burshtein, M. Goldstein, M. Houzet, L. I. Glazman and V. E. Manucharyan. Inelastic scattering of a photon by a quantum phase slip. *Phys. Rev. Lett.*, 126:197701, May 2021
- R. Kuzmin, R. Mencia, N. Grabon, **N. Mehta**, Y. H. Lin, and V. E. Manucharyan. Quantum electrodynamics of a superconductor-insulator phase transition. *Nature Physics*, 15(9):930-934, 2019
- R. Kuzmin, **N. Mehta**, N. Grabon, R. Mencia, and V. E. Manucharyan. Superstrong coupling in circuit quantum electrodynamics. *npj Quantum Information*, 5:20, 2019

Chapter 1

Introduction

Quantum electrodynamics (QED) is a branch of physics describing a remarkable list of fundamental phenomena produced by the quantum nature of the electromagnetic field [1, 2, 3]. In addition to this, Quantum electrodynamics either directly or indirectly has also led to the invention of many important and ground-breaking practical applications including the laser, GPS, and more recently quantum computers [4, 5]. One of the simplest models of Quantum electrodynamics is that of cavity QED, where a single atom interacts with a single mode of quantized electromagnetic field. In this system the electromagnetic modes can be spatially confined and the corresponding vacuum fields can be dramatically enhanced [6]. A celebrated manifestation of cavity QED is the strong coupling

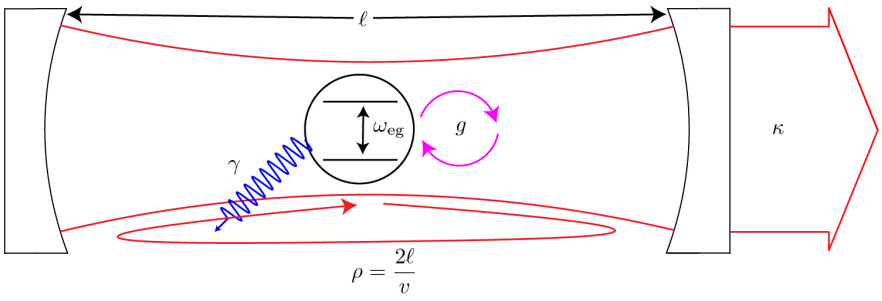

Figure 1.1: Atom with transition frequency $\omega_{\mathrm{eg}}/2\pi$ interacts coherently with radiation inside a Fabry-Perot cavity of length ℓ. The linewidth of the standing wave modes in the cavity and atom are given by κ and γ respectively. The free spectral range of the cavity is given by $\Delta = 1/\rho = v/2\ell$.

regime where the interaction strength between the atom and the electromagnetic fields g exceeds the intrinsic loss rates of the atom and the cavity γ, κ respectively (see Fig. 1.1). In this regime coherent exchange of single excitations can occur at the rate given by g, the vacuum Rabi frequency [6]. This strong coupling regime has attracted extensive attention in the last two decades and also forms the basis of most quantum computing architectures. More recently, new strong coupling regimes of cavity QED have been explored, in particular the *ultrastrong* coupling regime, achieved when the anti-resonant (non-rotating-wave) terms of light-matter interaction become relevant [7, 8, 9, 10] with just one cavity mode, such physics emerges when the vacuum Rabi frequency becomes comparable to the photon and atom transition frequencies. In the ultrastrong coupling regime, subspaces with different excitation numbers are coupled as a result of breaking of particle number conservation. As comprehensively reviewed in Refs. [11, 12, 13], the ultrastrong coupling regime has been investigated in many different platforms, including semiconductor systems [14, 15] and superconducting quantum circuits [16, 17].

1.1 Multi-mode cavity QED

Another kind of strong coupling regime that instead has been relatively overlooked so far in both theory and experiment, can be obtained in multi-mode resonators where the vacuum Rabi frequency exceeds the free spectral range of the resonator, namely the frequency difference between consecutive standing-wave modes. This regime of cavity QED was first pointed out theoretically in Ref. [18] and was coined as *superstrong* coupling regime and is mathematically defined as $\rho\Gamma \gg 1$, where ρ is the round trip time of photons in the cavity and Γ is the atom's spontaneous emission linewidth in the limit of infinite system size. The main predicted manifestation is the hybridization of the atom transition with several single-photon states in different modes, thus modifying their spatial profile [18]. In addition, this regime also enables coupling of states with different excitation numbers as states with multiple excitations become resonant with a single excitation state because of the presence of low frequency modes (see Fig. 1.2). This regime has been demonstrated recently via microwave spectroscopy on a superconducting platform consisting of a transmission line resonator coupled to a single transmon-type atom [19, 20, 21]. The main observation in the experiments is

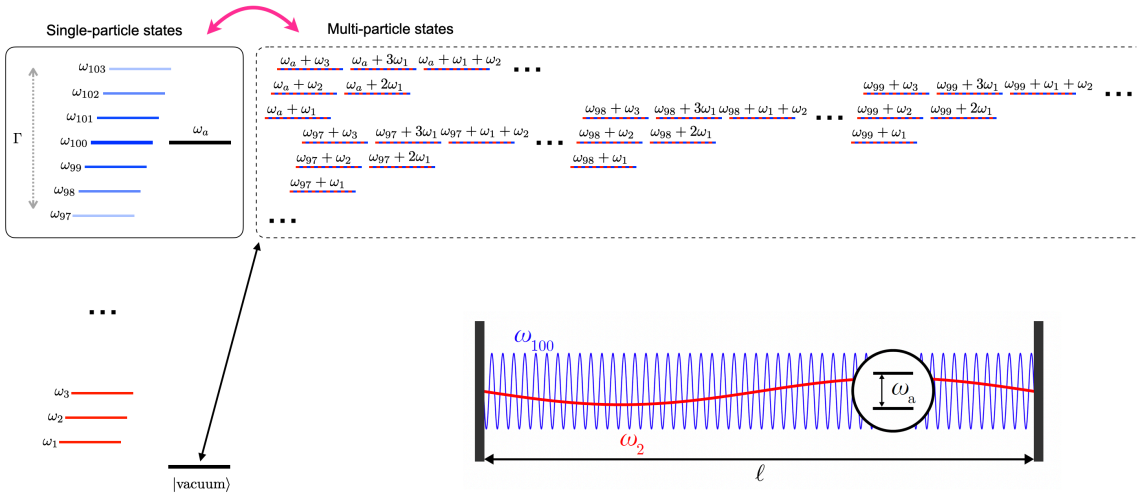

Figure 1.2: A schematic description of the energy levels of a multi-mode cavity coupled to a single qubit. The modes of the cavity have frequencies ω_j with $j = 1, 2, 3, ...$, while ω_a is the qubit transition frequency. On the left, the diagram depicts the energy levels of bare single-particle excitations (only one photon in one mode or only a qubit excitation). The qubit excited state can hybridize with several quasi-resonant single-photon states over a frequency window Γ. On the right, example of many-body states where multiple photons occupy different modes. Due to the existence of low-frequency modes, single-particle excitations can be resonant to multi-particle states.

that the frequencies of a large number of resonator modes around the atom transition frequency are shifted. However, the coupling was too low to expect quantum many-body effects with single photons. Another important point to make here is that these experiments were done using a weakly non-linear atom that can be modeled as a harmonic oscillator with a perturbative Kerr non-linearity. The corresponding Hamiltonian [20] is equivalent to a multi-mode bosonic Hopfield model [22]. In other words, as the atom hybridizes with more modes of the cavity, its non-linearity gets diluted in the harmonic modes of the cavity. As a result, counter intuitively, increasing the coupling would actually results in a more linear system.

1.2 Quantum impurity regime of cavity QED

From many-body physics perspective, the most intriguing scenario occurs by replacing a weakly-anharmonic atom [23, 19, 20, 21] with a strongly anharmonic one in a superstrongly coupled multi-mode cavity QED platform. In fact, quantum electrodynamics in this case maps onto the strongly

correlated quantum impurity models of condensed matter physics [24, 25, 26, 27, 28]. Quantum impurity models are among the simplest systems that display novel many-body effects, [29, 30, 31] the models consist of a large number of otherwise uncoupled degrees of freedom interacting with a local quantum impurity. In the cavity QED platform the role of the impurity is played by the atom and the non-interacting modes are the standing wave modes of the Fabry-Perot cavity. The atom in this case mediates interactions between a large subset of the cavity modes in direct analogy with quantum impurity models like the Kondo model where a single spin half impurity mediates coupling between a sea of non-interacting electrons[29, 30]. Theoretically, the computational complexity to make predictions on these models scales exponentially in the number of modes coupled simultaneously to the impurity [32]. The advantage of simulating quantum impurity models in a cavity QED setting is that, for sufficiently large coupling strengths, the many-body effects can be completely developed, while only needing to control one quantum degree of freedom which is in stark contrast to other experimental investigations of many-body phenomena that require the precise control of many individual quantum degrees of freedom [33, 34, 35, 36, 37, 38, 39, 40, 41].

To understand the origin of many-body dynamics in our multi-mode cavity QED system, let us ignore the effect of the atom, for the time being, and examine the Fock space of a cavity with uniformly-spaced mode frequencies $f_k = k\Delta$, where $k = 1, 2, ...$ (see Fig. 1.3). Consider exciting a single high-frequency photon in the mode $k \gg 1$. This single-particle state would be degenerate with about $O(k)$ two-particle states, as well as $O(k^2)$ three-particle states and so on so forth, as illustrated with blue and red color states in Fig. 1.3. What would be the effect of an atom at frequency $f_{\rm eg} \sim f_k$? In the single-particle approximation, the atom merely adds an energy-dependent phase-shift to reflected photons. This linear effect [23, 21, 42] amounts to weakly perturbing the standing wave modes in the frequency window $|f_k - f_{\rm eg}| \lesssim \Gamma$, where Γ coincides with the atom's spontaneous emission linewidth in the limit of infinite system size and satisfies $\Delta \ll \Gamma \ll f_{\rm eg}$ (the superstrong coupling condition). At the multi-particle level, though, the atom can induce a multi-particle interaction described in the most general way by the following effective Hamiltonian:

$$\frac{\hat{H}}{h} = \sum_{k>0} f_k \hat{a}_k^\dagger \hat{a}_k + \hat{V}_3 + \hat{V}_4 \ldots, \tag{1.1}$$

$$\hat{V}_i = g_i \sum_{k,k_2,\ldots k_i>0} A_{k,k_1,k_2,\ldots k_i} \hat{a}^\dagger_{k_1} \hat{a}^\dagger_{k_2} \ldots \hat{a}^\dagger_{k_i} \hat{a}_k + h.c. \tag{1.2}$$

Here $\hat{a}_k$ ($\hat{a}^\dagger_k$) is the operator that annihilates (creates) a photon at frequency f_k in the standing-wave mode k, which *already* includes a small atom admixture (due to hybridization with the atom). The atom as a separate entity is completely eliminated from this picture. The interaction energy scales g_i are linked to the parameters of the atoms and the cavity. The matrix elements $A_{k,k_1,\ldots k_i}$ are of order unity for $k_i = k$ but rapidly decay for $|k - k_i| \gtrsim \Gamma/\Delta$.

The interaction term $\hat{V}_i$ in Eq. 1.2 coherently couples a single-particle state $\hat{a}^\dagger_k|0\rangle$ to multi-particle states $\prod_i \hat{a}^\dagger_{k_i}|0\rangle$. Therefore, the relevant many-body Fock space of Hamiltonian (Eq. 1.1) has a tree-like connectivity, similar to the case of many quantum impurity problems in condensed matter physics [43]. The fate of a single excitation in such system can now be thought of as a hopping problem in this fictional lattice of many-body Fock space, where the hopping amplitude is given by the matrix elements of $\hat{V}_i$. In the case of a disorder free ideal system the hopping leads to delocalization of the single excitation in the many-body Fock space, where an initially excited photon in mode k irreversibly decays by down-conversion at a rate $\propto \sum_{k_1,k_2,\ldots k_i} |\langle 0|\hat{a}_k \sum \hat{V}_i \hat{a}^\dagger_{k_1} \hat{a}^\dagger_{k_2} \ldots \hat{a}^\dagger_{k_i}|0\rangle|^2 \delta(f_k - \sum f_{k_i})$ given by Fermi's Golden Rule [44]. However, for the case of system with finite disorder in the single particle spectrum, the massive degeneracy of the multi-particle states is lifted. Figure 1.4 shows the Hilbert space of such a system near mode k. In this case the fate of a single excitation becomes a many-body problem and absence of diffusion in the Fock space is called many-body localization, by analogy with Anderson localization in the real space [45]. This general phenomenon was subsequently predicted to occur in many other physical settings [46, 47, 48]. Being the only known mechanism to prevent isolated interacting systems from reaching thermal equilibrium, MBL has been attracting a vast attention from the theoretical physics community [49, 50].

1.3 Thesis overview

In this thesis we describe experiments and theory where we implement the quantum impurity regime of multi-mode QED using the platform of cQED (circuit Quantum Electrodynamics) [51]. Experimentally, this regime has been hard to achieve because it requires engineering strong coupling while

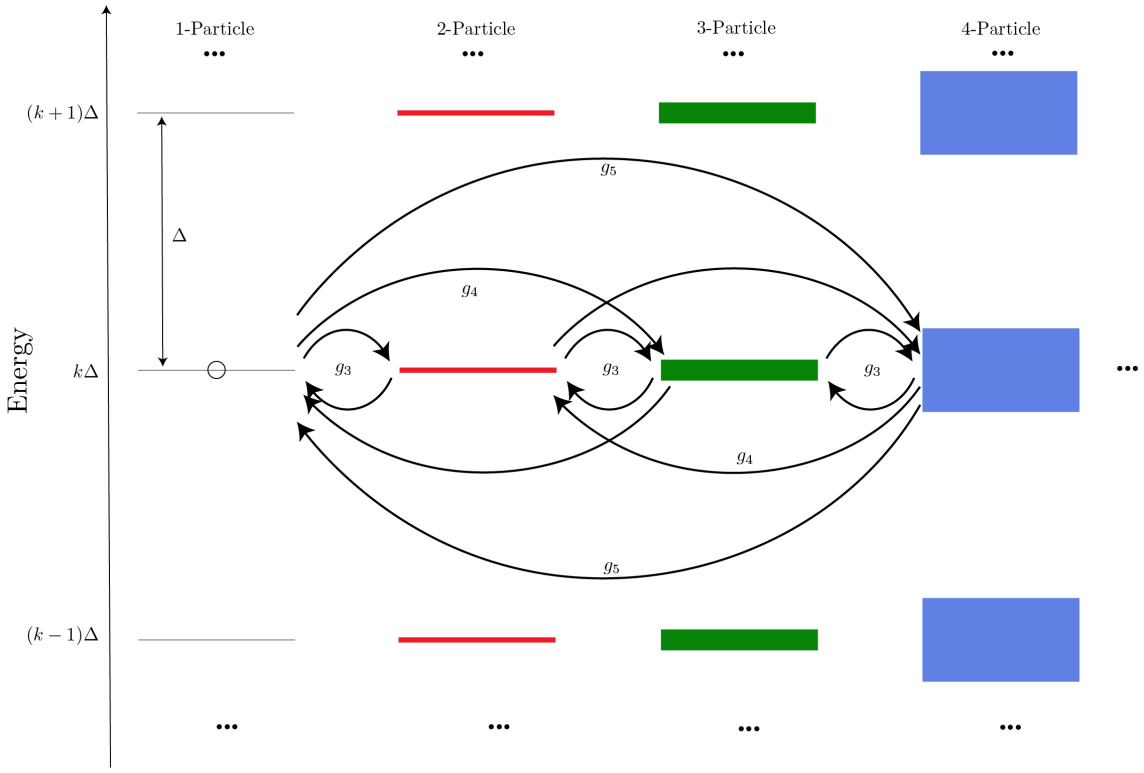

Figure 1.3: Energy levels of a disorder free multi-mode Fabry-Perot cavity with free spectral range Δ near mode number k. The Hilbert space is partitioned based on the number of excitations in each many-body state.

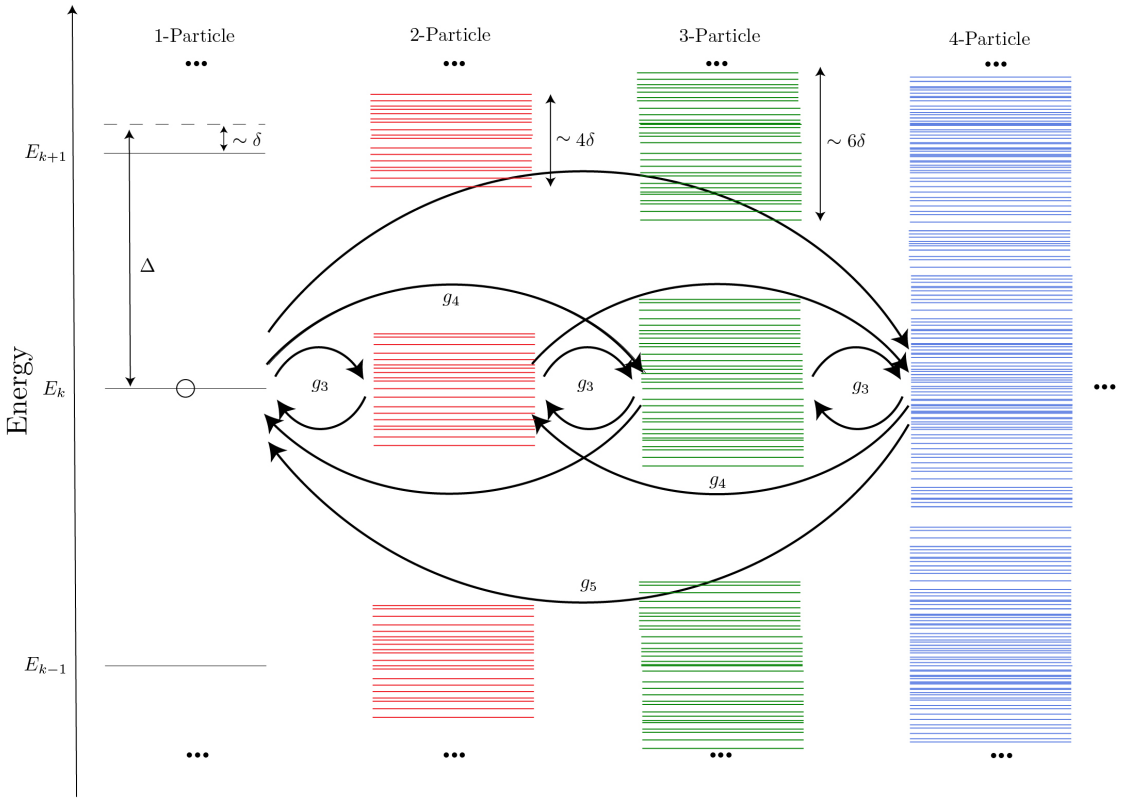

Figure 1.4: Energy levels of a disordered multi-mode Fabry-Perot cavity with free spectral range Δ near mode number k. The Hilbert space is partitioned based on the number of excitations in each many-body state.

simultaneously also decreasing the free spectral range of the cavity. We can illustrate this difficulty by an example for atom field coupling in 1-D, the coupling strength is typically proportional to $g \sim 1/\sqrt{\ell}$ and the free spectral range is $\Delta \sim 1/\ell$, so the ratio $g/\Delta \sim \sqrt{\ell}$. The slow growing nature of the function g/Δ is the reason why all of the recent experimental demonstrations of superstrong coupling regime require cavities with extremely large spatial dimensions[23, 52]. The first main technical innovation of this work is our ability to engineer Fabry-Perot cavity where the speed of light is slowed by a factor of 100 compared to the speed of light in vacuum. This allows us to implement a multi-mode cavity QED system in a compact form factor. Second innovation is the galvanic connection between the Fabry-Perot cavity and the artificial atoms which gives us access to practically infinite coupling and allows us to reach the quantum impurity regime. In addition we are also able to engineer different connectivity in the many-body Fock space of the Fabry-Perot modes by engineering the non-linearity of the artificial atoms. In two different experiments by engineering sparse and dense connectivity in the many-body Hilbert space we observe both the localization and delocalization of single excitation states in the many-body Fock space.

The thesis is organized as follows. Chapter 2 gives a brief overview of the physics of quantum electrical circuits. Here we derive and explain the Hamiltonian of the multi-mode Fabry-Perot cavities and artificial atoms used in the thesis. Chapter 3 discusses the experimental tools used in the work. Chapter 4 describes the experimental implementation of the multi-mode Fabry Perot cavity using a long chain of Josephson junctions. The next two chapters 5, 6 describe in detail two specific implementations of multi-mode cavity QED in the quantum impurity regime. In the first case we are able to engineer the connectivity in the Fock space such that the single photon excitation gets localized and we observe the violation of Fermi's golden rule. In the second case we engineer the qubit impurity in the exact opposite limit where a single excitation in a high frequency mode of the cavity decays into a shower of odd number of lower frequency photons. We confirm this by measuring the lifetime of the photon of the cavity modes and match the decreased lifetime to a Fermi's golden rule calculation. The last chapter summarizes the results and discusses some future work.

Chapter 2

Circuit Theory

In this chapter we provide a brief introduction to the quantum theory of superconducting circuits. We start by introducing the circuit elements used to construct to the devices in the experiments described in this work. We then proceed to describe the construction of the two main ingredients in our work namely the linear multi-mode Fabry-Perot cavity and artificial atoms using the circuit elements. And finally we conclude by deriving the couplings between the two class of circuits. The last two sections of this chapter derive the microscopic many-body circuit Hamiltonians of the multi-mode circuit QED systems described in this thesis.

2.1 Introduction to circuit QED

As introduced in the last chapter, circuit quantum electrodynamics (cQED) is a solid state implementation of the cavity QED setup. cQED studies the coherent interaction between artificial atoms made of superconducting elements with discrete energy levels, and microwave photons that live inside superconducting cavities. The ability to engineer properties of both the artificial atoms and photons though clever circuit design and nano-fabrication enables this platform to study the physics of light matter interactions in regimes experimentally inaccessible by natural atoms and light. These properties have made cQED as one of the leading platforms for both digital and analog quantum information processing. Excellent state-of-the-art reviews can be found in these references [53, 54, 55, 56].

Before we begin to construct complicated quantum many-body systems using electrical circuits, we need to understand under what conditions do the electric and magnetic fields inside these macroscopic circuit elements can be thought of in terms of quantum mechanical operators. The quantum theory of circuits was pioneered by Michel Devoret and Steven Girvin in [57, 58], and this chapter will closely follow their lecture notes. The first vital ingredient in constructing quantum electrical circuits is superconductivity! Superconductivity is described by the condensation of pairs of electrons of opposite spin (Cooper pairs) into a ground state significantly gaped from the single-excitation band of states where a single Cooper pair is broken. This excitation gap is effectively responsible for reducing the number of degrees of freedom and allowing current to flow in the superconductor without dissipation, thereby allowing these collective charge modes to be simply described by the charge built up at a node or by the supercurrent flowing in a wire connecting two nodes.

Reducing the Hilbert space of superconducting circuits to just a single degree of freedom (charge or flux) is not enough to justify a quantum mechanical treatment. Not only do we need to cool down the circuit to introduce superconductivity, but we need to operate at a temperature where the thermal fluctuations of the charge and flux are much smaller than the quantum ones associated with the microwave resonance of the circuit $k_B T \ll \hbar\omega$. This is the reason why all circuit QED experiments involve anchoring the circuit to cold stage of a dilution refrigerator typically operating in the $10 - 15\,\mathrm{mK}$. This temperature is much smaller than energy of a $5\,\mathrm{GHz}$ microwave photon which corresponds to $240\,\mathrm{mK}$. These circuits are described by many levels associated with different quanta of microwave excitations. Therefore, it becomes equally critical to engineer modes with high quality factor $Q \gg 1$ [59] in order to distinguish these energy states and quantize the circuit. All of the circuits described in this thesis can be decomposed into a network of three basic two terminal components, namely capacitors, inductors and Josephson junctions. Each of these components is defined by the total superconducting phase across it and the the total current flowing through it. Each element is also defined by its unique current-phase relation which links the current flowing through the element and the superconducting phase across it as a function of time

$$I(t) = f(t)V(t), \tag{2.1}$$

and the total electrical energy stored in such an element is given by:

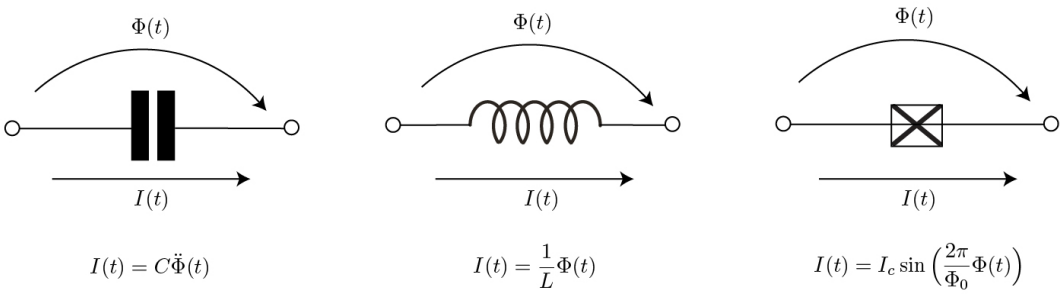

Figure 2.1: Current phase relation of three basic two terminal components used in circuit QED

$$E(t) = \int_{-\infty}^{t} V(t')I(t')dt'. \tag{2.2}$$

For the purposes of describing the circuits in the Lagrange-Hamilton formalism, its instructive to define two additional variables which will serve as the generalized coordinates for each component. The coordinates can either be the magnetic flux across the component which is related to the voltage as:

$$\Phi(t) = \int_{-\infty}^{t} V(t')dt', \tag{2.3}$$

or the charge flowing through the component which is related to the current as:

$$Q(t) = \int_{-\infty}^{t} I(t')dt'. \tag{2.4}$$

Since an arbitrary circuit can contain more branches than there are degrees of freedom, it becomes more intuitive to define the network in terms of the flux and charge variables at each node. The reader is encouraged to visit a more detailed description of this method of nodes in [59, 58]. The choice of these node flux and charge variables in a network of two terminal components is akin to choosing a set of generalized coordinates in a classical mechanics problem. This choice of variables, as will be shown in the subsequent sections of this chapter merely defines the gauge for the problem at hand and does not affect the dynamics of the problem.

2.1.1 Capacitors

Capacitors are formed by two conducting surfaces separated by an insulator or a gap. The voltage across this element is then directly proportional to the charge accumulated on the conducting surfaces and the inverse of the proportionality constant is know as the capacitance. This leads to the following expression for the energy stored in a capacitor:

$$V(t) = \frac{1}{C}Q(t), \tag{2.5}$$

$$E(t) = \frac{1}{2}C(V(t))^2, \tag{2.6}$$

$$E(t) = \frac{(Q(t) - Q(-\infty))^2}{2C}. \tag{2.7}$$

2.1.2 Inductors

Similarly, an inductor is a piece of superconducting wire where the voltage across the wire is proportional to the rate of change of current flowing through the wire and the proportionality constant is known as the inductance of the wire. This leads to the following expression for the energy stored in an inductor:

$$V(t) = L\frac{dI(t)}{dt}, \tag{2.8}$$

$$E(t) = \frac{1}{2}L(I(t))^2, \tag{2.9}$$

$$E(t) = \frac{(\Phi(t) - \Phi(-\infty))^2}{2L}. \tag{2.10}$$

2.1.3 Josephson junction

A Josephson junction is formed by a thin layer of an insulator sandwiched between two bulk superconductors. This is a special element which introduces non-linearity and is responsible for all of the interesting physics that can be studied using circuit QED. The origin of the non-linearity of this element comes from the coherent tunneling of Cooper pairs across the thin insulting barrier which

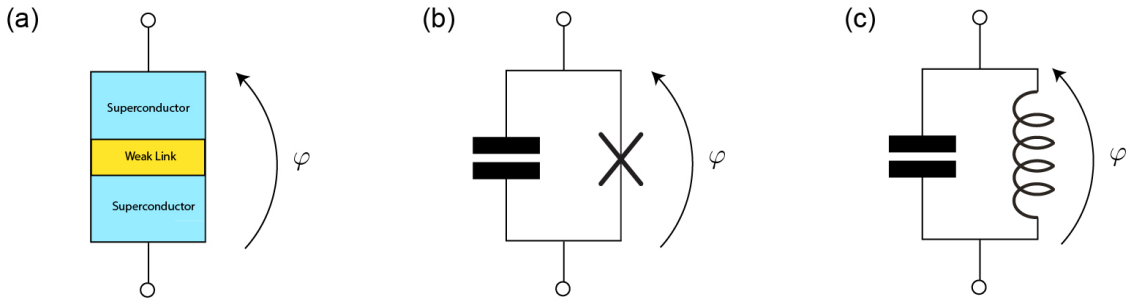

Figure 2.2: (a) Josephson tunnel junction formed by sandwiching a weak link between two superconductors. (b) Effective circuit model of a Josephson junction as a non-linear element denoted by the cross in parallel with its self capacitance. (c) Effective linearized circuit model of the Josephson junction.

in turn is a result of the overlap of the ground state wavefunctions in the two superconducting electrodes [60]. If we assume the number of Cooper pairs on the left electrode as N_L and on the right electrode as N_R then the phenomenon of tunneling can be described by the following Hamiltonian:

$$H_{JJ} = -\frac{1}{2}E_J \sum_m (|m\rangle\langle m+1| + |m+1\rangle\langle m|)\,, \tag{2.11}$$

here m denotes the Cooper pairs transferred across the tunnel junction and the parameter E_J determines the rate of this tunneling. This Hamiltonian is identical to a one-dimensional tight binding model and its eigenstates are plane waves given by:

$$|\varphi\rangle = \sum_{m=-\infty}^{+\infty} e^{im\varphi}|m\rangle\,, \tag{2.12}$$

here $\varphi = ka\,, a = 1$ is the wavevector of the plane waves. Applying this ansatz to the tunneling Hamiltonian we get the well known cosine dispersion of the eigenvalues:

$$H_{JJ}|\varphi\rangle = -E_J \cos\varphi|\varphi\rangle\,. \tag{2.13}$$

We can now also define the variable conjugate to the wavevector which is the total number of Cooper pair tunneled $n = \sum_m m|m\rangle\langle m|$. In this representation φ can now be thought as the position

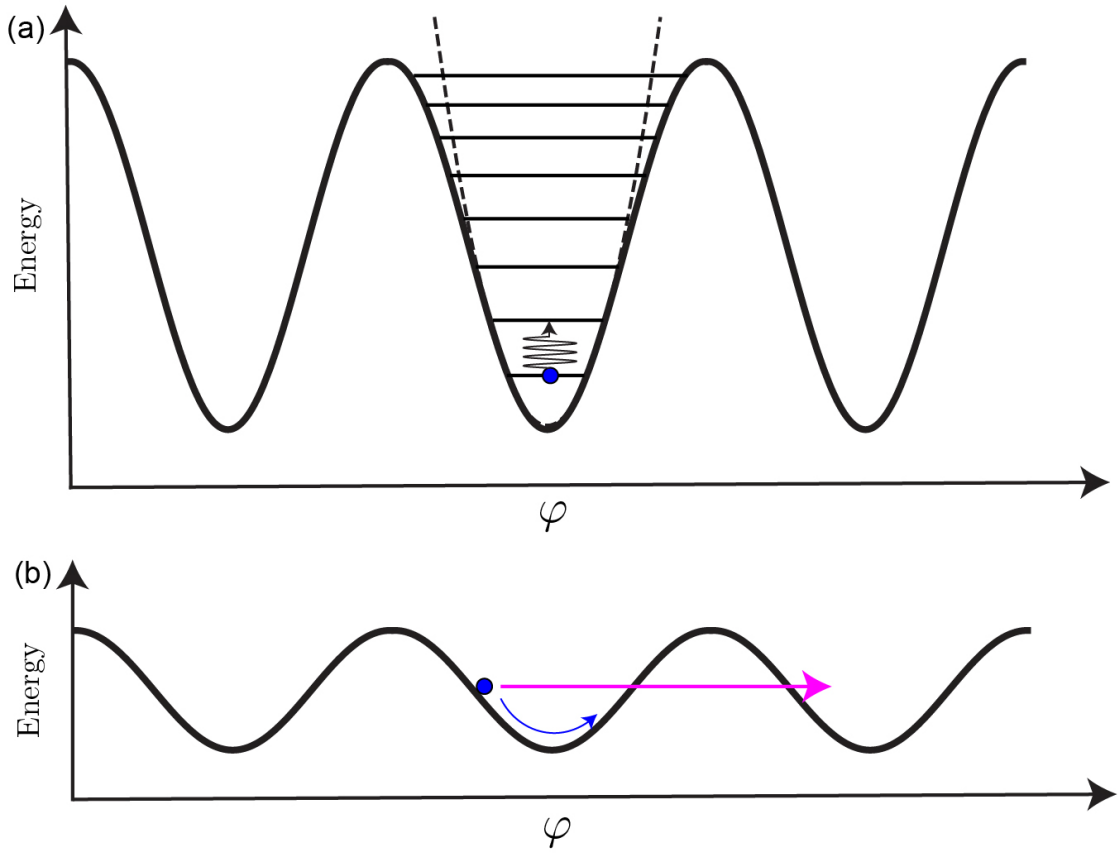

Figure 2.3: (a) Cosine potential of a large area Josephson junction where the dynamics of the phase particle is confined to a single well. (b) Cosine potential of small area Josephson junction where the tunneling of the phase particle across multiple wells is important.

of a fictional particle in a cosine potential and the number of Copper pairs as the momentum of this particle.

We are now ready to derive the phase current relationship of the Josephson junctions. For this we consider a voltage biased junction whose Hamiltonian is given by:

$$H_{JJ} = -E_J \cos\varphi - 2eVn. \tag{2.14}$$

By writing the equations of motion for the variables φ and n we arrive at:

$$\frac{\partial n}{\partial t} = \frac{H_{JJ}}{\hbar \partial \varphi} = (E_J/\hbar)\sin\varphi\,, \tag{2.15}$$

$$\frac{\hbar \partial \varphi}{\partial t} = \frac{H_{JJ}}{\partial n} = 2eV.$$

The first equation of motion is the DC Josephson relation which gives the current phase relation of the Josephson junction as [61]:

$$I = I_c \sin\varphi\,, \tag{2.16}$$

here $I_c = \frac{2e}{\hbar} E_J$, is the maximum possible dissipationless current which can flow through the tunnel junction. The second equation of motion is the AC Josephson relation which gives the AC response of the junction to a DC bias voltage:

$$\varphi(t) = \varphi(0) + \frac{2e}{\hbar} Vt\,, \tag{2.17}$$

$$I(t) = I_c \sin(\varphi(0) + \omega t)\,, \tag{2.18}$$

where, $\omega = 2eV/\hbar$ is the frequency of the AC current.

This is not the complete picture of a Josephson junction since every physical Josephson junction also comes with a corresponding self capacitance formed by the two superconducting electrodes separated by a dielectric. Including the effect of the capacitor, the Hamiltonian of an isolated Josephson

junction can then be written as:

$$H_{JJ} = 4E_C n^2 - E_J \cos\varphi, \tag{2.19}$$

here E_C is the energy associated with the self capacitance. In the phase particle analogy the self capacitance takes the role of mass of the fictional phase particle. Depending on the relative values of the Josephson (E_J) and charging (E_C) energies the dynamics of the phase particle can be broadly divided into two categories (see Fig 2.2, 2.3). This first is when the ratio $E_J/E_C \gg 1$, in this case the phase particle is confined to a single Josephson well and the cosine potential can be approximated to its lowest order. In this case the Josephson junction acts similar to an LC oscillator with an effective linearized Josephson inductance given by:

$$\begin{aligned} L_J &= \left(\frac{\hbar}{2e}\right)^2 \frac{1}{E_J} \\ &= \frac{\hbar}{2eI_c} \end{aligned} \tag{2.20}$$

These types of junctions in the thesis will be refereed to as linear junctions. The second case is when $E_C \sim E_J$ then the dynamics of the phase particle involves tunneling across multiple cosine well and in this case in general the full cosine term of the potential is important.

2.2 Linear superconducting circuits: Microwave photons

Now, that we have finished describing the basic building blocks, we can now start combining these elements like Lego blocks to construct more complex composite circuits. In this section we will describe the construction of linear superconducting circuits that play the role of light in the light matter coupling studied by circuit Quantum Electrodynamics (cQED).

2.2.1 Lumped element L-C oscillator

The simplest composite circuit that can be constructed using the linear elements is that of a parallel combination of inductor and a capacitor which forms a lumped element LC resonator. The dynamics

of this circuit can be described by a single variable the flux across the inductor or its conjugate variable the charge on the capacitor. Using the current phase relations developed in the last section we can get the energy stored in the inductor and capacitor which gives us the following Lagrangian for the circuit:

$$\mathfrak{L} = \frac{C\dot{\Phi}^2}{2} - \frac{\Phi^2}{2L}, \tag{2.21}$$

and the corresponding Euler-Lagrange equations of motion:

$$\ddot{\Phi} = -\frac{\Phi}{LC}, \tag{2.22}$$

where the natural frequency of oscillation of the circuit is given by $\omega = 1/\sqrt{LC}$. The charge across the capacitor can then be represented as :

$$Q = \frac{\partial \mathfrak{L}}{\partial \dot{\Phi}} = C\dot{\Phi}. \tag{2.23}$$

Applying the Legendre transform to the Lagrangian gives us the Hamiltonian of the circuit:

$$H = Q\dot{\Phi} - \mathfrak{L} = \frac{Q^2}{2C} + \frac{\Phi^2}{2L}. \tag{2.24}$$

To write the quantum Hamiltonain of this circuit we promote the charge and flux variables to quantum operators obeying the commutation relation $[\hat{\Phi}, \hat{Q}] = i\hbar$. For convenience we introduce new dimensionless variables of the flux and charge where the flux is normalized by the superconducting flux quantum $\varphi = \Phi/(\hbar/2e)$ and the charge is normalized by the charge of a Cooper pair $n = Q/2e$. Going forward in this thesis the circuit Hamiltonains will be written in terms of these new variables and their corresponding quantum operators which satisfy the commutation relation $[\hat{\varphi}, \hat{n}] = i$.

The Hamiltonian of the lumped element L-C oscillator can now be written also in terms of annihilation and creation operators defined as:

$$\begin{aligned} \hat{\varphi} &= \frac{\hbar}{2e}\varphi_{ZPF}(\hat{a} + \hat{a}^\dagger), \\ \hat{n} &= i2e\, n_{ZPF}(\hat{a} - \hat{a}^\dagger), \end{aligned} \tag{2.25}$$

$$\hat{H} = \hbar\omega(\hat{a}^\dagger\hat{a} + \frac{1}{2}) \tag{2.26}$$

where φ_{ZPF} and n_{ZPF} are the zero point fluctuations of the phase and Cooper pair number variables given by:

$$\begin{aligned} \varphi_{ZPF} &= \sqrt{\frac{Z}{\pi R_Q}}, \\ n_{ZPF} &= \sqrt{\frac{R_Q}{4\pi Z}}. \end{aligned} \tag{2.27}$$

In these expressions $Z = \sqrt{L/C}$ is the impedance of the L-C circuit and the constant $R_Q = h/4e^2$ is the superconducting resistance quantum.

2.2.2 Standing wave modes on a transmission line

Most circuit QED experiments only involve a single mode of a superconducting resonator where a simple lumped element model can be used however for this work, we specifically study multi-mode circuit QED where multi-mode structure of the device plays an important role. In our case this multi-mode structure is due to the standing wave modes on a two-wire superconducting transmission line resonator. In this section, we present the standard approach to finding the normal modes of such a distributed resonator, first using a classical description of the circuit.

Here we consider the specific case of a simple one dimensional two-wire telegraph style transmission line (see Fig. 2.4 (a)). Fig 2.4 (b) shows the equivalent lumped element circuit mode for such a transmission line, where the distributed system is represented as a ladder of lumped element inductances $l \times dx$ in series and capacitances $c \times dx$ to ground. Using the method prescribed in section 2.2.1 we define the reduced node fluxes associated to each node as φ_j and we can write the Lagrangian of the system:

$$\mathfrak{L} = \left(\frac{\hbar}{2e}\right)^2 \sum_{j=0}^{N-1} \left[\frac{1}{2}c\dot{\varphi}_j^2 dx - \frac{(\varphi_{j+1} - \varphi_j)^2}{2l dx}\right], \tag{2.28}$$

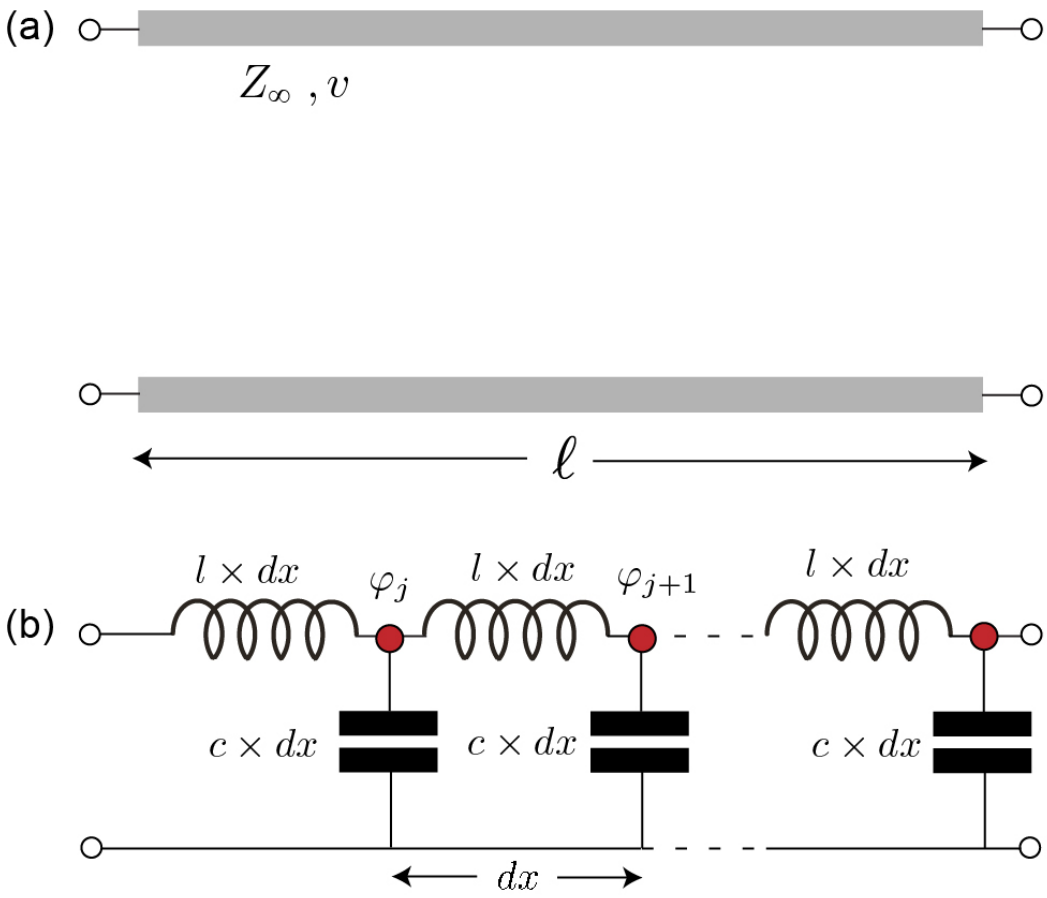

Figure 2.4: (a) Circuit schematic of a distributed 1-D transmission line resonator. (b) Lumped element circuit mode showing the capacitance and inductace per unit length and the reduced node fluxes at each node.

and the corresponding Hamiltonian as:

$$H = \sum_{j=0}^{N-1} \Big[4e^2 \frac{n_j^2}{2cdx} + \Big(\frac{\hbar}{2e}\Big)^2 \frac{(\varphi_{j+1} - \varphi_j)^2}{2ldx} \Big]. \tag{2.29}$$

By considering the continuum limit of this Hamiltonian when the unit cell size of the lumped model is taken to zero such that $Ndx = \ell$ we get the following:

$$H = \int_0^\ell dx \Big[4e^2 \frac{n(x)^2}{2c} + \Big(\frac{\hbar}{2e}\Big)^2 \frac{(\partial_x \varphi(x))^2}{2l} \Big], \tag{2.30}$$

where we have used the fact that $\partial_x \varphi(x) = \lim_{dx \to 0} (\varphi_{j+1} - \varphi_j)$ and we have defined the Cooper pair density as $n(x) = n_j/dx$. Writing the Hamilton's equation of motion for Eq 2.30, we arrive at the wave propagation equation for the transmission line as

$$v^2 \frac{\partial^2 \varphi(x,t)}{\partial x^2} - \frac{\partial^2 \varphi(x,t)}{\partial t^2} = 0, \tag{2.31}$$

where $v = 1/\sqrt{lc}$, is the speed of light in the transmission line. We can solve the wave equation by using the method of separation of variables by using the ansatz:

$$\varphi(x,t) = M(x)N(t), \tag{2.32}$$

we arrive that the equations $\ddot{N}(t) = -\omega^2 N(t)$ and $\ddot{M}(x) = -k^2 M(x)$, with ω being the frequency of the standing wave modes and k being the wavevector. The spatial and temporal mode profile of the standing wave modes can be written explicitly as:

$$\begin{aligned} N(t) &= A\cos(\omega t) + B\sin(\omega t), \\ M(x) &= C\cos(kx) + D\sin(kx), \end{aligned} \tag{2.33}$$

and the constants $A, B, C,$ and D are set by the boundary conditions of the transmission line at $x = 0$ and $x = \ell$. For the case of a open circuit boundary condition on both ends we can arrive at the result where the wavevector is quantized as $k_j = j\pi/\ell$ and the corresponding frequencies for the standing wave modes as $\omega_j = j\omega_0$, where the $\omega_0/2\pi$ is the frequency of the fundamental mode of

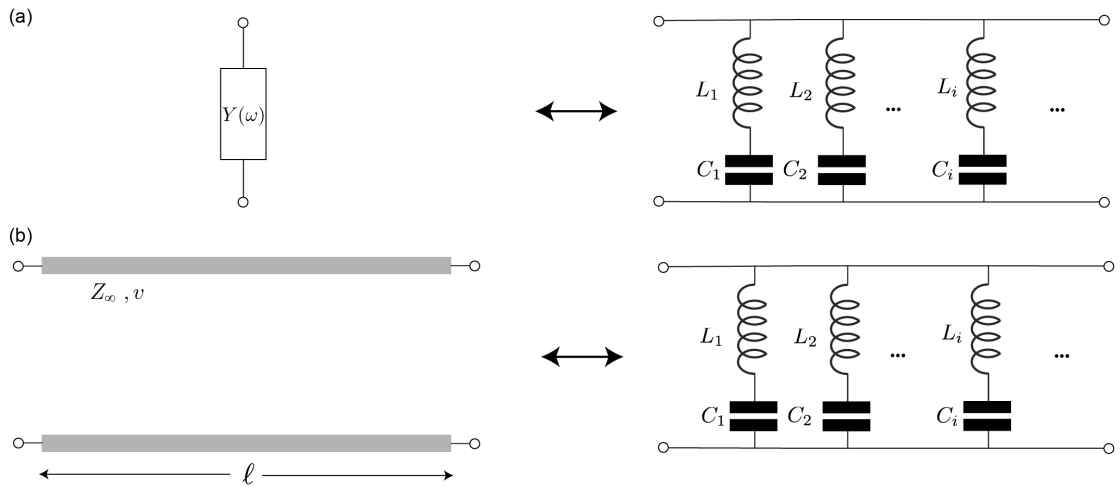

Figure 2.5: (a) Foster's decomposition of an arbitrary admittance function $Y(\omega)$ (b) Foster's decomposition of an open section of a 1-D transmission line resonator of length ℓ. The exact values of the capcitances and the inductances in the decomposition is given by Eq. 2.37

the transmission line. By following the quantization procedure for a Harmonic oscillator discussed in section 2.2.1 we arrive at the Hamiltonian of the transmission line written as:

$$\hat{H} = \sum_{j=0}^{\infty} \hbar\omega_j (\hat{a}_j^\dagger \hat{a}_j + \frac{1}{2}) \tag{2.34}$$

2.2.3 Foster's decomposition of transmission line

A more convenient harmonic mode decomposition of the standing wave modes on a transmission line can be found by using the Foster's theorem. Foster's theorem [62] states that any physical admittance function $Y(\omega)$ can be represented by an infinite number of series L_jC_j-circuits connected in parallel, as shown in Fig. 2.5 (a). The admittance $Y^F(\omega)$ of such lumped element circuit is given by:

$$Y^F(\omega) = \sum_{j=1}^{\infty} \frac{i\omega C_j}{(1 - \omega_j L_j C_j)}. \tag{2.35}$$

To find the values of L_j and C_j, it is sufficient to match the poles and the residues of the two analytical functions $Y(\omega)$ and $Y^F(\omega)$. In this section we will first derive the Foster's decomposition for the simplest possible case of an open section of a 1-D transmission line of length ℓ, characterized

by the speed of light v and the wave impedance Z_∞. The admittance of such a transmission line of length ℓ is given by [63]:

$$Y(\omega) = \frac{\mathrm{i}}{Z_\infty} \tan(\omega \ell / v)\,. \tag{2.36}$$

Matching the poles and residues of functions given by Eq. (2.36) and Eq. (2.35) results in the equally spaced poles at frequencies $\omega_j = 2\pi\Delta(j - 1/2)$, where the free spectral range is $\Delta = v/2\ell$. The inductances and capacitances read:

$$\begin{aligned} L_j = L_1 &= \frac{Z_\infty}{4\Delta}\,, \\ C_j &= \frac{1}{Z_\infty \pi^2 \Delta} \times \frac{1}{(j-1/2)^2}\,. \end{aligned} \tag{2.37}$$

We can generalize the Foster's decomposition method for a line with an arbitrary wave dispersion $k(\omega)$, frequency-dependent wave impedance $Z_\infty(\omega)$ and an arbitrary reactive termination, characterized by the phase shift $\tau(\omega)$. The admittance of such a line is given by:

$$Y(\omega) = \frac{1}{Z_\infty(\omega)} \left(\frac{\mathrm{e}^{-\mathrm{i}\tau(\omega)} - \mathrm{e}^{-2\mathrm{i}k(\omega)\ell}}{\mathrm{e}^{-\mathrm{i}\tau(\omega)} + \mathrm{e}^{-2\mathrm{i}k(\omega)\ell}} \right), \tag{2.38}$$

whose poles ω_j are implicitly defined by:

$$k(\omega_j)\ell = \pi(j - 1/2) + \tau(\omega_j)\,. \tag{2.39}$$

In general, Eq. (2.39) produces non-uniformly spaced modes. Nevertheless, the parameters L_j and C_j can still be expressed in a compact form:

$$L_j = \frac{Z_\infty(\omega_j)}{2} \frac{\ell \partial k}{\partial \omega}\bigg|_{\omega=\omega_j}\,, \tag{2.40}$$

$$C_j = \frac{2}{\omega_j^2 Z_\infty(\omega_j)} \frac{\partial \omega}{\ell \partial k}\bigg|_{\omega=\omega_j}\,. \tag{2.41}$$

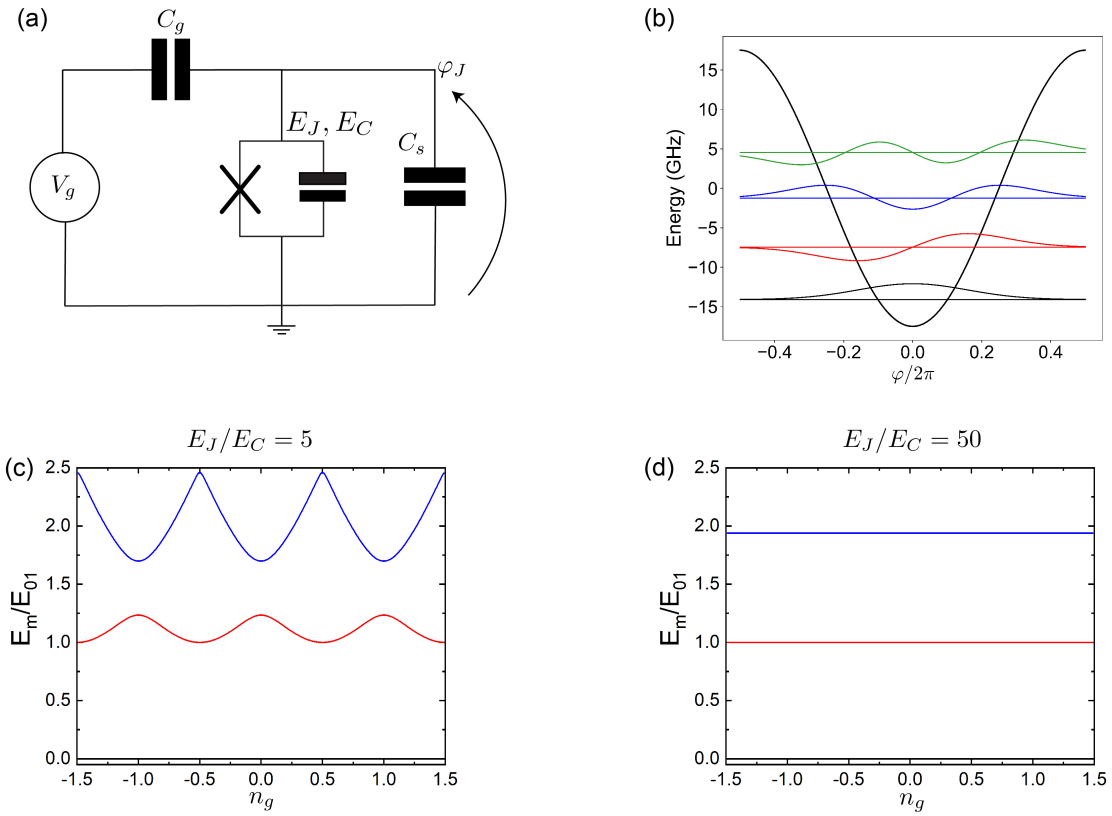

Figure 2.6: (a) Circuit schematic in the most general form of a charge qubit (b) Wavefunction and energy of the first four eigenstates of a transmon qubit. (c, d) Energy levels of a charge qubit as a function of the the n_g for two different ratios of E_J/E_C.

2.3 Non-linear superconducting circuits: Artificial atoms

In this section we will describe the construction of non-linear superconducting circuits that play the role of artificial atoms. There is an entire periodic table [57] of superconducting artificial atoms but for this brief introduction we will focus on two widely used circuits with distinct topology. In the first example a single Josephson junction is connected to two isolated superconducting islands and in the second one we consider a Josephson junction shunted by a very large kinetic inductance forming a loop.

2.3.1 Charge qubits

Charge qubits are the simplest circuits (in terms of circuit complexity) that can be operated as a qubit. They essentially only consist of a single superconducting island connected to ground by a Josephson junction and the charge on the island is biased by a voltage source. This voltage source induces an offset charge on the island given by $2en_g = V_g C_g$. We will work with the dimensionless variable which converts the induced charge to the number of Cooper pairs. The junction has a self capacitance C_J and can also be shunted by an additional capacitance C_S. The Hamiltonian of such a circuit is governed by the superconducting phase across the junction $\hat{\varphi}_J$ and its conjugate variable the Cooper pair number operator $\hat{n}_J$. The Hamiltonian can be written as:

$$\hat{H} = 4E_C(\hat{n} - n_g)^2 - E_J \cos(\hat{\varphi}_J), \tag{2.42}$$

here E_C is the total charging energy of the island given by $E_C = e^2/2(C_S + C_J + C_g)$. Note that this Hamiltonain is exactly the same as that of a Josephson junction but now with the Coulomb interaction associated with the capacitance taken into account. The Hamiltonian describes a fictional phase particle in a periodic cosine potential where the Josephson energy defines the amplitude of the cosine potential and the charging energy defines the inverse of the mass of this particle. This Hamiltonian can be exactly solved and the solutions are given by the well known *Mathieu* functions [64]. The charge qubits can be broadly classified into two categories based on the relative value of the ratio between the Josephson tunneling energy and the charging energy E_J/E_C. We will first discuss the simple case when $E_J/E_C \gg 1$ and then proceed to describe what happens when the E_J/E_C is decreased.

2.3.1.1 Transmon

When the Josephson junction in Fig 2.6 (a) is shunted by a large capacitance, we can think of this as a scenario where the tunneling potential barrier for the fictional phase particle is enhanced and the mass is increased. In this scenario the tunneling between the adjacent well is strongly suppressed and the phase particle wave function is strongly localized in one cosine well (Fig. 2.6 (b)) with small phase excursions around the minimum. We can also estimate using the WKB approximation

the charge dispersion of the energy levels of this Hamiltonian. The band structure for the m^{th} energy level of the transmon can be written as $E_m(n_g) = E_m(n_g = 0.25) + \frac{1}{2}\epsilon_m \cos(2\pi n_g)$, where the charge dispersion ϵ_m is given by [64]:

$$\epsilon_m \approx (-1)^m E_C \frac{2^{4m+5}}{m!}\sqrt{\frac{2}{\pi}}\Big(\frac{E_J}{2E_C}\Big)^{m/2+3/4}\exp(-\sqrt{8E_J/E_C}). \tag{2.43}$$

This expression shows that the energy levels of the transmon become exponentially insensitive to the charge offests as the ratio E_J/E_C is increased. This justifies the Taylor series expansion of the cosine potential which leads to the following transmon Hamiltonian:

$$\hat{H}_{\text{transmon}} = 4E_C\hat{n}_J^2 - E_J\Big(-\frac{1}{2}\hat{\varphi}_J^2 + \frac{1}{24}\hat{\varphi}_J^4 + O(\hat{\varphi}_J^6)\Big). \tag{2.44}$$

In this approximation the transmon can be thought of as a quantum harmonic oscillator with a weak Kerr type non-linearity.

$$\hat{H}_{\text{transmon}} = \hbar\omega_{\text{eg}}\hat{a}^\dagger\hat{a} - \frac{E_C}{2}\hat{a}^\dagger\hat{a}\hat{a}^\dagger\hat{a}, \tag{2.45}$$

where the transition energy between the lowest two states is given by $\omega_{\text{eg}} = \sqrt{8E_JE_C} - E_C$. For the experiments described in chapter 6, we incorporate flux tunability in the transmon by replacing the Josephson junction with a SQuID loop. The SQuID loop can be thought as a single Josephson junction whose Josephson energy depends on the flux threading the loop given by:

$$E_J(\varphi_{\text{ext}}) = (E_{J_1} + E_{J_2})\cos(\varphi_{\text{ext}}/2)\sqrt{1 + d^2\tan^2(\varphi_{\text{ext}}/2)}, \tag{2.46}$$

here E_{J_1}, E_{J_2} are the Josephson energies of the two junctions in the SQuID loop and the parameter $d = |E_{J_1} - E_{J_2}|/(E_{J_1} + E_{J_2})$ is dependent on the asymmetry of the two junctions.

2.3.2 Flux qubits

Flux qubits consist of a different topology of circuits where the Josephson junction is shunted by an inductor forming a superconducting loop. The change in topology of the circuit has profound consequences on the mathematical description. The difference originates from the fact that now

the potential landscape for the phase across the Josephson junction is no longer a periodic function and the phase is not defined on a circle $\varphi_j \in (0 - 2\pi)$ but on a real line. Instead of periodic boundary conditions imposed on the wavefunction we can now impose the boundary condition of the wavefunction going to zero as $\varphi_J \to \infty$. Including the energy of an inductor to the Hamiltonian of a Josephson junction we arrive at the Hamiltonian for a flux qubit:

$$\hat{H} = 4E_C(\hat{n}_J - n_g)^2 + \frac{1}{2}E_L\hat{\varphi}_J^2 - E_J\cos(\hat{\varphi}_J - \varphi_{\text{ext}}). \tag{2.47}$$

Because the charge is now a continuous variable we expect on physical grounds that a static offset charge n_g can be completely screened and should not affect the energy. Mathematically this can be seen as performing a unitary gauge transformation and physically this can be thought of as a DC short that can screen all the offset charge to the ground. Before we proceed to describe the spectrum of flux qubit, we should note that there is an additional control knob in the circuit which comes from the superconducting flux quantization condition and this can be thought of as the flux qubit analog of the offset charge variable n_g. As with the case of offset charge, we see that the resulting spectrum must be periodic in the offset flux.

Given our ability to engineer E_J, E_L, E_C and the external flux φ_{ext} threading the superconducting loop we can create a wide variety of potential landscapes and as a by-product a wide variety of level structures in these qubits. Some of the most famous incarnations of the flux qubits are three junction flux qubit [65], C-shunt flux qubit [66], fluxonium [67]. Transition energy and wavefunctions for flux qubit in the three junction flux qubit regime and fluxonium regime are plotted in Fig. 2.7. In this work we work in the fluxonium regime of the flux qubit which is described next.

2.3.2.1 Fluxonium qubit

The fluxonium consists of a large inductance (and correspondingly small $E_L \sim 1$ GHz) that shunts a Josephson junction with a $E_J/E_C \sim 1$. The large inductance of the fluxonium is supplied by the kinetic inductance of a Josephson junction array. The Hamiltonian is given by:

$$\hat{H} = 4E_C\hat{n}_J^2 + \frac{1}{2}E_L\hat{\varphi}_J^2 - E_J\cos(\hat{\varphi}_J - \varphi_{\text{ext}}). \tag{2.48}$$

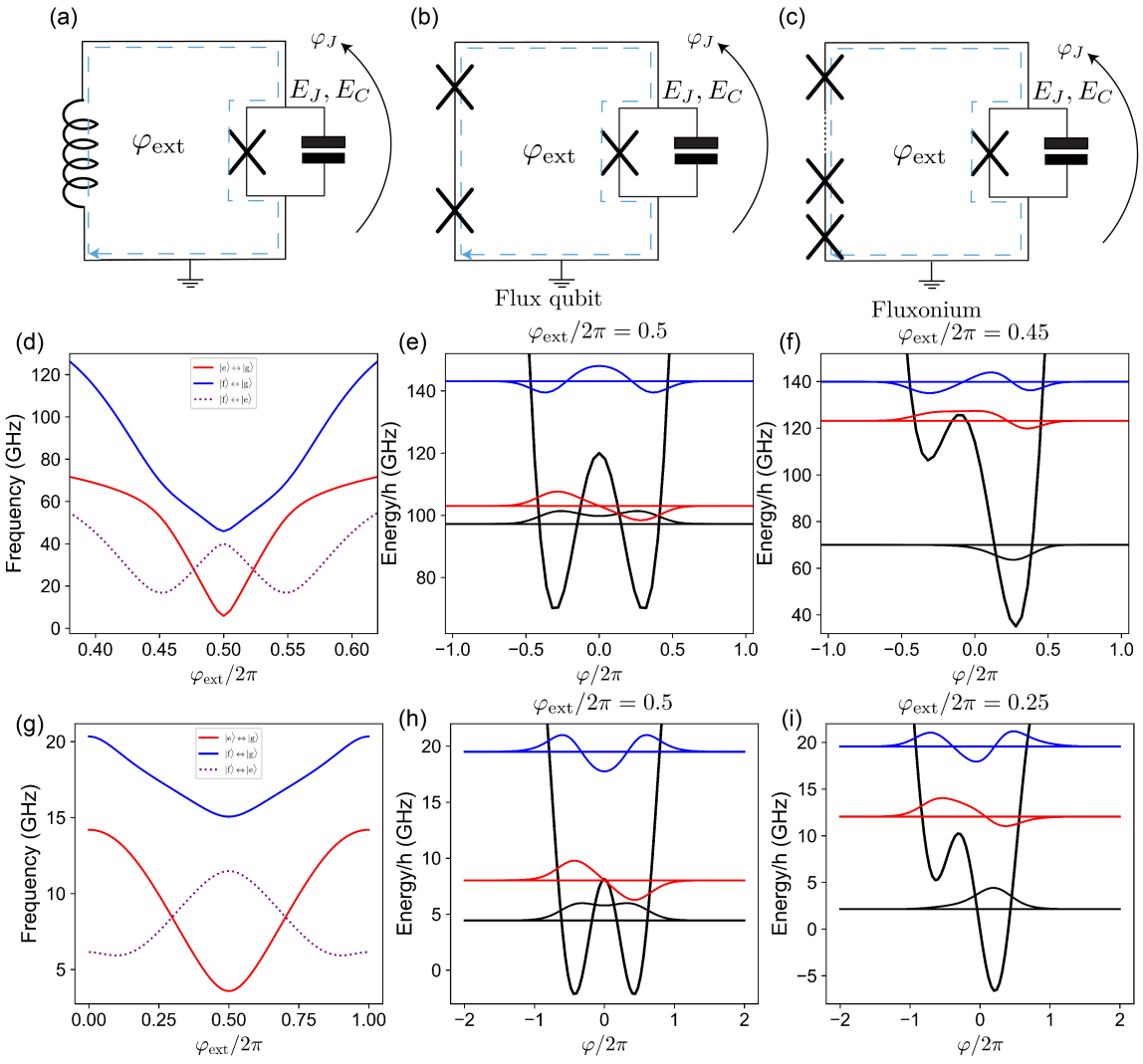

Figure 2.7: (a) Circuit schematic in the most general form of a flux qubit (b,c) Circuit schematic for three junction flux qubit (b) and fluxonium qubit (c). (d-f) Transition energy spectrum, Wavefunction and energy of the first four eigenstates of a three junction flux qubit. (g - i) Same but for fluxonium qubit. Flxuonium parameters used in generating the plots - ($E_J = 8.12$ GHz, $E_C = 5.6$ GHz, $E_L = 1.42$ GHz). FLux qubit parameters used in generating the plots - ($E_J = 120$ GHz, $E_C = 6$ GHz, $E_L = 60$ GHz)

The fluxonium circuit displays rich physics and has a lot of appealing properties which make it a leading qubit for the purposes of quantum computing but for the purposes of the experiments described in chapter 5, its three most important properties are its large anharmonicity, symmetry breaking of its potential and high coherence. All three of these properties are due to the inductive energy term in the Hamiltonian. First, the inductive energy term creates an effective double well potential which can be made asymmetric in φ by the application of a external magnetic flux though the qubit loop (see Fig. 2.7 (g -i)) which is a crucial element for experiments described in chapter 5. This also makes the fluxonium transition spectrum highly anharmonic and allows us to truncate it into an effective two level system. Lastly, the two orders of magnitude higher inductance compared to a three junction flux qubit enables fluxonium to retain a reasonably high coherence time of $5\ \mu$s even when biased away from the half flux sweet spot [68, 69], where the potential displays its asymmetry in φ. The above mentioned reasons make fluxonium the ideal choice of to study the quantum impurity effects in multi-mode cQED as described in chapter 5.

2.4 Coupling between linear and non-linear circuits

In this section we derive the interaction Hamiltonian for circuits where we couple the artificial atoms to the microwave photons. We study in depth two specific multi-mode circuit QED Hamiltonians where an open section of a 1-D transmission line is coupled galvanically to a transmon and a fluxonium atom. Our goal is to construct the interacting circuit Hamiltonian in the form:

$$\hat{H} = \hat{H}_{\text{atom}} + \hat{H}_{\text{modes}} + \hat{H}_{\text{int}}, \tag{2.49}$$

where the first two terms describe respectively an atom and a set of non-interacting bosonic modes hosted by the transmission line, while the third term describes their interaction.

2.4.1 Charge qubit coupled to multi-mode transmission line resonator

Here we derive the circuit Hamiltonian of a transmon circuit galvanically coupled to an open section of a 1-D transmission line. The equivalent circuit schematic and circuit model is shown in Fig. 2.8.

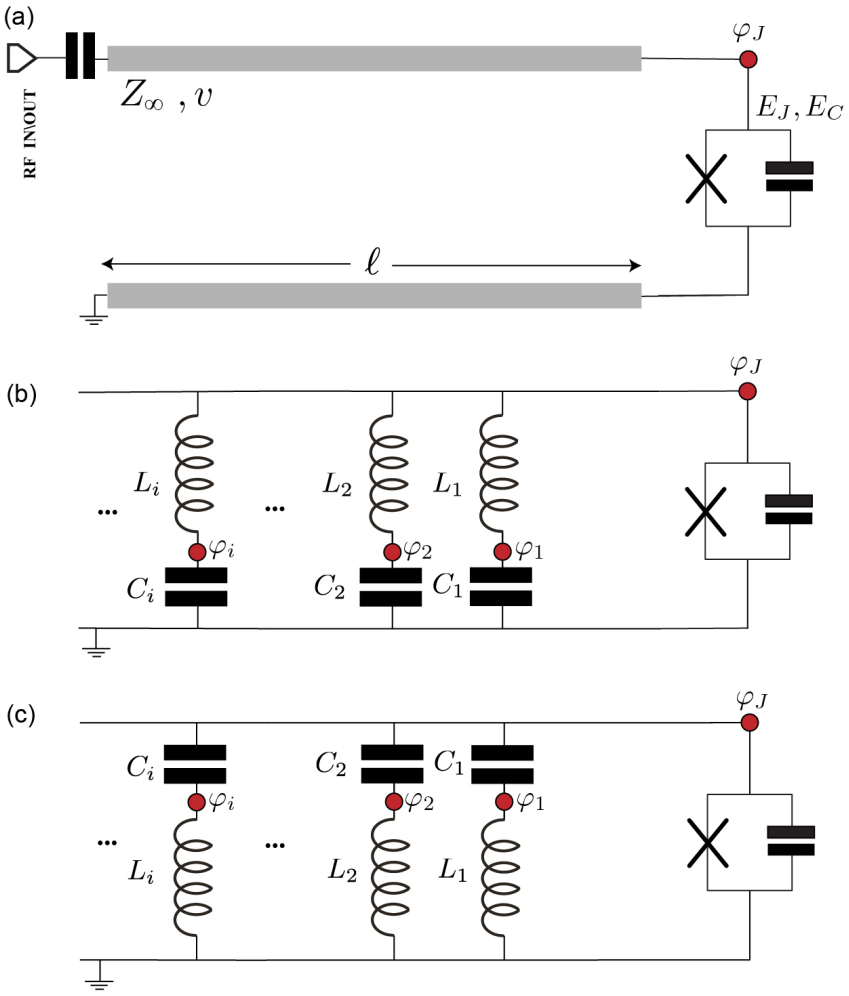

Figure 2.8: (a) Circuit Schematic of a transmon galvanically coopled to an open section of a 1-D transmission line resonator (b, c) Equivalent circuit model in the flux (charge) gauge where the transmission line resonator is replaced by the Foster's decomposition.

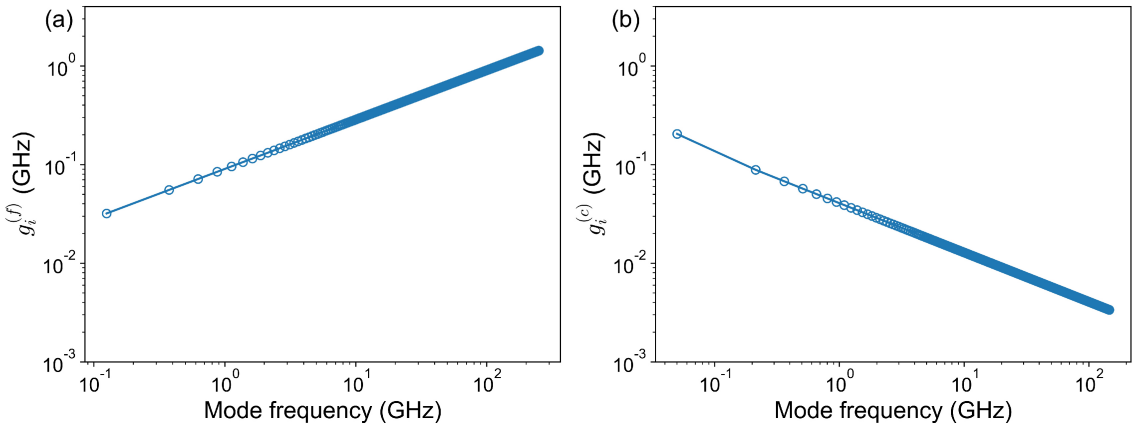

Figure 2.9: Couplings constants calculated in the flux gauge (a) and charge gauge (b) for transmon parameters $E_C = 0.35$ GHz and $E_J = 35$ GHz coupled to a transmission line with $Z_\infty = 10\,\mathrm{K}\Omega$ and speed of light 3×10^8 m/s.

Note that we have two possible choices for the reduced node fluxes for this circuit, we can either use the reduced flux across the capacitors C_i as the node fluxes or we can use the reduced flux across the inductors L_i as the node fluxes. The two choices result in different Hamiltonian but in the end they both describe the same physical system. We call the first choice of variables as the flux gauge since in this description of the circuit the interaction between the transmon and the standing wave modes of the transmission line is mediated by the flux variable and the latter choice as charge gauge since in this cause the interaction is mediated by the charge variable.

2.4.1.1 Flux gauge

For the choice of the node fluxes shown in Fig. 2.8 (b), we can write the classical circuit Lagrangian $\mathfrak{L} = T - V$ with T and V given by:

$$T = \frac{1}{2} C_J \dot{\phi}_J^2 + \sum_{i=1}^{\infty} \frac{1}{2} C_i \dot{\phi}_i^2, \tag{2.50}$$

$$V = -E_J \cos(\varphi_J) + \sum_{i=1}^{\infty} \frac{(\phi_i - \phi_J)^2}{2L_i}.$$

In order to get the Hamiltonian of this circuit, we define the conjugate momenta (charges) to the generalized fluxes shown in Fig. 2.8 (b):

$$q_i = \frac{\partial \mathfrak{L}}{\partial \dot{\phi}_i} = C_i \dot{\phi}_i, \tag{2.51}$$
$$q_J = \frac{\partial \mathfrak{L}}{\partial \dot{\phi}_J} = C_i \dot{\phi}_J,$$

We can arrive at the Hamiltonian by applying Legendre transform and quantizing the classical operators using previously described methods as:

$$\hat{H}_{\text{atom}} = 4E_C \hat{n}_J^2 + \frac{1}{2} E_L \hat{\varphi}_J^2 - E_J \cos(\hat{\varphi}_J), \tag{2.52}$$

$$\hat{H}_{\text{modes}} = \sum_{i=1}^{\infty} \hbar \omega_i \hat{a}_i^\dagger \hat{a}_i, \tag{2.53}$$

$$\hat{H}_{\text{int}} = \sum_{i=1}^{\infty} h g_i^{(f)} (\hat{a}_i + \hat{a}_i^\dagger), \tag{2.54}$$

where $E_C = e^2/2C_J$ and $E_L = (\hbar/2e)^2 \times \sum_i 1/L_i$ and $\omega_i = 1/\sqrt{L_i C_i}$. Unfortunately, in the flux gauge the separation of Hamiltonian (2.49) into the three terms has a number of disturbing properties. To start, the value of the coupling constant $g_i^{(f)}$ grows with i approximately as $i^{1/2}$ (see Fig. 2.9 (a)). Therefore, truncating the model to a finite number of low-energy modes cannot be readily justified. In addition, the transmon Hamiltonian has an additional renormalized inductive energy E_L that also depends on the total number of modes used in the Foster's decomposition of the transmission line (N). In fact, the parameter E_L diverges as $E_L \to \infty$ for $N \to +\infty$. Such a behavior of E_L is problematic for interpreting the dynamics of the renormalized atom's Hamiltonian. We show in the next section that all these problems in the interpretation of the Hamiltonian can be solved by making a gauge transformation.

2.4.1.2 Charge gauge

We can now follow the same procedure as in the last section but for the choice of variables shown in Fig. 2.8 (c). The circuit lagrangian $\mathfrak{L} = T - V$ is then given by:

$$T = \frac{1}{2}C_J\dot{\phi}_J^2 + \sum_{i=1}^{\infty}\frac{1}{2}C_i(\dot{\phi}_i - \dot{\phi}_J)^2 \tag{2.55}$$

$$V = -E_J\cos(\varphi_J) + \sum_{i=1}^{\infty}\frac{\phi_i^2}{2L_i} \tag{2.56}$$

In order to get the Hamiltonian of this circuit, we define the conjugate momenta (charges) to the generalized node fluxes in Fig. 2.8 (c):

$$\begin{aligned} q_J = \frac{\partial\mathfrak{L}}{\partial\dot{\phi}_J} = C_J\dot{\phi}_J + \sum_{i=1}^{\infty}C_i(\dot{\phi}_J - \dot{\phi}_i), \\ q_i = \frac{\partial\mathfrak{L}}{\partial\dot{\phi}_i} = C_i(\dot{\phi}_i - \dot{\phi}_J) \end{aligned} \tag{2.57}$$

By applying the Legendre transform to the Hamiltonian we can get the following Hamiltonian:

$$\hat{H} = 4E_C(\hat{n}_J - \sum_{i=1}^{\infty}\hat{n}_i)^2 - E_J\cos(\hat{\varphi}_J) + \sum_{i=1}^{\infty}4E_{C_i}\hat{n}_i^2 + \frac{1}{2}E_{L_i}\hat{\varphi}_i^2. \tag{2.58}$$

Note that we can also arrive at exactly the same Hamiltonian by applying the unitary trasformation $U = \prod_i e^{\mathrm{i}\hat{\varphi}_J\hat{n}_i}$ to the Hamiltonian in the flux gauge. We can write the Hamiltonian in the form of Eq. 2.49 to get:

$$\hat{H}_{\text{atom}} = 4E_C\hat{n}_J^2 - E_J\cos(\hat{\varphi}_J) \tag{2.59}$$

$$\hat{H}_{\text{modes}} = \sum_{i=1}^{\infty}\hbar\omega_i^{(c)}\hat{a}_i^\dagger\hat{a}_i \tag{2.60}$$

$$\hat{H}_{\text{int}} = -\mathrm{i}\hat{n}_J\sum_{i}^{\infty}hg_i^{(c)}(\hat{a}_i - \hat{a}_i^\dagger) \tag{2.61}$$

Note that in this gauge, all of the disturbing properties of the flux gauge vanish. First, the atom part of the Hamiltonian exactly matches the disconnected transmon Hamiltonian. Second, the coupling between the transmon and the standing wave modes of the transmission line scales as $g_i^{(c)} \sim 1/\sqrt{i}$, such that $g_i^{(c)} \to 0$ as $i \to \infty$, this property allows us to truncate the high frequency modes for numerical calculations.

2.4.2 Flux qubit coupled to multi-mode transmission line resonator

In this section we derive the circuit Hamiltonian of a flux qubit galvanically coupled to an open section of a 1-D transmission line (see Fig. 2.10 (a)). The coupling between the flux qubit and the transmission line is quantitatively characterized by x the ratio of the qubit loop inductance shared with the transmission line. Here we derive the circuit Hamiltonian for our multi-mode cavity QED system in the mixed gauge, whose variable choice is shown in Fig. 2.10 (d). Note that the choice of the parameter i_0 interpolates between the pure charge gauge ($i_0 = 0$) and the pure flux gauge ($i_0 = N$). The variable choices for these specific cases are shown in Fig 2.10 (b, c).

2.4.2.1 Derivation of the circuit Hamiltonian

We link the dependent variable φ_M to the independent variables φ_i with $i = 1, 2, \ldots N$. Using the current conservation at node M, marked by the gray circle in Fig. 2.10 (d), we get:

$$\frac{\varphi_M}{xL} + \frac{\varphi_M}{(1-x)L} + \sum_{i=1}^{i_0} \frac{\varphi_M}{L_i} = \frac{\varphi_J}{(1-x)L} + \sum_{i=1}^{i_0} \frac{\varphi_i}{L_i} - \sum_{i>i_0} \frac{\varphi_i}{L_i}\,. \tag{2.62}$$

We can now write the circuit's classical Lagrangian $\mathfrak{L} = T - V$ in terms of the generalized fluxes $\phi_i = \varphi_i(\hbar/2e)$ and $\phi_J = \varphi_J(\hbar/2e)$. The kinetic and potential energy contributions to the Lagrangian are given by:

$$T = \frac{1}{2}\dot{\boldsymbol{\phi}}^T \mathcal{C} \dot{\boldsymbol{\phi}}\,, \tag{2.63}$$

$$V = \frac{1}{2}\boldsymbol{\phi}^T \mathcal{L}^{-1} \boldsymbol{\phi} - E_J \cos(\varphi_J - \varphi_{\text{ext}})\,, \tag{2.64}$$

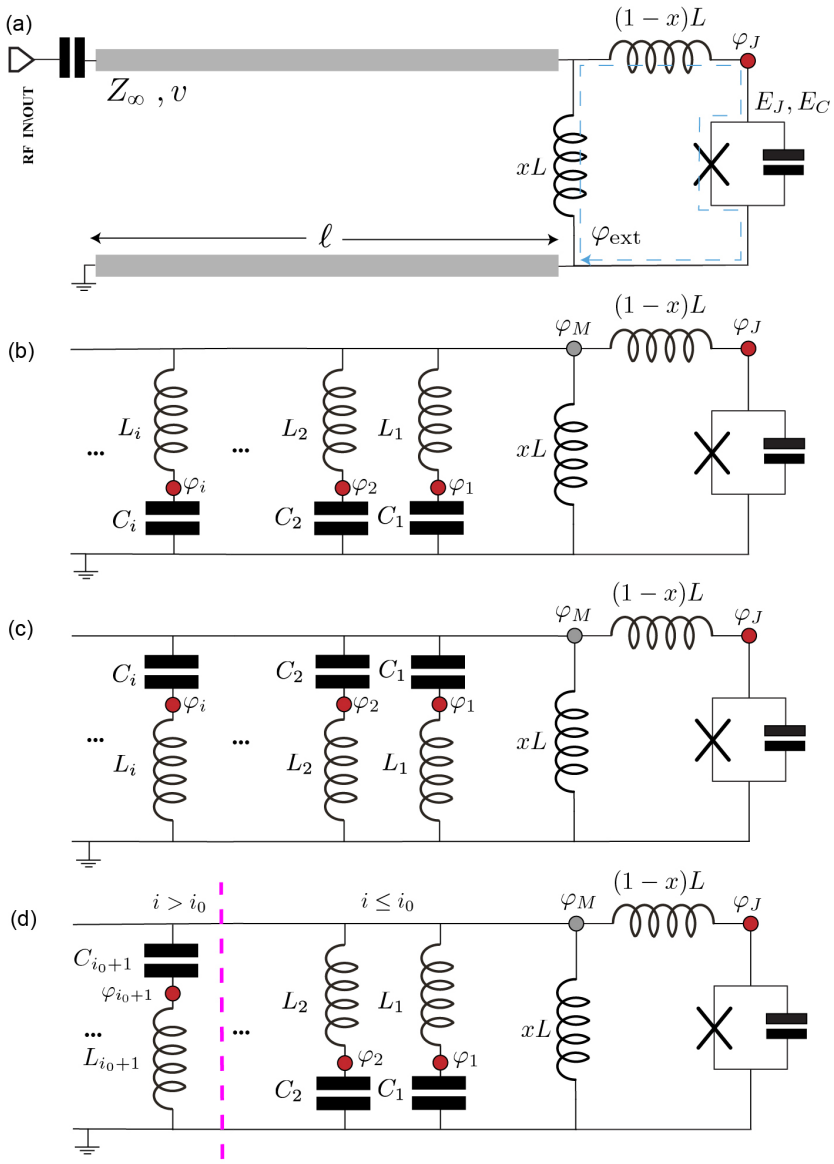

Figure 2.10: (a) Circuit Schematic of a fluxonium galvanically coopled to an open section of a 1-D transmission line resonator (b, c) Equivalent circuit model in the flux (charge) gauge where the transmission line resonator is replaced by the Foster's decomposition. (d) Equivalent circuit model in the hybrid gauge where we interpolated continuously between the pure flux and charge gauges.

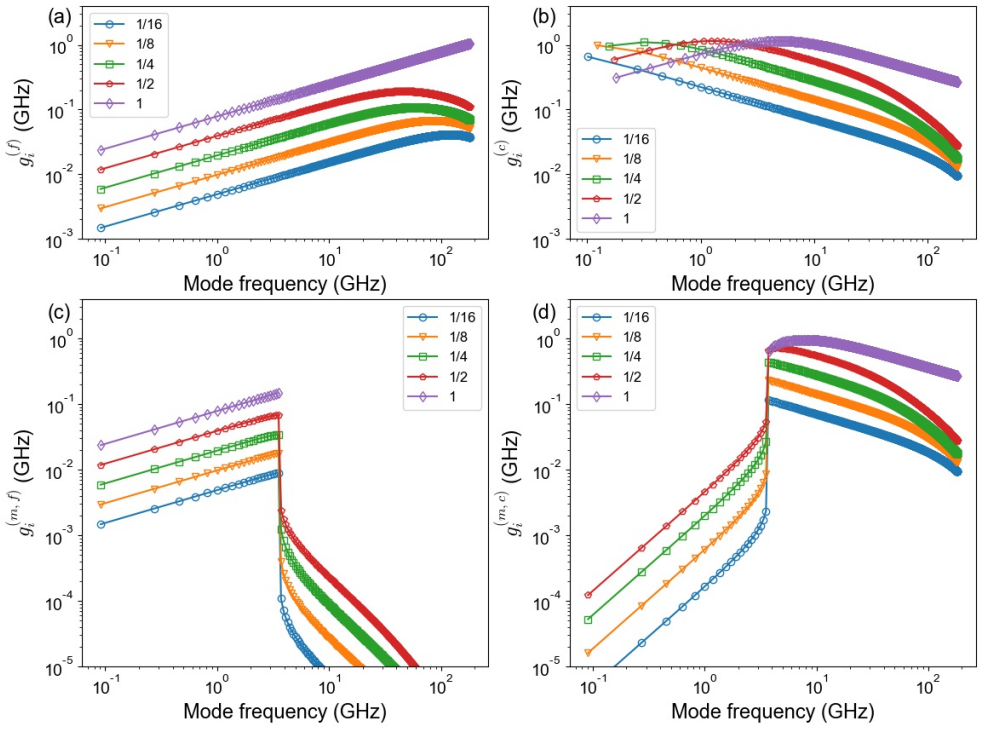

Figure 2.11: Couplings constants calculated in the flux gauge (a), charge gauge (b) and mixed gauge (c, d) for fluxonium ($E_C = 5.6\,\mathrm{GHz}$, $E_J = 8.12\,\mathrm{GHz}$ and $E_L = 1.42\,\mathrm{GHz}$) coupled to a transmission line cavity of length $6\,\mathrm{mm}$ with $Z_\infty = 10\,\mathrm{k\Omega}$ and speed of light $3 \times 10^8\,\mathrm{m/s}$ with varying geometric factors.

where we have defined the vector

$$\boldsymbol{\phi} \equiv (\phi_0 = \phi_J, \phi_1, \phi_2, \ldots \phi_N)\,. \tag{2.65}$$

The symmetric capacitance matrix $\mathcal{C}$ and the symmetric inductance matrix $\mathcal{L}$ have the following matrix elements:

$$\mathcal{C}_{0,0} = C_J + \tilde{x}^2 \sum_{j>i_0} C_j\,, \tag{2.66}$$

$$\mathcal{C}_{0,0<i\leq i_0} = -\tilde{x}\frac{L_\Sigma}{L_i}\sum_{j>i_0} C_j\,, \tag{2.67}$$

$$\mathcal{C}_{0,i>i_0} = -\tilde{x}C_i - \tilde{x}\frac{L_\Sigma}{L_i}\sum_{j>i_0} C_j\,, \tag{2.68}$$

$$\begin{aligned}\mathcal{C}_{i\neq 0,j\neq 0} = C_i\delta_{i,j} + \frac{L_\Sigma}{L_j}C_i\Theta[i-i_0-1] \\ +\frac{L_\Sigma}{L_i}C_j\Theta[j-i_0-1] + \frac{L_\Sigma}{L_i}\frac{L_\Sigma}{L_j}\sum_{k>i_0} C_k\,,\end{aligned} \tag{2.69}$$

$$(\mathcal{L}^{-1})_{0,0} = \frac{(1-\tilde{x})}{(1-x)L}, \tag{2.70}$$

$$(\mathcal{L}^{-1})_{0,0<i\leq i_0} = \frac{\tilde{x}}{L_i}\,, \tag{2.71}$$

$$(\mathcal{L}^{-1})_{0,i>i_0} = 0\,, \tag{2.72}$$

$$(\mathcal{L}^{-1})_{i\neq 0,j\neq 0} = \delta_{i,j}\frac{1}{L_i} + \frac{L_\Sigma}{L_i L_j}\Theta[i-i_0-1]\Theta[j-i_0-1]\,, \tag{2.73}$$

where the variables L_Σ and $\tilde{x}$ are given by:

$$L_\Sigma = \left(\frac{1}{xL} + \frac{1}{(1-x)L} + \sum_{i=1}^{i_0}\frac{1}{L_i}\right)^{-1}, \tag{2.74}$$

$$\tilde{x} = \frac{L_\Sigma}{(1-x)L}. \tag{2.75}$$

Note that Θ is the discrete Heaviside step function. Note that for the case of pure charge gauge, $L_\Sigma = x(1-x)L$ and $\tilde{x} \to x$.

In order to derive the Hamiltonian of this circuit, we define the conjugate momenta (charges) to the generalized coordinates shown in Fig. 2.10 (c):

$$\boldsymbol{q} = \frac{\partial \mathfrak{L}}{\partial \dot{\boldsymbol{\phi}}} = \mathcal{C}\dot{\boldsymbol{\phi}}\,. \tag{2.76}$$

The Hamiltonian can be obtained by applying a Legendre transform to the Lagrangian:

$$H = \boldsymbol{q}^T\dot{\boldsymbol{\phi}} - \mathfrak{L} = \frac{1}{2}\boldsymbol{q}^T\mathcal{C}^{-1}\boldsymbol{q} + \frac{1}{2}\boldsymbol{\phi}^T\mathcal{L}^{-1}\boldsymbol{\phi} - E_J\cos(\varphi_J - \varphi_{\text{ext}})\,. \tag{2.77}$$

The circuit Hamiltonian can be written as a sum of three parts. The atomic part of the Hamiltonian reads:

$$H_{\text{atom}} = 4E_C n_J^2 + \frac{1}{2}\tilde{E}_L\varphi_J^2 - E_J\cos(\varphi_J - \varphi_{\text{ext}})\,, \tag{2.78}$$

where $E_C = e^2(\mathcal{C}^{-1})_{0,0}/2$ and $\tilde{E}_L = (\hbar/2e)^2(\mathcal{L}^{-1})_{0,0}$, which formally depends on the $(0,0)$ element of the inverse capacitance and inductance matrices. Remarkably, it can be proved analytically that $(\mathcal{C}^{-1})_{0,0} = 1/C_J$, irrespective of choice of i_0 and $(\mathcal{L}^{-1})_{0,0} = 1/L$ for $i_0 = 0$. This is relevant, because it shows that the atom Hamiltonian defined in Eq. (2.78) is not renormalized by the transmission

line parameters and depends only on the bare fluxonium parameters for the pure charge gauge. Whereas in the mixed gauge the atom inductive energy is renormalized and is a function of both x and i_0. The worst case scenario occurs for the flux gauge where the inductive energy of the atom now depends on the number of modes included in the lumped element Foster's decomposition of the transmission line. The renormalization of the inductive energy as a function of the total number of modes included in the flux gauge is shown in Fig 2.12.

The photonic part of the Hamiltonian, which is quadratic in the charge and flux variables, reads:

$$H_{\text{modes}} = \frac{1}{2}\sum_{i,j=1}^{N} (\mathcal{C}^{-1})_{i,j}\, q_i q_j + \frac{1}{2}\sum_{i,j=1}^{N} (\mathcal{L}^{-1})_{i,j}\phi_i\phi_j \,. \tag{2.79}$$

Finally, the interaction between the fluxonium degrees of freedom and the transmission line modes is given by:

$$H_{\text{int}} = q_J \sum_{i=1}^{N} (\mathcal{C}^{-1})_{0,i} q_i - \phi_J \sum_{i=1}^{N} (\mathcal{L}^{-1})_{0,i}\phi_i \,. \tag{2.80}$$

2.4.2.2 Renormalization due to the diamagnetic terms

In order to quantize the classical Hamiltonian we introduce photon annihilation (creation) operators $\hat{a}_i(\hat{a}_i^\dagger)$ as:

$$\hat{q}_i = \mathrm{i}\sqrt{\frac{\hbar}{2R_Q}}(\hat{a}_i - \hat{a}_i^\dagger)\,, \tag{2.81}$$

$$\hat{\phi}_i = \sqrt{\frac{\hbar R_Q}{2}}(\hat{a}_i + \hat{a}_i^\dagger)\,, \tag{2.82}$$

where $R_Q = h/4e^2$ is the superconducting resistance quantum. Note that any other resistance value could be used as the dummy operators $\hat{a}_i$ ($\hat{a}_i^\dagger$) merely define a starting basis for the cavity modes. The operator $\hat{H}_{\text{modes}}$ can be diagonalized via a Bogoliubov transformation, because it is a quadratic function of the photon operators. To proceed, we introduce a vector of annihilation operators $\hat{\boldsymbol{a}}$:

$$\hat{\boldsymbol{a}}^T \equiv (\hat{a}_1, \hat{a}_2 \ldots \hat{a}_N)\,. \tag{2.83}$$

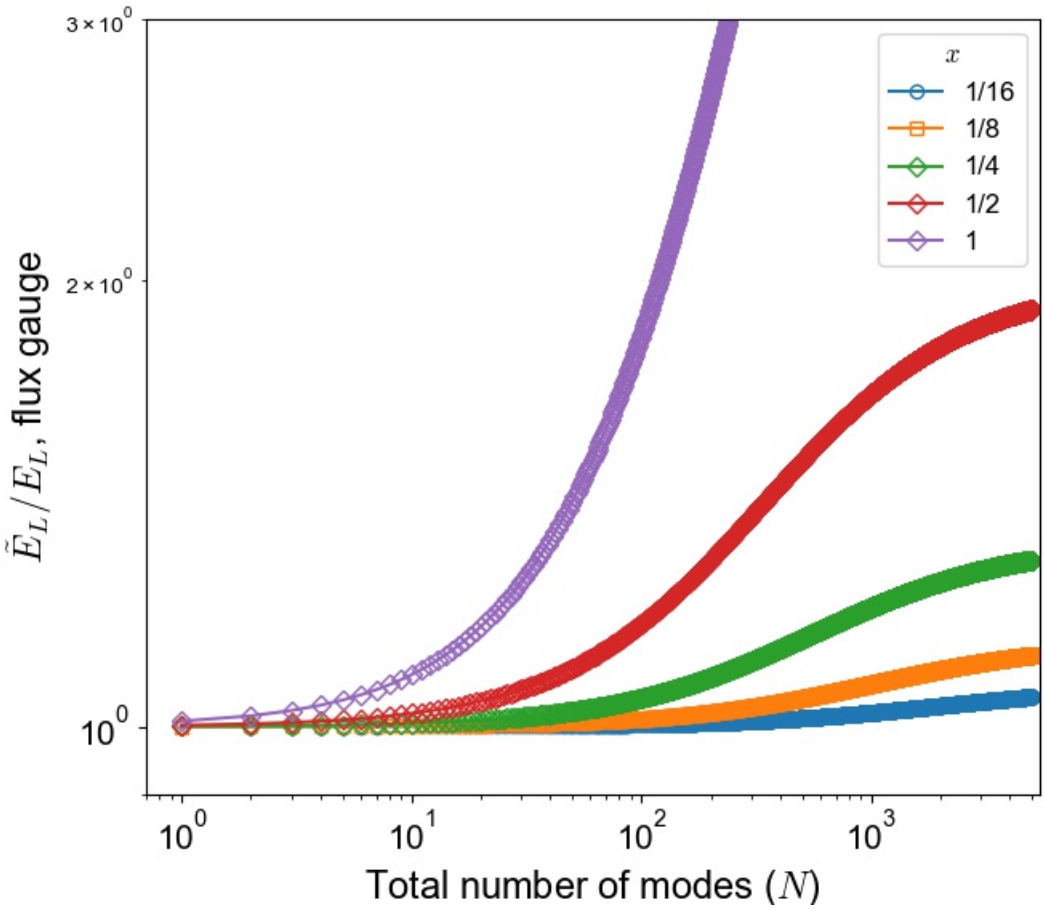

Figure 2.12: Relative renormalization of the inductive energy of the fluxonium atom in the flux gauge as a function of the total number N of modes included in the Foster's decomposition of the transmission line. Same parameters as in Fig. 2.11. The legend indicates the values of the geometric fraction x.

The Hamiltonian H_{modes} can be rewritten in the following matrix form:

$$\hat{H}_{\text{modes}} = \frac{1}{2}(\hat{\boldsymbol{a}}^{\dagger,T}, \hat{\boldsymbol{a}}^{T})\eta\mathcal{M}\begin{pmatrix}\hat{\boldsymbol{a}}\\ \hat{\boldsymbol{a}}^{\dagger}\end{pmatrix} = \frac{1}{2}(\hat{\boldsymbol{b}}^{\dagger,T}, \hat{\boldsymbol{b}}^{T})\eta\Omega\begin{pmatrix}\hat{\boldsymbol{b}}\\ \hat{\boldsymbol{b}}^{\dagger}\end{pmatrix}, \tag{2.84}$$

where η is the diagonal $2N \times 2N$ matrix such that $\eta_{ii} = 1$ for $i \leq N$ and $\eta_{ii} = -1$ for $i > N$. The other $2N \times 2N$ matrix to deal with is:

$$\mathcal{M} = \begin{pmatrix}\mathcal{X} & \mathcal{Y}\\ -\mathcal{Y} & -\mathcal{X}\end{pmatrix}. \tag{2.85}$$

The symmetric $N \times N$ matrices $\mathcal{X}$ and $\mathcal{Y}$ are defined as:

$$\mathcal{X}_{i,j} = R_Q(\mathcal{L}^{-1})_{i,j} + R_Q^{-1}(\mathcal{C}^{-1})_{i,j}\,, \tag{2.86}$$

$$\mathcal{Y}_{i,j} = R_Q(\mathcal{L}^{-1})_{i,j} - R_Q^{-1}(\mathcal{C}^{-1})_{i,j}\,, \tag{2.87}$$

where $i, j \in \{1, 2, ..., N\}$. Finally the diagonal matrix $\Omega = diag(\omega_1, \omega_2, .., \omega_N, -\omega_1, -\omega_2, ..., -\omega_N)$ contains the frequencies of the normal Bogoliubov modes. It is defined as $\mathcal{M} = \mathcal{Q}\Omega\mathcal{Q}^{-1}$, so that the Bogoliubov mode operators are:

$$\begin{pmatrix}\hat{\boldsymbol{b}}\\ \hat{\boldsymbol{b}}^{\dagger}\end{pmatrix} = \mathcal{Q}^{-1}\begin{pmatrix}\hat{\boldsymbol{a}}\\ \hat{\boldsymbol{a}}^{\dagger}\end{pmatrix}, \tag{2.88}$$

where the matrix $\mathcal{Q}$ can be expressed in the form :

$$\mathcal{Q} = \begin{pmatrix}V & U\\ -U & -V\end{pmatrix}. \tag{2.89}$$

The Hamiltonian $\hat{H}_{\text{modes}}$ can be diagonalized in terms of bosonic normal-mode operators $\hat{b}_i$ ($\hat{b}_i^{\dagger}$):

$$\hat{H}_{\text{modes}} = \sum_{i=1}^{N} \hbar\omega_i^{(m)}\hat{b}_i^{\dagger}\hat{b}_i\,, \tag{2.90}$$

where $\omega_i^{(m)}$ are the corresponding normal-mode frequencies.

The coupling of the atom to the transmission line is represented by the interaction Hamiltonian:

$$\hat{H}_{\text{int}} = \mathrm{i}\hat{n}_J \frac{4}{\pi^{1/2}} E_C \sum_{i=1}^{N} (\mathcal{C}^{-1} C_J)_{0,i} (\hat{a}_i - \hat{a}_i^\dagger) \\ -\hat{\varphi}_J \frac{E_L}{4\pi^{3/2}} \sum_{i=1}^{N} (\mathcal{L}^{-1} L)_{0,i} (\hat{a}_i + \hat{a}_i^\dagger)\,. \tag{2.91}$$

In order to express H_{int} in terms of the normal-mode transmission line operators $\hat{b}_\nu$, we need to invert the Bogoliubov transformation as follows:

$$\hat{a}_i = \sum_{\nu=1}^{N} V_{i,\nu} \hat{b}_\nu + \sum_{\nu=1}^{N} U_{i,\nu} \hat{b}_\nu^\dagger\,. \tag{2.92}$$

Note that the conservation of the bosonic commutation rules, i.e., $[b_\nu, b_{\nu'}^\dagger] = \delta_{\nu,\nu'}$, imposes the following normalization condition for the Bogoliubov transformation coefficients:

$$\sum_{i=1}^{N} U_{i,\nu}^2 - V_{i,\nu}^2 = 1\,. \tag{2.93}$$

2.4.2.3 The mixed gauge QED Hamiltonian

We have now all the ingredients to formulate the multi-mode cavity QED Hamiltonian in terms of the fluxonium operators $\hat{\varphi}_J$, $\hat{n}_J$, and the transmission line normal mode operators $\hat{b}_i$ ($\hat{b}_i^\dagger$). The total Hamiltonian is $H = H_{\text{atom}} + H_{\text{modes}} + H_{\text{int}}$, where H_{atom} is given by Eq. (2.78), H_{modes} is given by Eq. (2.90) and H_{int} can be expressed as:

$$\hat{H}_{\text{int}} = \mathrm{i}\hat{n}_J \sum_{i=1}^{N} h g_i^{(m,c)} (\hat{b}_i - \hat{b}_i^\dagger) \\ -\varphi_J \sum_{i=1}^{N} h g_i^{(m,f)} (\hat{b}_i - \hat{b}_i^\dagger)\,, \tag{2.94}$$

with the mixed gauge coupling constants given by:

$$hg_i^{(m,c)} = \frac{4}{\pi^{1/2}} E_C \sum_{j=1}^{N} (\mathcal{C}^{-1} C_J)_{0,j} (V_{j,i} - U_{j,i}) \,, \tag{2.95}$$

$$hg_i^{(m,f)} = \frac{1}{4\pi^{3/2}} E_L \sum_{j=1}^{N} (\mathcal{L}^{-1} L)_{0,j} (V_{j,i} + U_{j,i}) \,. \tag{2.96}$$

Note that for the special case of $i_0 = 0$ (charge gauge) the flux coupling constants are identically zero and for the case of $i_0 = N$ (flux gauge) the charge coupling constants are identically zero. Moreover, the flux coupling constants in the mixed gauge $g_i^{(m,f)}$ for $i < i_0$ can be written analytically as:

$$hg_i^{(m,f)} = \hbar \omega_i^{(m)} x \sqrt{\frac{R_Q}{4\pi Z_\infty (i + 1/2)}} \,. \tag{2.97}$$

Chapter 3

Experimental Techniques

In this chapter we summarize the main experimental methods used throughout this thesis.

3.1 Nanofabrication

Fabrication of all the devices described in this work was done following well established techniques evolved from more than two decades of extensive research on superconducting circuits [70]. All our devices are fabricated on high resistivity Si of thickness $380\ \mu\mathrm{m}$. The Josephson junctions in our devices are Al-Alox-Al tunnel junctions. These use aluminium oxide as the insulating layer in the tunnel junction. We choose this because the growth of aluminum oxide is unique in that it is self-terminating and thus has reliable thickness. This is important as the critical current and thus the Josephson energy (E_J) is exponentially sensitive to the width of the insulating layer. In addition there has been much study in use of these junction and methods have been found to grow low loss junctions [71].

To fabricate the Josephson junctions in the device we used the Dolan bridge technique. Also known as the shadow evaporation technique, this fabrication method allows small, overlapping structures to be fabricated with very high accuracy and reproducibility. [72]. We use a chip size of $9\ \mu\mathrm{m} \times 16\ \mu\mathrm{m}$ to pattern our devices. A double layer resist of MMA ($500\ \mathrm{nm}$) and PMMA ($100\ \mathrm{nm}$)

is applied before using a Elionix electron bean lithography to pattern the device features. After development of the patterns, Al deposition and growth of the Alox was performed using a Plassys e-beam evaporation system. We used the double angle method where we deposited $20\ \mathrm{nm}$ of Al at a rate of $1\ \mathrm{nm}/sec$. The Alox growth was done at $100\ \mathrm{mBar}$ pressure for $20\ \mathrm{mins}$. The second layer of $40\ \mathrm{nm}$ Al deposition was done before a final oxidation at $10\ \mathrm{mBar}$ to give a capping layer for a consistent top surface of the junctions.

3.2 Microwave reflectometry setup

3.2.1 Cryogenic setup

Our experiments were performed in a Blue Fors dilution refrigerator with a base temperature of $7-15\mathrm{mK}$. We used a bottom loader dilution refregirator which allowed us to exchange samples without warming up the whole unit in a relatively fast time scale of $7\,\mathrm{Hours}$. This was crucial in being able to cycle through a lot of devices. The input line was attenuated by $60\mathrm{dBm}$ to suppress the thermal noise coming in from higher temperature stages of the refrigerator. The placement of the attenuators was guided by the cooling power at different stages (see Fig. 3.1). Since the measurements were done in a reflection geometry, we used a Pasternack directional coupler $(2-20\,\mathrm{GHz})$ to physically separate the input and output signals. Note that the input signal was attenuated by an additional $16\ \mathrm{dBm}$ becacuse of the directional coupler. The reflected signal was directed to a Caltech HEMT (High Electron Mobility Transistor) cryogenic amplifier with a $35\ \mathrm{dB}$ gain and $5\ \mathrm{K}$ noise temperature in a broad frequency range of $4-12\ \mathrm{GHz}$. Two Quinstar isolators $(4-12\ \mathrm{GHz})$ were connected before the amplifier to guard the sample from any spurious microwaves travelling back on the output lines especially from the HEMT amplifier. All the components were thermally anchored to their respective stages. An in house built $3.6\ \mathrm{cm}$ radius superconducting solenoid coil was attached to the cold finger of the refrigerator to provide uniform perpendicular magnetic field used to flux bias the superconducting loops of the SQuID transmon and fluxonium qubits. The coil was connected to a

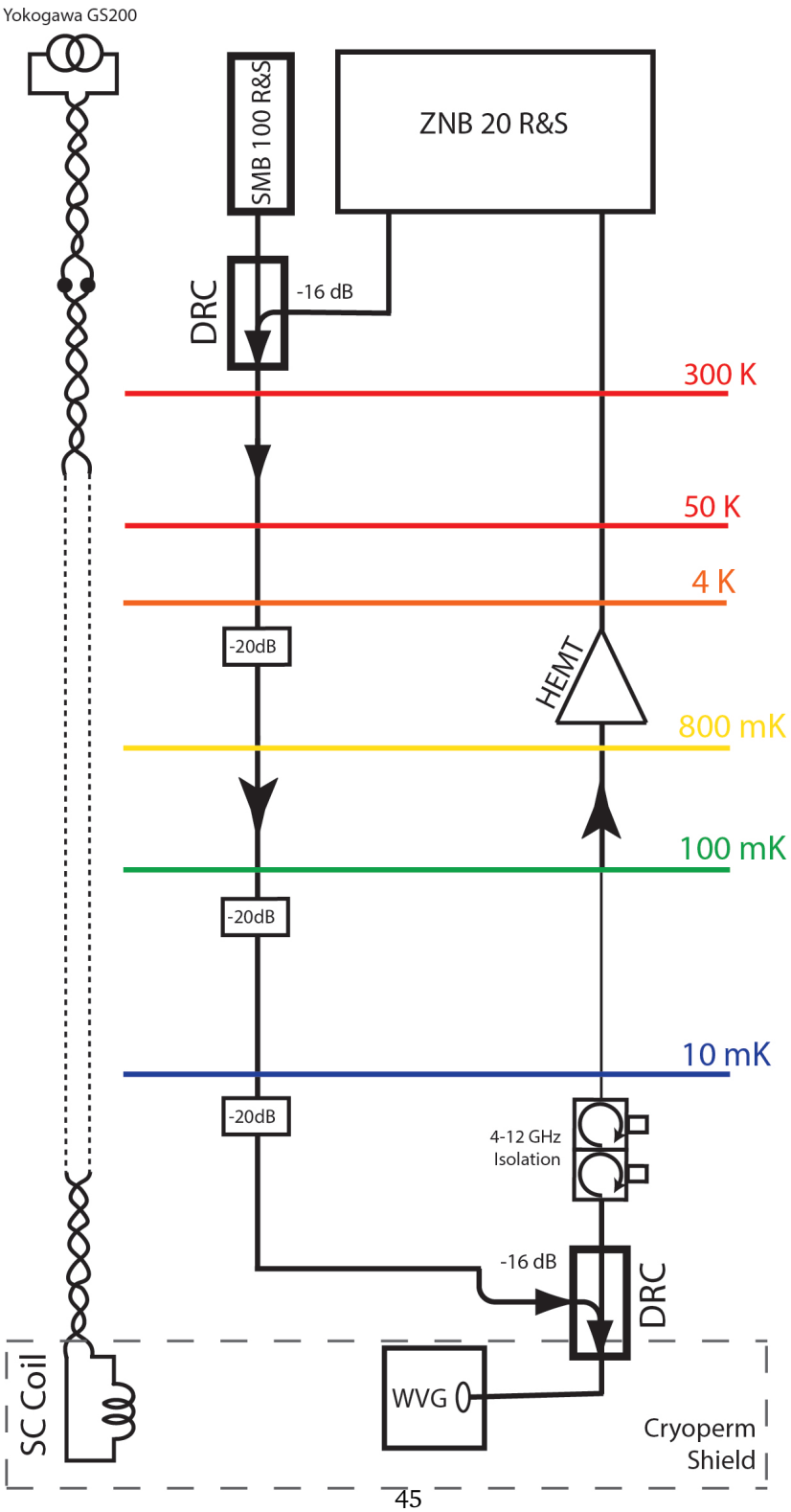

Figure 3.1: The full microwave reflectometery setup used in the experiments and described in detail in section 3.2.

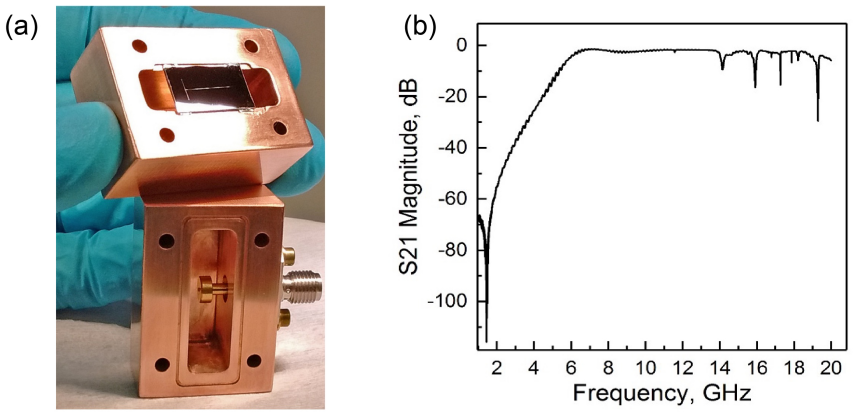

Figure 3.2: (a) Optical image of the 3-D copper waveguide sample holder. The image shows the placement of a sample silicon chip in the box and the launcher used to couple microwaves from coaxial cable to the chip. (b) Transmission signal measured when the waveduide box is empty at room temperature.

Yokogawa GS 200 DC current source at room temperature using a $30\ \Omega$ twisted pair wire. The 3-D waveguide sample holder was bolted to the cold finger of the dilution refrigerator and a Cryoperm cylinder was used to shield the flux sensitive devices from stray magnetic fields.

3.2.2 3-D waveguide sample holder

The devices were placed in a 3-D waveguide sample holder for measurements. The waveguide consists of a $9\ \mathrm{mm} \times 27\ \mathrm{mm} \times 25\ \mathrm{mm}$ copper box with two SMA ports. One port was permanently connected to a cryogenic $50\ \Omega$ termination. The other port was connected to a coax to waveguide launcher used to guide microwaves travelling on the coaxial lines into the copper waveguide. The launcher and cooper box dimension were chosen such that we have a relatively uniform coupling in the frequency range of $5 - 10\ \mathrm{GHz}$. We would like to stress at this point that we did not use any wire-bonding to couple microwaves into our devices. This setup minimizes the typical parasitic capacitances due to the measurement setup seen by the devices and helps to get a clean spectroscopy signal.

3.2.3 Room temperature setup

All measurements described in this work are done with continuous wave RF signals, we were able to get by with a relatively simple room temperature electronics setup. The main equipment in our setup was the $4-\mathrm{Port}$ ZNB20 Rohde and Schwarz VNA (Vector Network Analyzer). The ability of the VNA to perform fast measurement and demodulation of reflection signals was vital in obtaining the spectroscopy results presented in chapters $4-6$. For two-tone experiments the additional tone was combined using a directional coupler identical to the one used in the cryogenic setup.

Chapter 4

Multi-mode Fabry-Perot cavity

In this chapter we describe the experimental implementation and characterization of multi-mode Fabry-Perot cavities made using a long array of Josephson junctions. We present reflection spectroscopy measurements of such Fabry-Perot cavities. Using these measurements we extract the dispersion of the standing wave modes and their intrinsic lifetime.

4.1 Josephson junction transmission line

Our transmission line consists of two parallel chains of large area Josephson junctions separated by $2-10\ \mu\mathrm{m}$ fabricated on an insulating silicon chip. The junctions are Al/Alox Josephson junctions fabricated using the Dolan bridge method described in detail in section 3.1. Typical junction dimensions used are $1-3\ \mu\mathrm{m} \times 0.4\ \mu\mathrm{m}$ which translates to $E_J/E_C \gtrsim 100$. This safely places the junctions in the linear regime where the Josephson junction can be considered an oscillator with a linearized inductance given by Eq. 2.20. The inductance per junction in the transmission lines is of the order of a few nH, which makes it approximately 10^4 times larger than a wire of similar dimensions. An optical micrograph of a typical transmission line fabricated along with the SEM micrograph of the Josephson junctions is shown in Fig. 4.1 (a), (b) respectively. The minimal circuit model of our transmission line (see 4.1 (d)) includes two linear chains of Josephson junctions with energy E_J

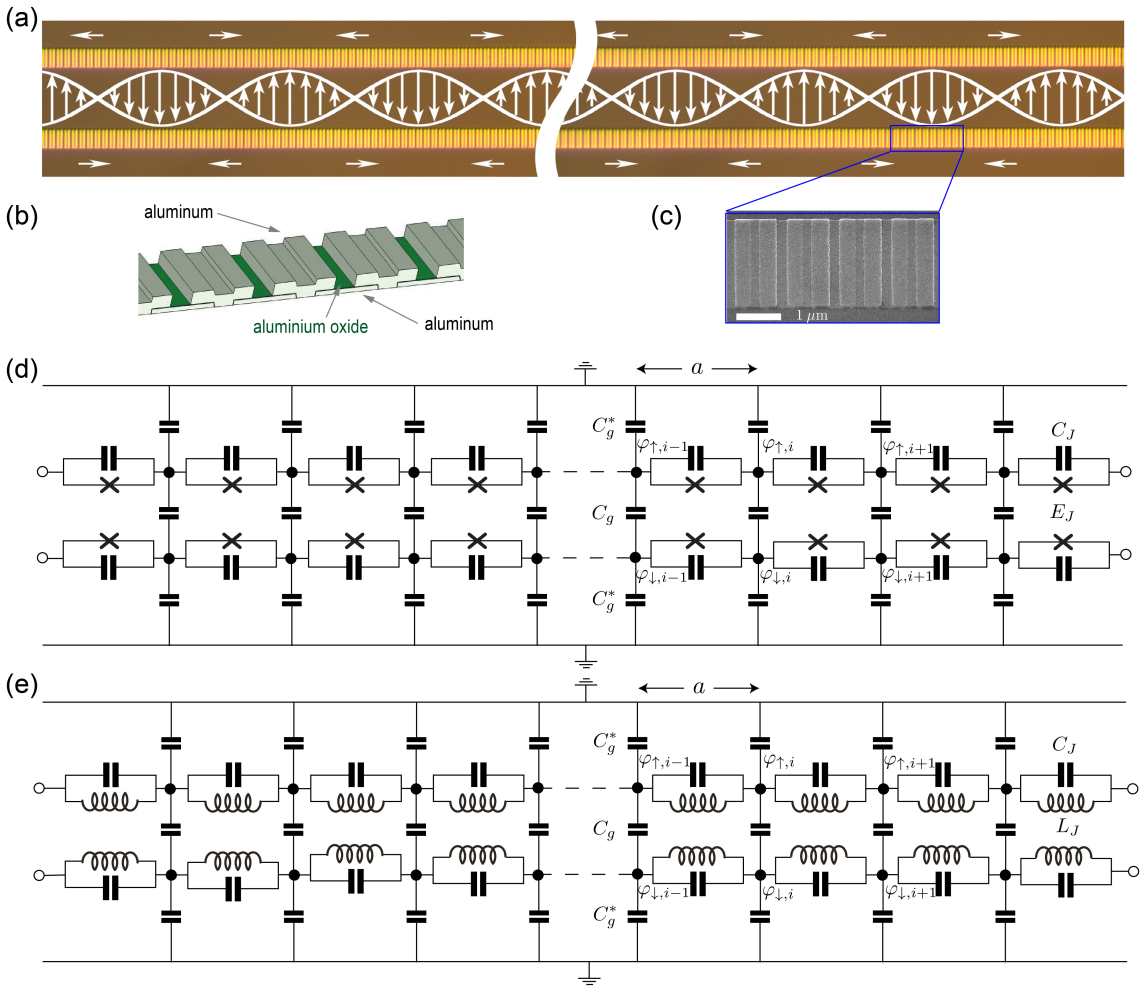

Figure 4.1: (a) Optical image of a section of high-impedance transmission line made of array of Josephson junctions. (b) Schematic of an array of Josephson junctions. (c) Scanning electron micrograph of an array of Josephson junctions. (d) Exact Circuit model of the transmission line. (e) Circuit model of the transmission line in the linear approximation.

in parallel with the Josephson capacitance C_J coupled with the inter-chain capacitance C_g and connected to ground by the capacitance C_g^*. The unit cell size of the array of Josephson junctions is $a = 0.6\,\mu\text{m}$.

4.1.1 Transmission line Lagrangian

We follow the procedure outlined in section 2.2.2 to arrive at the circuit Lagrangian of the transmission line for the choice of reduced node flux variables shown in Fig 4.1 (d).

$$\mathfrak{L} = T - V, \tag{4.1}$$

where the kinetic energy is given by:

$$T = \sum_i \frac{(\dot{\varphi}_{\uparrow,i} - \dot{\varphi}_{\uparrow,i-1})^2}{2E_C} + \sum_i \frac{(\dot{\varphi}_{\downarrow,i} - \dot{\varphi}_{\downarrow,i-1})^2}{2E_C} + \sum_i \frac{(\dot{\varphi}_{\uparrow,i} - \dot{\varphi_{\downarrow,i}})^2}{2E_g} + \sum_i \frac{\dot{\varphi}_{\uparrow,i}^2}{2E_g^*} + \sum_i \frac{\dot{\varphi}_{\downarrow,i}^2}{2E_g^*}, \tag{4.2}$$

and the potential energy is given by:

$$V = -\sum_i \left(E_J \cos\left(\varphi_{\uparrow,i} - \varphi_{\uparrow,i-1}\right) + E_J \cos\left(\varphi_{\downarrow,i} - \varphi_{\downarrow,i-1}\right)\right). \tag{4.3}$$

It is convenient to work in the continuum limit and write the Lagrangian of the system as:

$$\begin{aligned}\mathfrak{L} = \int dx \Big[&\frac{(\partial_x \dot{\varphi}_\uparrow(x,t))^2 a}{2E_C} + \frac{(\partial_x \dot{\varphi}_\downarrow(x,t))^2 a}{2E_C} + \frac{(\dot{\varphi}_\uparrow(x,t) - \dot{\varphi}_\downarrow(x,t))^2}{2E_g a} + \\ &\frac{\dot{\varphi}_\uparrow^2(x,t)}{2E_g^* a} + \frac{\dot{\varphi}_\downarrow^2(x,t)}{2E_g^* a} + \frac{E_J}{a}[\cos(\partial_x \varphi_\uparrow a) + \cos(\partial_x \varphi_\downarrow a)]\Big].\end{aligned} \tag{4.4}$$

We define new variables $\varphi_+(x,t) = \varphi_\uparrow(x,t) + \varphi_\downarrow(x,t)$ and $\varphi_-(x,t) = \varphi_\uparrow(x,t) - \varphi_\downarrow(x,t)$ to get the following Lagrangian:

$$\begin{aligned}\mathfrak{L} = \int dx \Big[&\frac{(\partial_x \dot{\varphi}_-(x,t))^2 a}{4E_C} + \frac{(\partial_x \dot{\varphi}_+(x,t))^2 a}{4E_C} + \frac{(\dot{\varphi}_-(x,t))^2}{2a}\Big(\frac{1}{E_g} + \frac{1}{2E_g^*}\Big) + \frac{(\partial_x \dot{\varphi}_+(x,t))^2}{4E_g^* a} \\ &+ \frac{2E_J}{a}[\cos(\frac{1}{2}\partial_x \varphi_-(x,t)a) \times \cos(\frac{1}{2}\partial_x \varphi_+(x,t)a)]\Big].\end{aligned} \tag{4.5}$$

Since we work with large area Josephson junctions in this chapter such that the E_J/E_C of each junction is $\gg 1$. Each individual junction in our transmission line can be thought of as a harmonic oscillator. As was discussed in section 2.1.3 it is safe to approximate the cosine potential to its lowest order to give us a quadratic Lagrangian. The Lagrangian can be separated into two parts as:

$$\begin{aligned} \mathfrak{L} &= \mathfrak{L}_- + \mathfrak{L}_+, \\ \mathfrak{L}_- &= \int dx \Big[\frac{(\dot{\varphi}_-(x,t))^2}{2a} \Big(\frac{1}{E_g} + \frac{1}{2E_g^*} \Big) + \frac{(\partial_x \dot{\varphi}_-(x,t))^2 a}{4E_C} - \frac{E_J a}{4} (\partial_x \varphi_-)^2 \Big], \\ \mathfrak{L}_+ &= \int dx \Big[\frac{(\partial_x \dot{\varphi}_+(x,t))^2}{4E_g^* a} + \frac{(\partial_x \dot{\varphi}_+(x,t))^2 a}{4E_C} - \frac{E_J a}{4} (\partial_x \varphi_+)^2 \Big]. \end{aligned} \tag{4.6}$$

We now write the Euler Lagrange equations of motion for the two Lagrangians to get the wave equation satisfied by the waves propagating in this transmission line:

$$\begin{aligned} \frac{a}{2E_C} \partial_x^2 \partial_t^2 \varphi_-(x,t) + \frac{E_J a}{2} \partial_x^2 \varphi_-(x,t) - \frac{1}{\tilde{E}_g a} \partial_t^2 \varphi_-(x,t) = 0, \\ \frac{a}{2E_C} \partial_x^2 \partial_t^2 \varphi_+(x,t) + \frac{E_J a}{2} \partial_x^2 \varphi_+(x,t) - \frac{1}{E_g^* a} \partial_t^2 \varphi_+(x,t) = 0, \end{aligned} \tag{4.7}$$

here we have defined the effective ground charging energy for the differential mode as $\tilde{E}_g^{-1} = E_g^{-1} + (2E_g^*)^{-1}$. The equations in Eq. 4.7 define two separate modes of propagation of the plane waves in the transmission line each corresponding to the oscillations of the voltage and current defined by the superconducting phase density $\varphi_+(x,t)$ (common mode) and $\varphi_-(x,t)$ (differential mode). The common mode corresponds to the voltage oscillating in phase in the upper and lower chains while the differential mode corresponds to the voltage oscillating out of phase in the upper and lower chains.

4.1.2 Multi-mode Fabry-Perot cavity

We construct our Fabry-Perot cavity by simply taking a finite section (here $10\mathrm{mm}$ long) of the two parallel chains of Josephson junctions and short circuiting it on the right end and connecting a dipole antenna on the left end. This dipole antenna is also used to couple radiation in and out of this Fabry-Perot cavity (see Fig. 4.2). This finite length Fabry-Perot now quantizes the phase oscillations

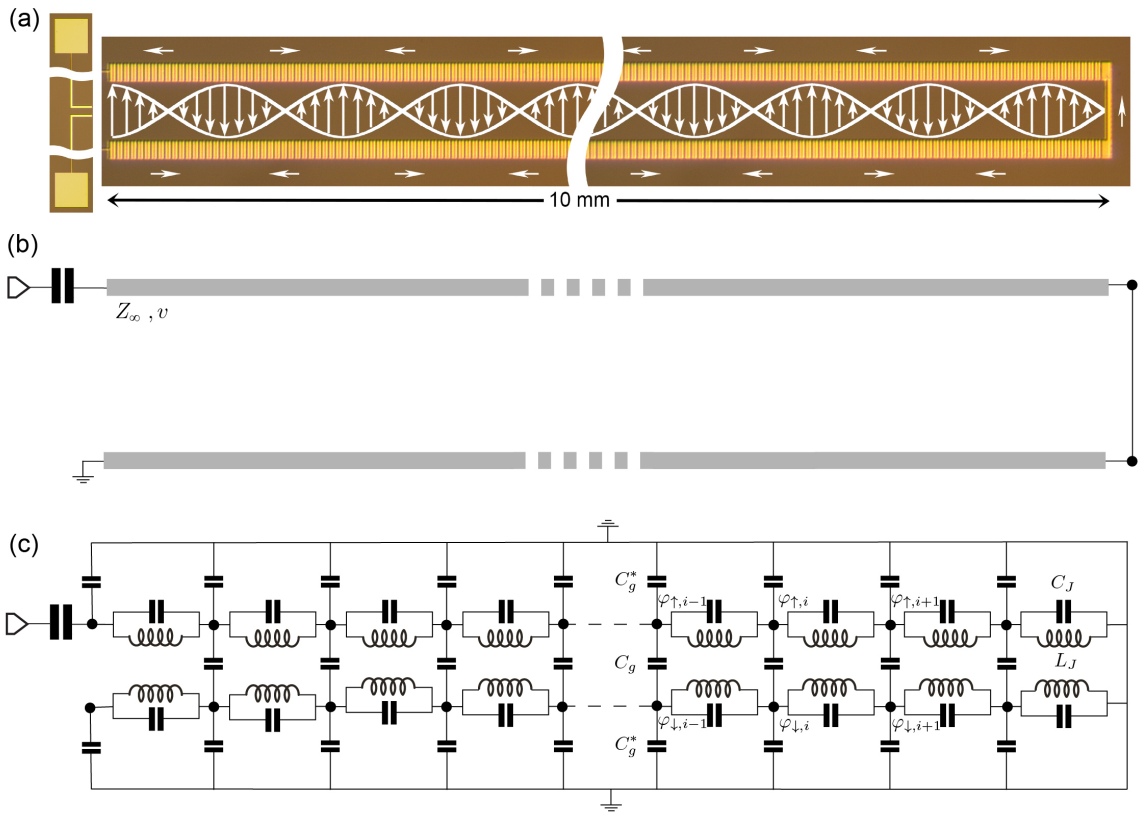

Figure 4.2: (a) Optical image of a multi-mode Fabry-Perot cavity made by terminating a high-impedance transmission line on the right by a short circuit and on the left by a weakly coupled antenna port. (b,c) Circuit schematic and lumped element circuit model of the same.

defined by Eq. 4.7 into standing wave modes and we can arrive at the dispersion relation of these collective modes of the phase field in the transmission line by imposing the boundary conditions corresponding to the two ends. To solve this boundary value problem for the wave equations we use the method of separation of variables discussed in section 2.2.2 and write the phase field in the transmission line as $\varphi_{-(+)}(x,t) = M_{-(+)}(x)N_{-(+)}(t)$. For the differential mode the boundary conditions define a zero voltage at the right end at $x = \ell$ and zero current at $x = 0$ and for the common mode the boundary condition corresponds to zero current at both ends. This directly leads us to the differential equation of the space and time parts of the phase oscillations:

$$\begin{aligned} \frac{d^2N_{-(+)}(t)}{dt^2} + \omega^2_{-(+)}N_{-(+)}(t) = 0, \\ \frac{d^2M_{-(+)}(x)}{dx^2} + k^2_{-(+)}M_{-(+)}(x) = 0, \end{aligned} \tag{4.8}$$

with boundary conditions:

$$\begin{aligned} \frac{dM_-(x=0)}{dx} = 0, \\ M_-(x=\ell) = 0, \\ \frac{dM_+(x=0)}{dx} = 0, \\ \frac{dM_+(x=\ell)}{dx} = 0, \end{aligned} \tag{4.9}$$

This leads to the quantization of the wave vector for the two sets of modes in the Fabry-Perot cavity:

$$\begin{aligned} k_{-,i} = \frac{\pi}{2\ell} + \frac{i\pi}{\ell}, \\ k_{+,i} = \frac{i\pi}{\ell}. \end{aligned} \tag{4.10}$$

This finally leads us to the dispersion relations for the differential and common standing wave modes in the Fabry-Perot cavity.

$$\omega_-(k_-) = \frac{a\sqrt{\frac{1}{2}E_J\tilde{E}_g}k_-}{\sqrt{1 + a^2k_-^2\frac{\tilde{E}_g}{2E_C}}}, \tag{4.11}$$

$$\omega_+(k_+) = \frac{a\sqrt{E_J E_g^*}k_+}{\sqrt{1 + a^2 k_+^2 \frac{E_g^*}{E_C}}}. \tag{4.12}$$

These dispersion relations can be further simplified into a two parameter form that reads:

$$\omega_-(k_-) = \frac{v_- k_-}{\sqrt{1 + (v_- k_-/\omega_p)^2}}, \tag{4.13}$$

$$\omega_+(k_+) = \frac{v_+ k_+}{\sqrt{1 + (v_+ k_+/\omega_p)^2}}. \tag{4.14}$$

These equations define two sets of modes with acoustic dispersion in the low frequency with a speed of propagation given by:

$$v_- = \frac{a}{\sqrt{2L_J C_g}}, \tag{4.15}$$

$$v_+ = \frac{a}{\sqrt{L_J C_g^*}}, \tag{4.16}$$

and a ultraviolet propagation cutoff given by $\omega_p = 1/\sqrt{L_J C_J}$, the self resonance frequency of the junctions forming the Fabry-Perot cavity. The wave impedance of the transmission line is given by $Z_\infty = \sqrt{2L_J/C_g}$. By changing the area of the Josephson junctions, the distance between the Josephson junction chains and length we can design Fabry-Perot cavities with a wide ranges of impedance, speed of light and FSR (free spectral range).

4.1.3 Interactions between standing wave modes

The interactions between the standing wave modes of our cavity are as a result of the non-linearity of the Josephson junctions forming the cavity. In the last section we ignored all the non-quadratic terms in the cosine potential of the junctions to arrive at the dispersion relation of the cavity. To derive the interactions between the modes of the cavity we add the 4^{th} order term in the cosine potential as a perturbation given by:

$$V = -\frac{2E_J}{a}\Big(\frac{1}{64}(\partial_x\varphi_+(x,t))^2(\partial_x\varphi_-(x,t))^2a^4 + \frac{1}{96}(\partial_x\varphi_-(x,t))^4a^4 + \frac{1}{96}(\partial_x\varphi_+(x,t))^4a^4\Big). \quad (4.17)$$

This perturbation introduces a negative self-Kerr non-linearity in all the standing wave modes of the cavity. In addition, the perturbation is also responsible for an all to all dispersive cross-Kerr interaction among the standing wave modes of the cavity. By quantizing the phase density and promoting the phase and the conjugate charge to quantum operators we arrive at the quantum Hamiltonian of the cavity:

$$\hat{H} = \sum_{i>0}\hbar\omega_i\hat{a}_i^\dagger\hat{a}_i + \sum_{i,j>0}\hbar\chi_{i,j}\hat{a}_i^\dagger\hat{a}_i\hat{a}_j^\dagger\hat{a}_j. \quad (4.18)$$

The second term in the Hamiltonian gives the interaction between modes. For $i = j$ it is the self Kerr interaction and for $i \neq j$ it is the cross Kerr interaction. The exact matrix elements can be calculated from the lumped element model of the cavity and the detailed procedure is given in ref [73].

4.2 Control Experiments

In this section we describe the first experiment that we perform to confirm the functioning of the Fabry-Perot cavity. Before we start the measurements we install the chip containing the Fabry-Perot cavity in a 3-D copper waveguide box with a single broadband microwave input/output port see (Fig 3.2 (a). The details of the 3-D waveguide design are presented in section 3.2.1. The simplest experiment we perform on the device is to measure the reflection coefficient of continuous tone microwaves generated by a Rhode and Swartz VNA. To launch microwaves we use a coaxial-to-waveguide launcher with good matching in the range $5 - 10$ GHz (see section 3.2 (b)). A typical trace reveals an ordered set of discrete resonances, which we associate with the standing wave modes of the Fabry-Perot (see Fig. 4.3). One important point to note here is that the geometry of the coaxial cable to waveguide launcher in our experiment is chosen such that the microwave signals can only couple to the differential modes in our device and not the common modes. For this reason, moving forward we will ignore the effect of the common modes in the system and

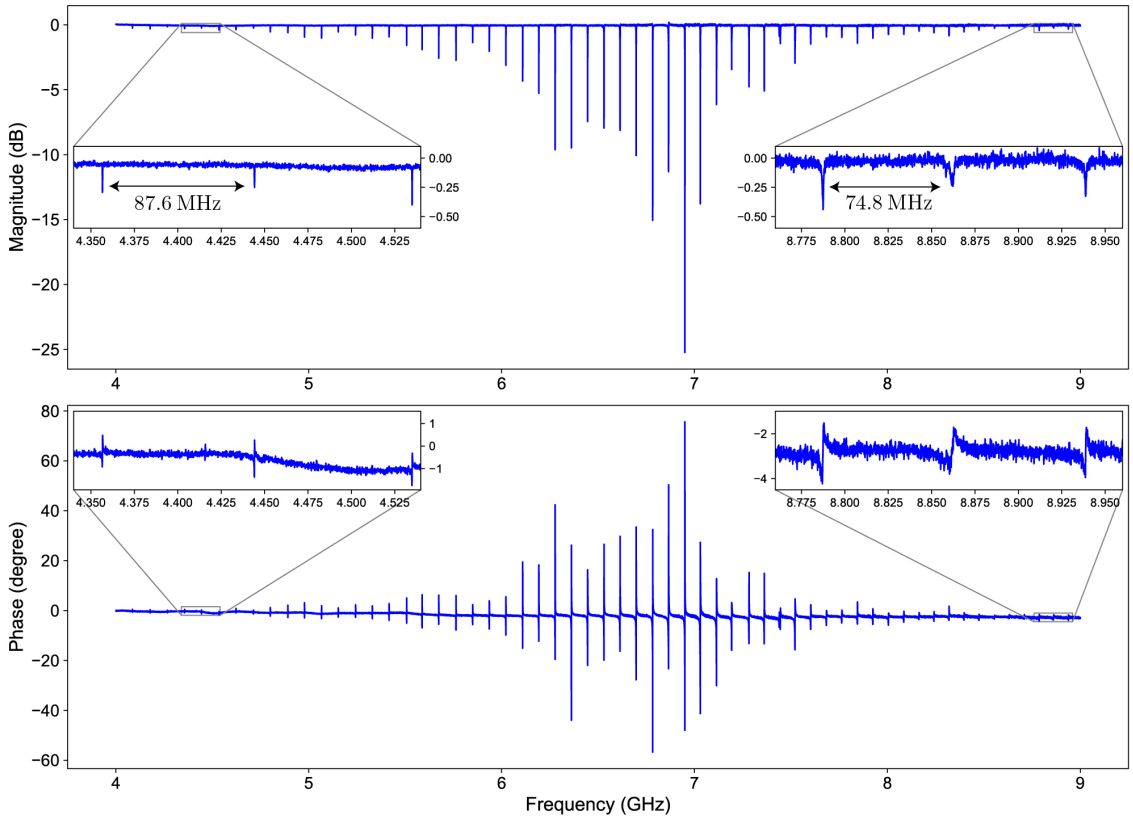

Figure 4.3: Reflection magnitude and phase response of a typical multi-mode Fabry-Perot made using a array of Josephson junctions. The insets shows the change in the mode spacing as the mode frequency increases because of the ultra-violet cutoff at the self resonance frequency of the Josephson junctions.

concentrate only on the differential modes. By measuring the spectral distance between adjacent resonances and knowing the length ℓ of the Fabry-Perot cavity we estimate the speed of light in the cavity $v = (\omega_{i+1} - \omega_i)/(2\pi\ell) \approx 1.75 \times 10^6\,\mathrm{m/s} \approx c/172$. This measurement confirms that indeed our transmission line acts like a 1-D Fabry-Perot cavity where the light is slowed down by more than a factor of 100. Another important thing to note in this measurement is the vanishing of the magnitude and phase response of the cavity resonances as the frequency goes below $4\,\mathrm{GHz}$ and above $9\,\mathrm{GHz}$. This is primarily due to the cutoff of the 3-D waveguide used to house the chip which is at $\sim 7\,\mathrm{GHz}$.

4.3 Characterization Experiments

In this section we describe more extensive and detailed experiments that are performed to accurately characterize our multi-mode Fabry-Perot cavity.

4.3.1 Intrinsic lifetime of modes

In addition to revealing the positions of the standing wave modes in our Fabry-Perot cavity we use the frequency dependent reflection coefficient measurement in the vicinity of each resonance to characterize the lifetime of the modes. We fit the data to the well known expression:

$$S_{11}(\omega) = \prod_{i=1}^{N} \frac{2\mathrm{i}(\omega - \omega_i)/\omega_i - (Q_i^{\mathrm{ext}})^{-1} + (Q_i^{\mathrm{int}})^{-1}}{2\mathrm{i}(\omega - \omega_i)/\omega_i + (Q_i^{\mathrm{ext}})^{-1} + (Q_i^{\mathrm{int}})^{-1}}\,, \tag{4.19}$$

where ω_i is the resonance frequency of the i^{th} Fabry-Perot standing wave mode, $Q_i^{\mathrm{int(ext)}}$ is the internal (external) quality factor of the resonance. Q^{int} parameterizes the loss of energy in the standing wave mode inside the transmission line device. Whereas, Q^{ext} can be viewed as a measure of opacity of the mirror at the antenna end of the chain. We found that, at frequencies below $7\,\mathrm{GHz}$, the opacity grows on reducing the frequency, which is consistent with the propagation cutoff of our copper waveguide. The opacity also has a tendency to increase as the frequency grows above $10\,\mathrm{GHz}$, which may be related to a partial Anderson localization of microwaves in the chain and their decoupling from the antenna end [74]. As a result, one-tone spectroscopy becomes inefficient far outside the $5 - 10\,\mathrm{GHz}$ pass band of our coaxial-to-waveguide launching system. For this reason, the

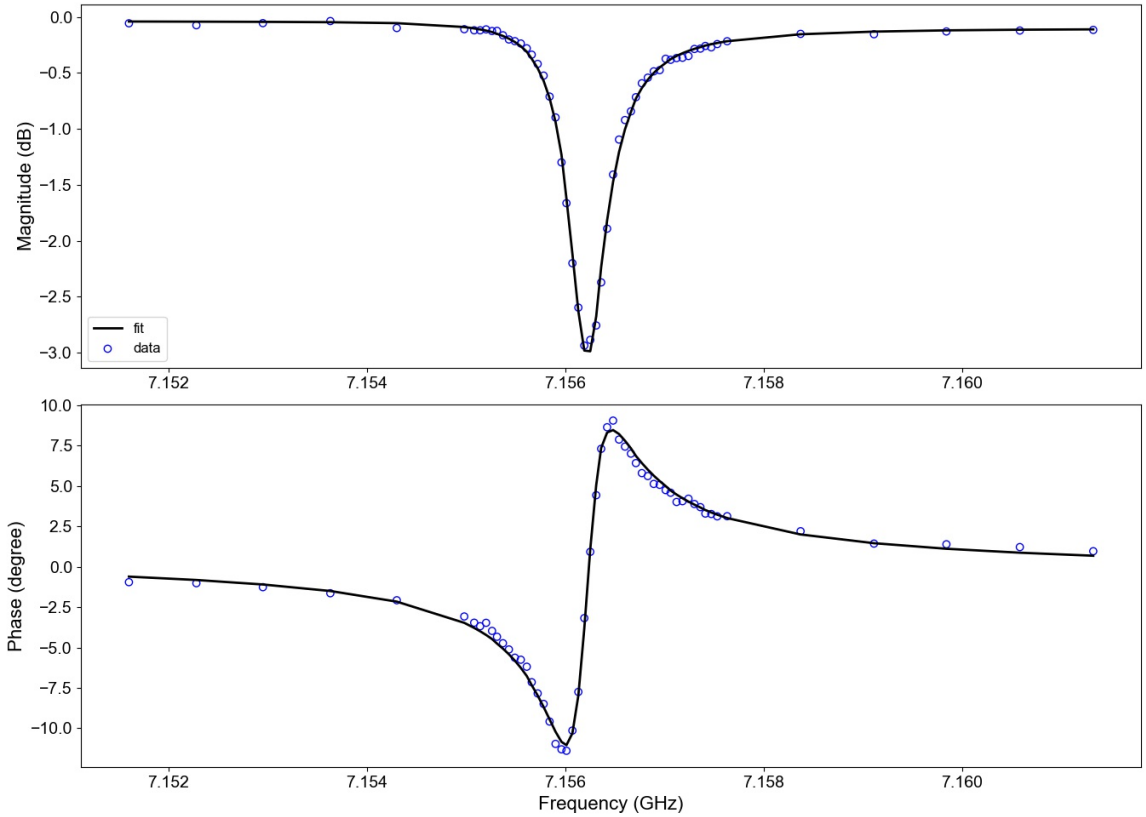

Figure 4.4: One tone spectroscopy overlayed with the fit to Eq. 4.19 used to extract the internal and external quality factor of the standing wave modes of the Fabry-Perot cavity.

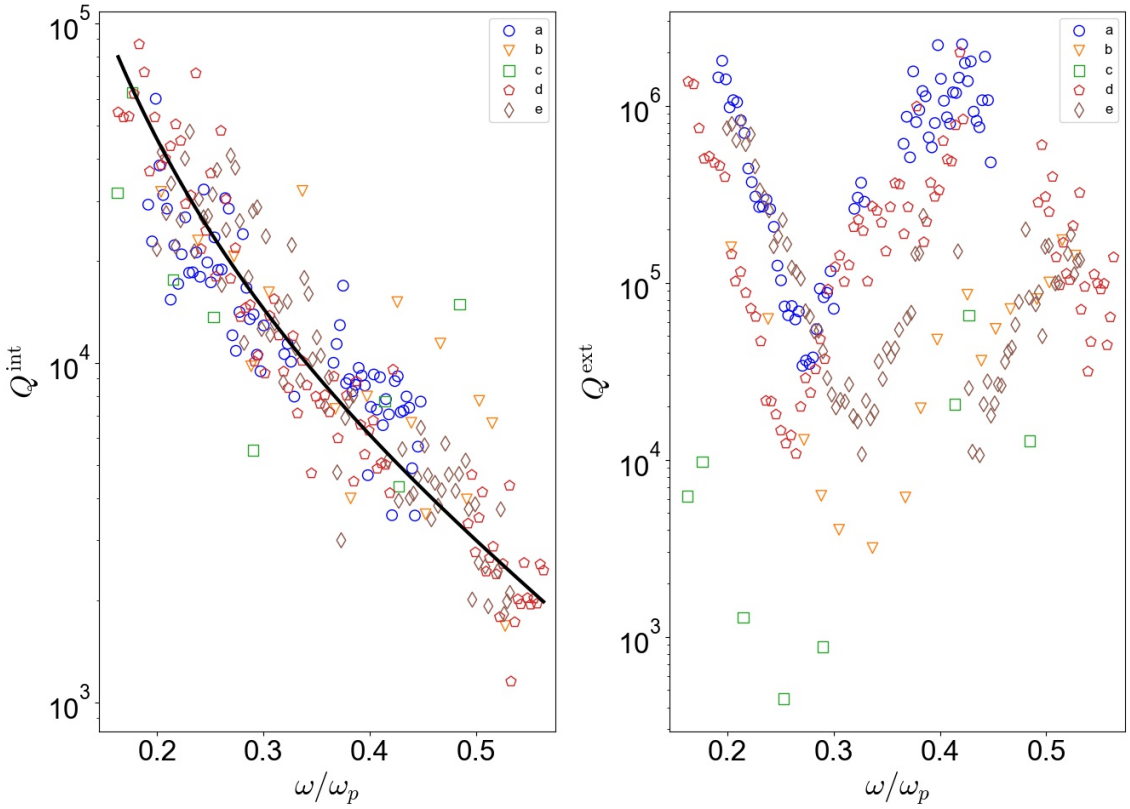

Figure 4.5: Inernal (left panel) and external (right panel) quality factor of the standing wave modes of all the Fabry-Perot cavities plotted against the dimensionless parameter ω/ω_p

frequency range in Fig. 4.3 is limited. Finally, we note that our reflection data fit exceptionally well to the above expression for $S_{11}(\omega)$, as shown in the Fig 4.4, which allows very accurate extraction of both ω_i and $Q_i^{\text{int(ext)}}$.

We are also able to explain the intrinsic loss of energy in our standing wave modes. The limiting mechanism of loss in our device is due to the absorption of photons in the dielectric of the Josephson junctions. We model this loss by adding a small complex part to the junction capacitance $C_J \rightarrow C_J(1 + \mathrm{i}\tan\delta)$. Using this we are able to arrive at the expression for the internal quality factor of the standing wave modes:

$$Q^{\text{int}}(\omega) = \frac{2}{\tan\delta}\left(\frac{\omega_p}{\omega}\right)\left(1 - \left(\frac{\omega_p}{\omega}\right)^2\right), \tag{4.20}$$

here $\tan\delta$ is the dielectric loss tangent. The internal quality factors data acquired across multiple devices fit very well to this model with a dielectric loss tangent of $\tan\delta = 10^{-3}$ (see Fig. 4.5). This value is consistent with other experiments done using Al/Alox Josepshon junctions [75]. This knowledge of the intrinsic loss mechanism in isolated Fabry-Perot modes will be crucial in latter chapters when we introduce impurity in the Fabry-Perot cavity.

4.3.2 Two tone spectroscopy

To further characterize the cavity and to extract the cavity mode frequencies beyond $7 - 12$ GHz range, we use a two tone spectroscopy technique where we exploit the weak cross-Kerr interaction between the standing wave modes of the cavity. First, the readout mode is selected in the pass band. Reflection amplitude and phase at a properly chosen frequency near the resonance are measured as a function of the frequency of the second tone, which is scanned to look for other modes. The cross-Kerr effect results in the shifting of the frequency of the readout mode due to the photon occupation of every other mode in the system (see Fig. 4.6). Using this technique it is possible reconstruct the full dispersion relation of the standing wave modes in the cavity and index the modes (see Fig. 4.7). This dispersion is in excellent agreement with the simple two parameter expression derived in section 4.1.1. We fit the extracted mode frequencies to obtain the speed of light in the Fabry-Perot cavity and the ultra-violet cutoff which corresponds to the self resonance frequency of the junctions forming the transmission line. Fig. 4.7 (a) clearly shows the $i = 1$ mode of the cavity

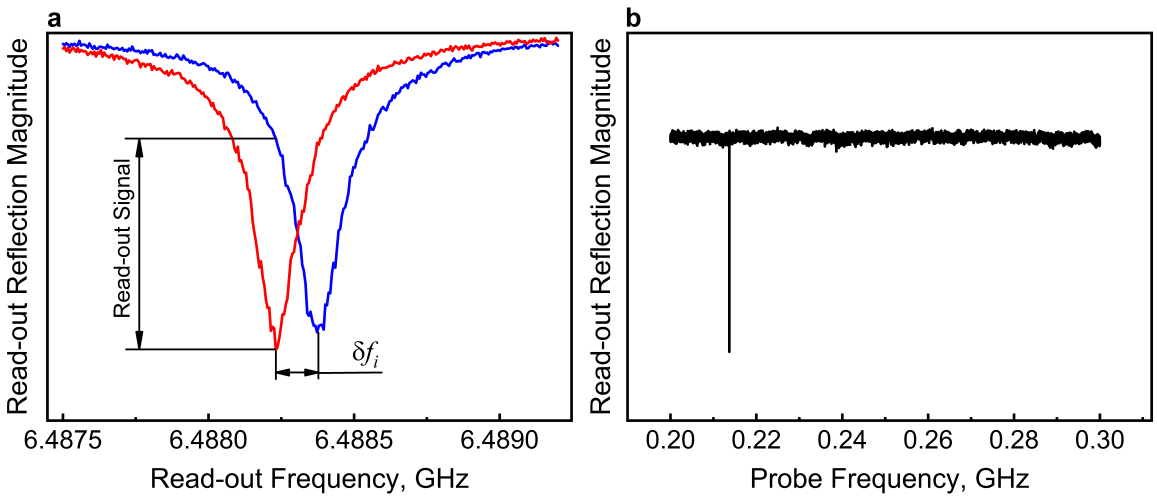

Figure 4.6: (a) The read-out mode while the probe tone is in (red) and out off resonance (blue) with the standing wave mode at 215 MHz. (b) The read-out tone reflection magnitude measured at the left shoulder of read-out mode line as a function of the probe tone frequency.

at 40 MHz, at approximately half the mode spacing, which correctly reflects the open and short circuit boundary conditions of the cavity mathematically expressed in Eq. 4.1.2. This observation confirms that wave propagation occurs along the entire length of the system and the spectrum is gapless. Fluctuations of the mode spacing as a function of the mode index are found to be within a few percent, independently of the wavenumber (Fig. 4.7 (c)), thus showing minimal disorder of junction parameters along the entire length of the system.

4.3.3 Extracting Impedance

By fitting the measured dispersion relation of standing wave modes in the cavity we get an accurate estimate of the speed of light and the plasma frequency cutoff. However, our Fabry-Perot cavity is characterized completely by 3 independent circuit parameters C_J, L_J, and C_g. From the measurement of the speed of light and plasma cutoff we have access to $1/\sqrt{L_J C_J}$ and $1/\sqrt{L_J C_g}$. In order to estimate the wave impedance $Z_\infty = \sqrt{L_J/C_g}$ we use two separate methods. The first one exploits the fact that the Al oxide growth is typically self-terminating. It implies that the Josephson junction capacitance is fully defined by the junction area. We use SEM to measure the junction areas along the chain. The C_J is found then as an average junction area multiplied by an empirical constant

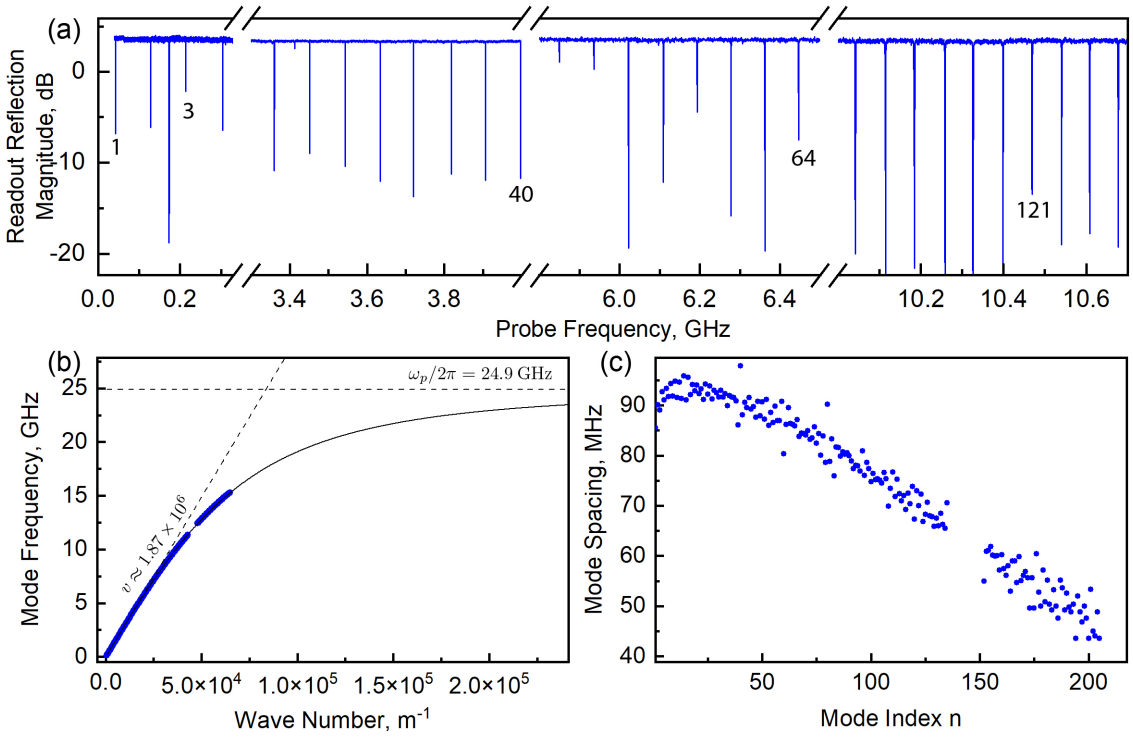

Figure 4.7: (a) The magnitude of reflection coefficient as a function of the probe frequency. Discrete standing wave resonances are indexed one by one starting from the very first mode at about $40\,\mathrm{MHz}$. The third resonance is a spurious mode and is discarded. (b) The reconstructed dispersion relation (blue markers) and theoretical fit to Eq. 4.13 (solid line). (c) The mode spacing as a function of the mode index. The sharp periodic outliers originate from the stitching error of the e-beam lithographer, otherwise invisible in device images.

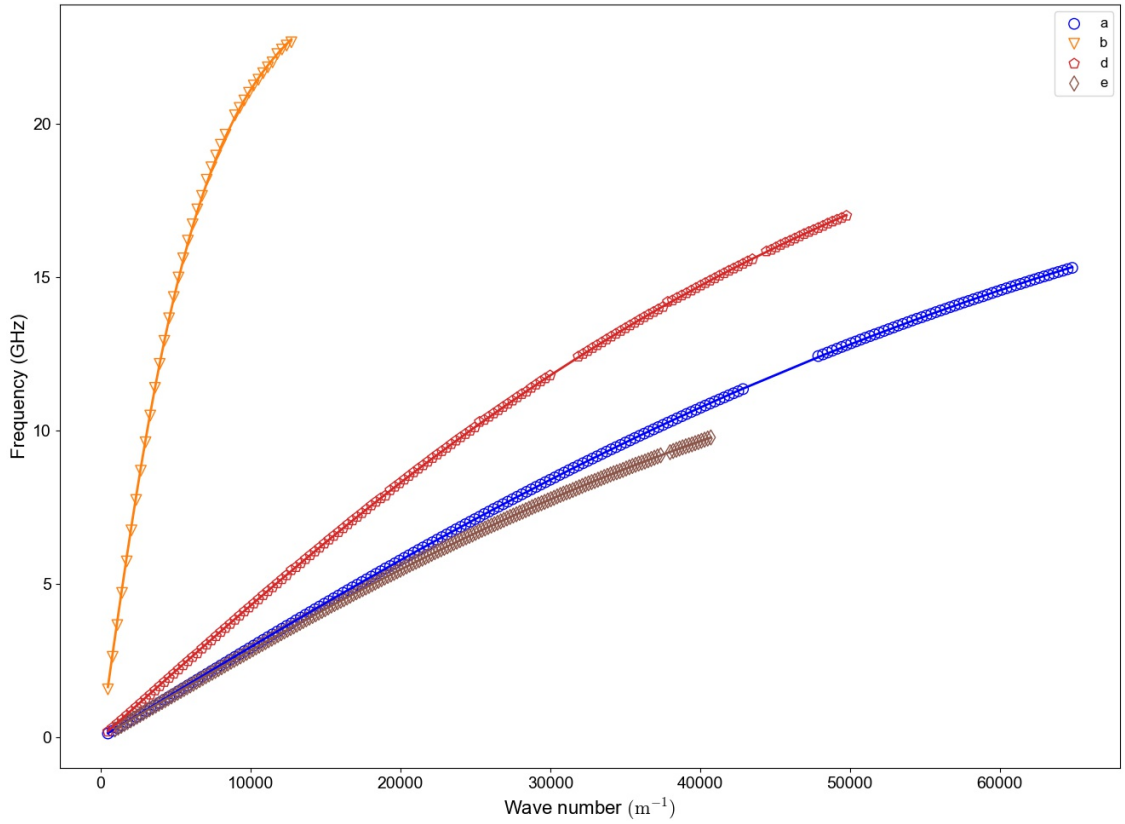

Figure 4.8: Reconstructed dispersion relation of all the multi-mode Fabry-Perot cavities. Parameters are listen in Table. 4.1

$45 f\mathrm{F}/\mathrm{m}^2$. The second method of finding the wave impedance takes the known geometrical dimensions of the chains and uses the well-known result for the capacitance of the coplanar stripes in order to calculate C_g. These methods give the impedance values which are different from each other by no more than 20 % (Table. 4.1). This number can be considered as our accuracy for an absolute impedance measurement. We take the average of these two values as our estimate for Z_∞. Their difference divided by $\sqrt{2}$ gives the impedance uncertainty.

4.4 Summary of measurements and conclusion

In summary, the reflection spectroscopy experiments on our devices confirm that we are able to engineer on chip multi-mode Fabry-Perot cavities. Exploiting the kinetic inductance of the Josephson junctions we are able to achieve two orders of magnitude reduction in the speed of light and an almost two orders of magnitude increase in the wave impedance of the cavity. This allows us to have a compact massively multi-mode cavity which can host ~ 100 standing wave modes in the frequency range of $0 - 10$ GHz. Furthermore, by measuring the quality factor of the modes we confirm that the photons in the standing wave modes are well isolated and have line widths $\gamma/\Delta \leq 100$. This is an important ingredient in exploring many-body effects in the system, since we want the intrinsic dissipation of the modes to be much smaller than the strength of the many-body effects.

4.5 Summary of device parameters

Device	$v/10^6(\mathrm{m/s})$	$\omega_p/2\pi(\mathrm{GHz})$	$Z_\infty(\mathrm{k}\Omega)$	E_J/E_C	Length (mm)
a	1.87 ± 0.05	24.9 ± 0.02	12.1 ± 0.6	87 ± 9	10
b	22.6 ± 0.06	26.7 ± 0.05	0.7 ± 0.05	729 ± 23	10
d	8.2 ± 0.01	21.5 ± 0.03	2.2 ± 0.1	224 ± 18	10
e	2.11 ± 0.03	20.9 ± 0.02	7.3 ± 0.4	448 ± 52	10

Table 4.1: Device parameters obtained from fitting the measured dispersion relation to theory.

Chapter 5

Fluxonium impurity coupled to multi-mode cavity

In this chapter we describe the experimental implementation and characterization of multi-mode cavity QED system where we couple a fluxonium artificial atom to the multi-mode Fabry-Perot cavity introduced in the last chapter. We characterize the effect of the fluxonium impurity on the Fabry-Perot cavity by measuring the frequency of the standing wave modes of the cavity as a function of the external flux threading the fluxonium atom. We derive an effective three wave mixing Hamiltonian which can split a single excitation in our cavity into many low frequency excitations but fails due to many-body localization. Through spectroscopy measurements we show signatures of the many-body localization of photons which manifests itself as the splitting of standing wave resonance into a fine structure of multi-particle resonances.

5.1 Design of the device

The system we study in this chapter consists of a two-wire transmission line of length $\ell = 6\ \mathrm{mm}$, characterized by its wave impedance Z_∞ and speed of light v, as shown in Fig. 5.1 (a). This transmission line is terminated on one end by a superconducting loop made up of an array of Josephson junctions including one weak junction that forms the fluxonium artificial atom. The fluxonium is

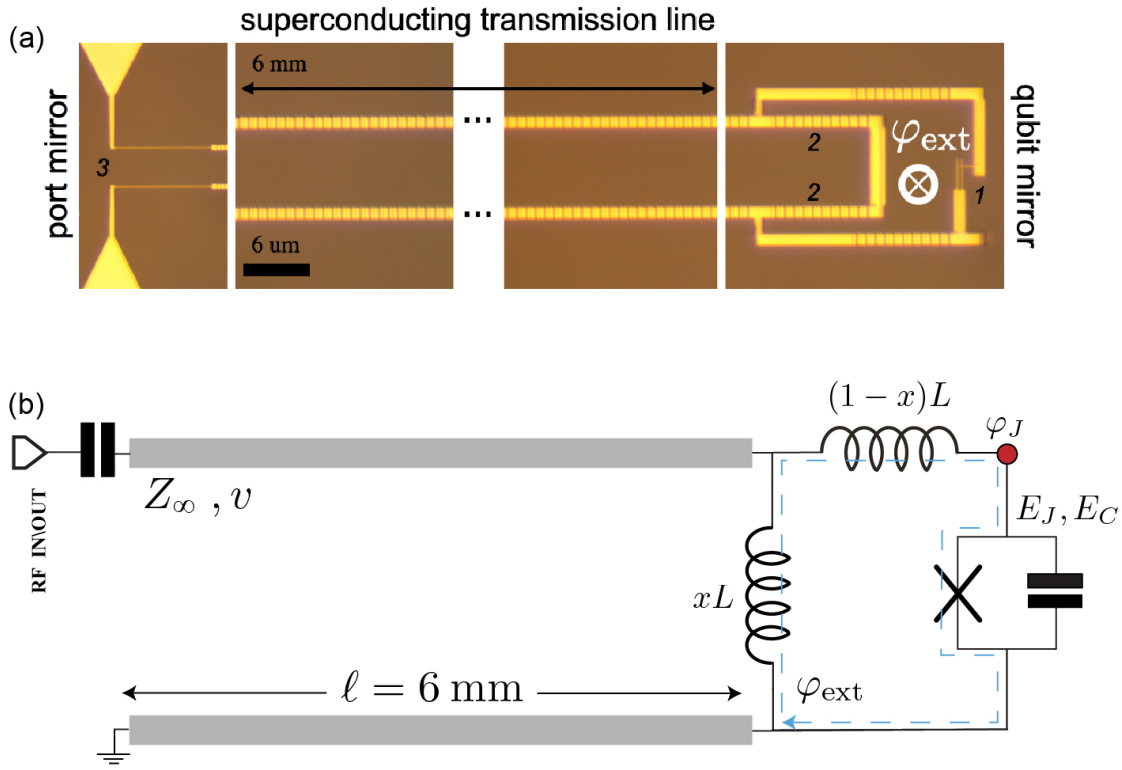

Figure 5.1: Optical micrograph (a) and circuit schematic (b) of the system showing a two-wire transmission line terminated by a superconducting fluxonium atom. The transmission line is characterized by its wave impedance Z_∞, speed of light v, and length ℓ. The fluxonium is defined by the Josephson energy E_J, the charging energy E_C of the small junction and the loop inductance L. A fraction x (shown as region 2 on optical image) of the fluxonium loop inductance is shared with the transmission line, coupling galvanically the atom to the transmission line's standing wave modes. The atom transition frequency can be tuned by changing the external flux bias $(\hbar/2e)\varphi_{\text{ext}}$ threading the superconducting loop.

galvanically connected to the transmission line such that the fluxonium loop junction array shares a fraction x ($0 < x \leq 1$) of the junctions with the transmission line. These shared junctions are responsible for the coupling of the standing wave modes of the transmission line to the fluxonium, thus creating an interacting multi-mode circuit QED system. For given fluxonium and transmission line parameters, the coupling depends on the geometric factor x. The energy levels of the fluxonium can be controlled by varying an external magnetic flux $(\hbar/2e)\varphi_{\text{ext}}$ pierced through the fluxonium loop. In this chapter we primarily discuss the measurement results from a device which shares $x = 0.5$ of its inductance with the transmission line. In addition to this a number of samples with varying geometric factor x were characterized and we summarize the results from those measurements in the last section.

5.2 Microscopic Hamiltonian

The system described in this work can be modeled as a fluxonium coupled inductively to a high-impedance transmission line cavity. With careful selection of the gauge we can arrive at the exact microscopic Hamiltonian of our system (see section 2.4.2). The Hamiltonian consists of three terms, the first two terms define the bare fluxonium qubit and the bare non-interacting bosonic modes of the transmission line cavity. The third term defines the coupling between the two

$$\hat{H} = \hat{H}_{\text{qubit}} + \hat{H}_{\text{modes}} + \hat{H}_{\text{int}}. \tag{5.1}$$

Explicitly the three terms are defined as:

$$\hat{H}_{\text{qubit}}/h = 4E_C\hat{n}_J^2 + \frac{1}{2}E_L\hat{\varphi}_J^2 - E_J\cos(\hat{\varphi}_J - \varphi_{\text{ext}})\,, \tag{5.2}$$

$$\hat{H}_{\text{modes}}/h = \sum_{i=1}^{\infty} f_i^{(m)}\hat{b}_i^\dagger\hat{b}_i\,, \tag{5.3}$$

$$\hat{H}_{\text{int}}/h = -\hat{\varphi}_J\sum_{i=1}^{\infty} g_i^{(m,f)}(\hat{b}_i + \hat{b}_i^\dagger) + \mathrm{i}\hat{n}_J\sum_{i=1}^{\infty} g_i^{(m,c)}(\hat{b}_i^\dagger - \hat{b}_i)\,, \tag{5.4}$$

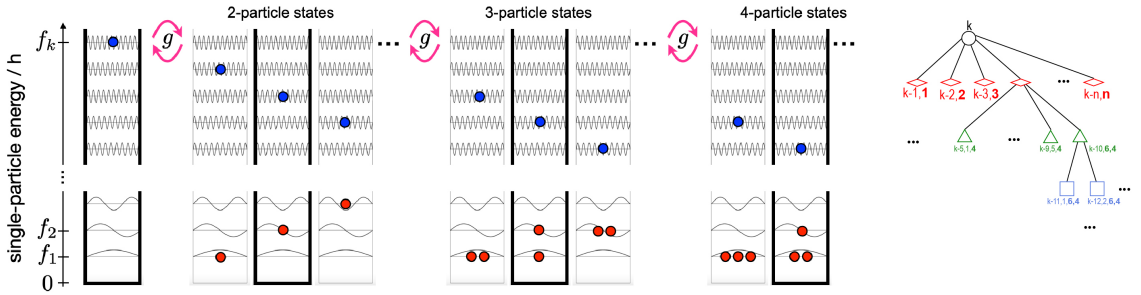

Figure 5.2: (a) Sketch depicting the frequency and wavefunctions of the cavity modes with free spectral range Δ. The columns show a subset of multi-particle states nearly resonant and coupled with the single-particle state occupying the mode k. (b) Schematic representation of connectivity in the many-body Fock space with a tree diagram whose nodes depict the many-body states and the edges connect the states that have a direct matrix element mediated by the three wave mixing term $\hat{V}$.

here the Hamiltonian parameters are related to an exact circuit model. The corresponding circuit model and detailed procedure to arrive at the specific Hamiltonian parameters can be found in section 2.4.2.

5.3 Effective Hamiltonian

In this section, we derive an effective Hamiltonian treatment that can be applied to our system when the coupling between the standing wave modes of the cavity and the fluxonium is such that $\Gamma \ll f_{\mathrm{eg}}$, where f_{eg} is the frequency of the fluxonium transition from the ground state to the first excited state and Γ is its radiative width into a semi-infinite transmission line (where the standing-wave modes form a continuum). In doing so, we only consider the transition from the ground state $|\mathrm{g}\rangle$ to the first excited state $|\mathrm{e}\rangle$. Within such a two-level approximation, the fluxonium atom Hamiltonian can be approximated as:

$$H_{\mathrm{qubit}}/h = f_{\mathrm{eg}}(\varphi_{\mathrm{ext}})|\mathrm{e}\rangle\langle\mathrm{e}|. \tag{5.5}$$

The flux-dependent transition frequency f_{eg} in Eq. (5.5) is calculated by a numerical diagonalization of the full fluxonium Hamiltonian given in Eq. (5.2). We also consider the Hamiltonian of our system in the mixed gauge, where we recall that the first i_0 modes of the cavity are coupled to

the atom predominantly via the flux variable and the higher $i > i_0$ cavity modes are coupled predominantly via the charge variable. This is convenient not only for the behavior of the qubit-cavity coupling constants at low and high frequencies, but also because for a strongly anharmonic qubit the two-level approximation is excellent in such a gauge, as verified with brute force numerics in the Appendix A.

We start by dividing the Fabry-Perot standing wave modes into two sets. The first set includes modes with frequencies much smaller than the fluxonium qubit transition frequency at $\varphi_{\rm ext} = \pi$ (mode index i such that $1 \leq i \leq i_0$). The second set of modes includes those that quasi-resonantly hybridize with the qubit transition. We will denote k the index of such modes where $i_0 < k \leq N$. Note here that N is the high frequency cutoff chosen such that $f_N \gg f_{\rm eg}$ which ensures that modes above mode number N also do not hybridize with the qubit transition. In the first step, we ignore for the time being the coupling of the fluxonium to the low-frequency bosonic modes of the transmission line and diagonalize the following Hamiltonian

$$\hat{H}_0 = \hbar\omega_{\rm eg}|{\rm e}\rangle\langle{\rm e}| + \sum_{i=1}^{N} \hbar\omega_i^{(m)} \hat{b}_i^\dagger \hat{b}_i - \hat{\varphi}_J \sum_{i>i_0} hg_i^{(m,f)} (\hat{b}_i + \hat{b}_i^\dagger) + {\rm i}\hat{n}_J \sum_{i>i_0} hg_i^{(m,c)} (\hat{b}_i - \hat{b}_i^\dagger)\,, \tag{5.6}$$

in the single-excitation subspace spanned by the basis states:

$$\mathcal{B}_0 = \left\{ |{\rm e}\rangle|0\rangle, |{\rm g}\rangle\hat{b}_k^\dagger|0\rangle \right\}_{1\leq k\leq N}\,. \tag{5.7}$$

Note that the single-excitation eigenstates of the Hamiltonian (5.6) consist of bare transmission line modes for $k \leq i_0$ with excitation frequency $\omega_k^{(m)}/2\pi$. For $k > i_0$ they have the form:

$$\hat{a}_k^\dagger|G\rangle = W_{k,0}|{\rm e}\rangle|0\rangle + \sum_{k'} W_{k,k'}|{\rm g}\rangle\hat{b}_{k'}^\dagger|0\rangle\,, \tag{5.8}$$

where $f_k = \omega_k/2\pi$ is the corresponding single-polariton excitation frequency. The term "polariton" state in used here in analogy to similar states appearing in semiconductor systems. The Hamiltonian in Eq. (5.6) can now be rewritten as

$$\hat{H}_0 = \sum_{i>0} \hbar\omega_i \hat{a}_i^\dagger \hat{a}_i \,. \tag{5.9}$$

As a second step of our procedure, we now include the effect of the coupling of low-frequency modes to the fluxonium in Eq. (5.9). The coupling term is given by

$$\hat{V} = -\hat{\varphi}_J \sum_{i=1}^{i_0} h g_i^{(m,f)} (\hat{b}_i + \hat{b}_i^\dagger) + \mathrm{i}\hat{n}_J \sum_{i=1}^{i_0} h g_i^{(m,c)} (\hat{b}_i - \hat{b}_i^\dagger) \,. \tag{5.10}$$

As it can be directly inspected, this term gives rise to an effective coupling between the bare transmission line modes and the polaritonic modes via a three-wave mixing process. Indeed, this elementary process down converts one particle states $\hat{a}_k^\dagger|0\rangle$ into two-particle states $\hat{a}_{k'}^\dagger \hat{a}_i^\dagger|0\rangle$, with excitations in another polaritonic mode k' and one excitation in a low-frequency photon mode i. The corresponding coupling is quantified by the following matrix element:

$$\langle G|\hat{a}_k \hat{V} \hat{a}_{k'}^\dagger \hat{a}_i^\dagger|G\rangle = h g_i^{(m,f)} W_{k,0}^* W_{k',0} (\langle \mathrm{e}|\hat{\varphi}_J|\mathrm{e}\rangle - \langle \mathrm{g}|\hat{\varphi}_J|\mathrm{g}\rangle) \,. \tag{5.11}$$

Likewise, each of these two-particle states can couple to a subset of three-particle states, which retain the low-frequency photon in mode i from the previous generation, i.e. the low-frequency photons are stable, and so forth. This finally leads to the effective Hamiltonian of our multi-mode cQED system:

$$\hat{H}_{\mathrm{eff}} = \sum_{k>0} \hbar\omega_k \hat{a}_k^\dagger \hat{a}_k + hg \sum_{k,k'>i_0}^{i\leq i_0} \sqrt{i} A_{k,k'} \hat{a}_k \hat{a}_{k'}^\dagger \hat{a}_i^\dagger + h.c. \,, \tag{5.12}$$

where

$$A_{k,k'} = W_{k,0}^* W_{k',0} \,, \tag{5.13}$$

$$g = g_1^{(m,f)} (\langle \mathrm{e}|\hat{\varphi}_J|\mathrm{e}\rangle - \langle \mathrm{g}|\hat{\varphi}_J|\mathrm{g}\rangle) \,. \tag{5.14}$$

Note that the matrix element $A_{k,k'}$ is proportional to the qubit components in the polaritonic modes participating in the three-wave-mixing process. via the factor $W_{k,0}^* W_{k',0}$. Moreover, the three-wave-mixing interaction strength g is finite only when there is a breaking of the flux symmetry of the

Josephson atom potential energy (necessary to have $\langle \mathrm{e}|\hat{\varphi}_J|\mathrm{e}\rangle - \langle \mathrm{g}|\hat{\varphi}_J|\mathrm{g}\rangle \neq 0$), which is achieved away from $\varphi_{\mathrm{ext}} = n\pi$. In addition, the three-wave-mixing strength g is proportional to the coupling of the fluxonium to the low frequency mode i. In the flux gauge, it is given by $g_i^{(m,f)} = g_1^{(m,f)}\sqrt{i}$, as it can be seen from Eq. (2.97).

The effective Hamiltonian can now be used to construct the full spectrum of our system by an iterative procedure that consists of enlarging the Hilbert space to include multi-particle states. Two-excitation states can be accounted for by considering the subspace spanned by the following basis of states:

$$\mathcal{B}_1 = \mathcal{B}_0 \bigcup \left\{ \hat{a}_k^\dagger \hat{a}_i^\dagger |0\rangle \right\}_{1\leq i\leq i_0}^{i_0<k\leq N} . \tag{5.15}$$

In this expanded Hilbert space, the single-polariton states are no longer eigenstates of the Hamiltonian. This is due to the fact that the single-polariton states now can hybridize with two-photon states due to the photon-photon interactions mediated by the fluxonium. Given the large number of frequency degeneracies between single-polariton states and two-photon states, determined by the relation $\omega_k = \omega_{k'} + \omega_i^{(m)}$, the diagonalization of the effective Hamiltonian produces a myriad of energy anticrossings in the spectrum. If we want to include the effect of three-photon states, we need to enlarge the basis of the Hilbert space by considering the states:

$$\mathcal{B}_2 = \mathcal{B}_0 \bigcup \mathcal{B}_1 \bigcup \left\{ \hat{a}_k^\dagger \hat{a}_{k'}^\dagger \hat{a}_i^\dagger |0\rangle \right\}_{1\leq i\leq i_0}^{i_0<k,k'\leq N} . \tag{5.16}$$

This process of expanding the Hilbert space can be iterated to include n-photon states, where we have one excitation in the polaritonic mode and $n-1$ excitations in low-frequency photon modes.

5.4 Control experiments

In this section we describe two simple control experiments that are preformed to ensure that the two main components namely the transmission line and the fluxonium atom are functioning as intended.

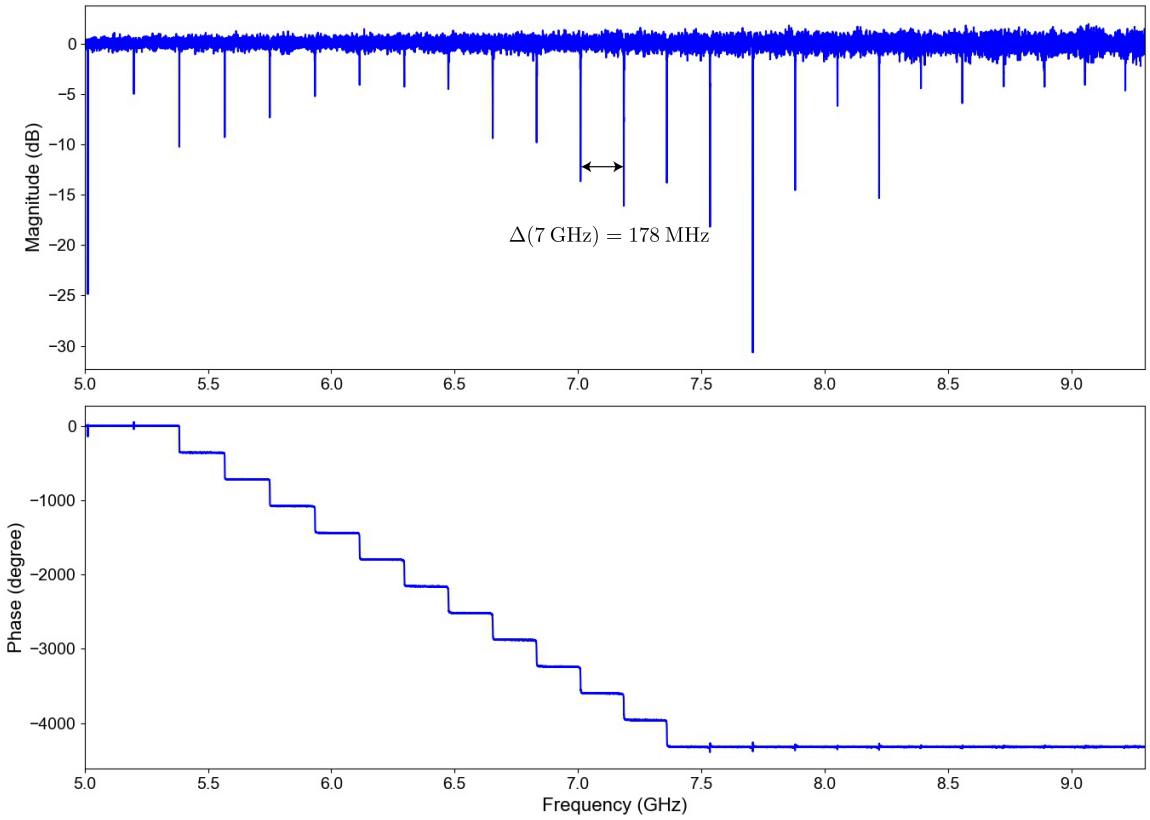

Figure 5.3: Reflection magnitude and phase as a function of CW microwave probe tone when there is zero external flux threading the fluxonium loop.

5.4.1 Single tone

Here we repeat the most basic experiment that we performed on a Fabry-Perot cavity described in the last chapter. We measure the reflection coefficient at the single port of the 3-D copper waveguide as a function of the CW microwave tone when there is no magnetic flux threading the fluxonium loop. The response reveals an almost equally spaced forest of resonances indistinguishable from the response of the bare Fabry-Perot cavity shown in Fig 4.3 in chapter 4. By measuring the distance between the consecutive resonances ($\Delta(7\,\mathrm{GHz}) = 178\,\mathrm{MHz}$) and knowing the length of the transmission line, we can estimate the speed of light as $v \approx 2 \times 10^6\,\mathrm{m/s}$. The measurement of speed of light and mode spacing confirms that the junctions of the transmission line are superconducting and there is no break in the line and the microwave propagation happens along the full length of the device.

5.4.2 Single tone Vs flux

In this next experiment we repeat the same reflection coefficient measurement but this time scanning a smaller frequency range of $200\,\mathrm{MHz}$ around $7\,\mathrm{GHz}$ for different values of the DC current flowing through the superconducting coil. The result of this measurement is displayed in Fig. 5.4 which shows that the standing wave resonance of the cavity is modulated periodically as a function of DC current flowing through the coil and the flux threading the fluxonium loop. This measurement shows that the fluxonium loop is connected and is superconducting. In addition, we observe no vacuum Rabi splittings in the spectroscopy data as the fluxonium frequency is tuned through $7\,\mathrm{GHz}$. Instead we observe that multiple modes of the cavity shift simultaneously which proves we have achieved the superstrong coupling regime of cavity QED.

5.5 Characterization experiments

Together these two experiments show that the transmission line and fluxonium are working as expected and now we can proceed to characterize the device in more detail.

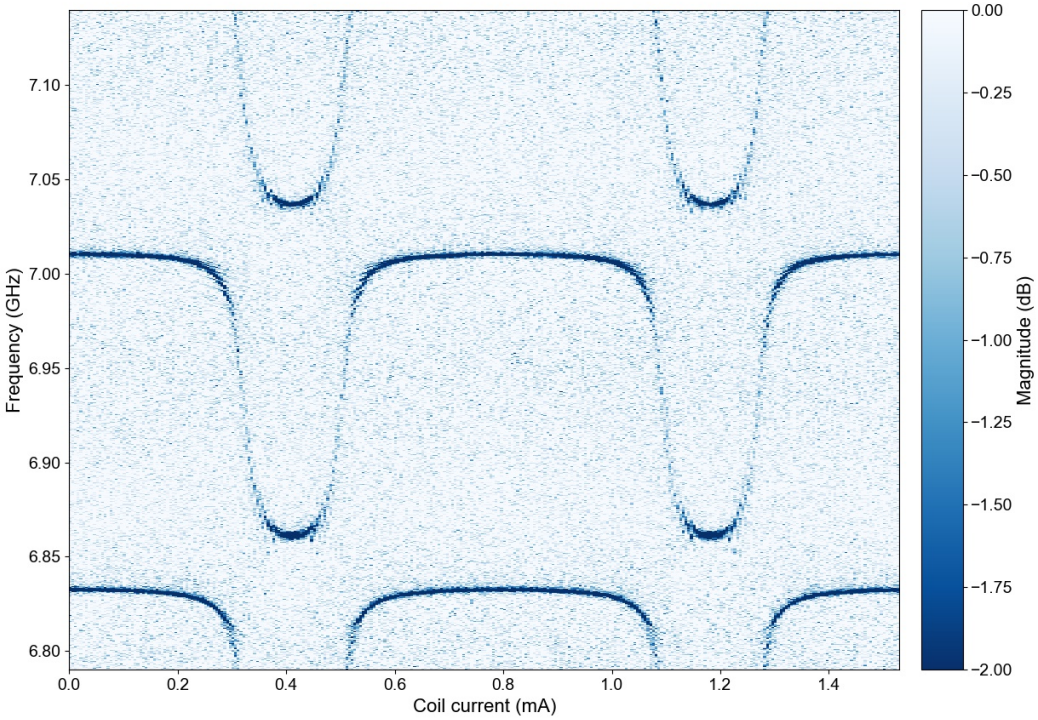

Figure 5.4: Colorplot of reflection magnitude as a function of externally applied magnetic flux threading the fluxonium loop. The signal is clearly flux periodic which shows that the fluxonium loop is closed and superconducting. This periodicity of the reflection signal with coil current is used to calibrate the magnetic flux threading the fluxonium loop.

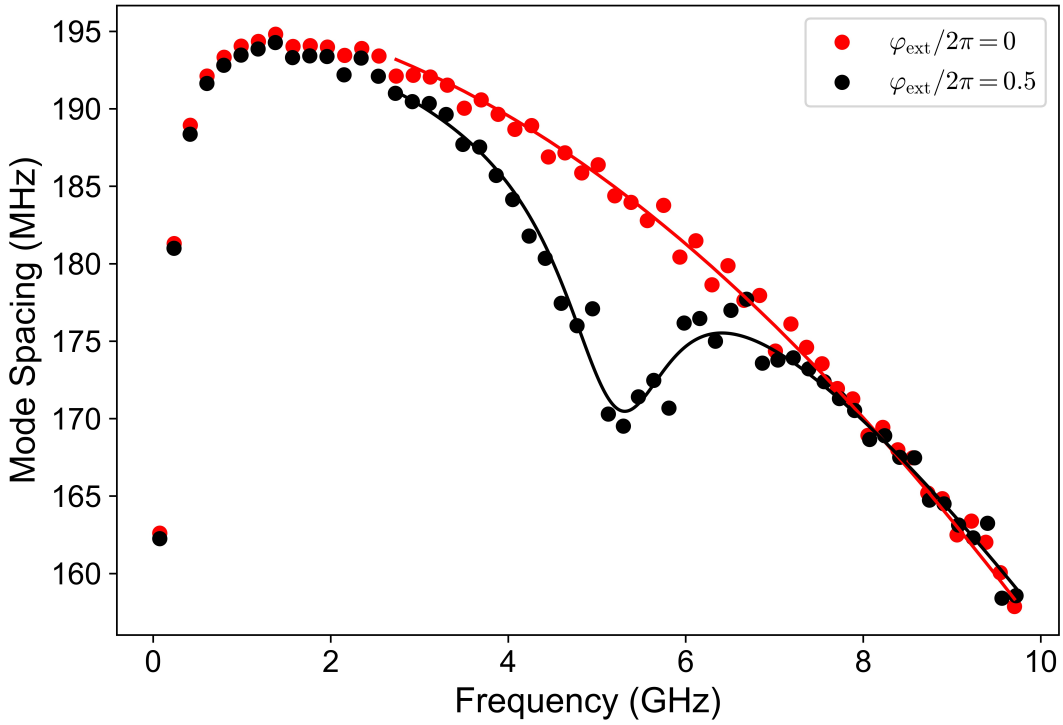

Figure 5.5: Mode spectral spacing (difference between the frequencies of two consecutive modes) versus frequency when the flux bias is $\varphi_{\rm ext}/2\pi = 0$ (red circles) and $\varphi_{\rm ext}/2\pi = 0.5$ (black circles). The decrease of mode spacing at low frequency is due to the antenna capacitance, while at high frequencies it occurs owing to the plasma cut-off frequency at $26.94\,\mathrm{GHz}$. Note also the Lorentzian dip in the mode spacing around the qubit transition frequency for the case of $\varphi_{\rm ext}/2\pi = 0.5$.

5.5.1 Bare Fabry-Perot cavity

In the experiment we can directly measure the bare transmission line frequencies $(f_k^{(m)})$ by performing spectroscopy of the single particle excitation frequencies when the flux through the qubit loop is set to an integer multiple of 2π. In this configuration the three wave mixing term induced by the qubit goes to zero. Furthermore, the qubit transition frequency is tuned to its highest $(f_{\rm eg} > 15\,\mathrm{GHz})$ and the transmission line modes below $10\,\mathrm{GHz}$ are effectively decoupled from the qubit. The single-particle energy spacing in our transmission line resonator in this case are fitted with high accuracy by a simple two-parameter model, which has an ultra-violet cut-off given by the plasma frequency

of the Josephson junctions [42] given by:

$$\Delta(f) = \frac{v}{2\ell}(1 - (f/f_p)^2)^{3/2} \tag{5.17}$$

where ℓ is the length of the transmission line and f_p is the plasma frequency of the Josephson junction making the transmission line. In addition to high frequency, the mode spacing is also distorted in the very low frequency limit due to the antenna capacitance. The amplitude of the random disorder fluctuations in the mode spacing is of the order of a few MHz, which is about 1% of the average mode spacing. This is probably due to the area fluctuations in the array of Josephson junctions making the slow-light Fabry-Perot resonator.

5.5.2 Fluxonium parameters

In the presence of the qubit, the energy spacing of the Fabry-Perot modes is distorted and displays a dip, as shown in Fig. 5.5. In this case the mode spacing as a function of frequency is given by :

$$\Delta(f) = \frac{v}{2\ell}(1 - (f/f_p)^2)^{3/2} + \frac{4\pi^2(f - f_{\mathrm{eg}})^2 + \pi^2\Gamma^2}{\Gamma} \tag{5.18}$$

Here f_{eg} is the ground to excited state transition frequency of the qubit. When the qubit is tuned to its minimum energy configuration corresponding to $\varphi_{\mathrm{ext}} = \pi$, we fit the dip in the mode spacing with a Lorentzian of width $\Gamma = 1.43\,\mathrm{GHz}$ [42]. This puts the device deep in the superstrong coupling regime with $\Gamma/\Delta \gtrsim 8$. We also checked that the qubit width remains constant for the frequency range of $5\,\mathrm{GHz}$ to $10\,\mathrm{GHz}$. This distortion in the mode spacing is as a result of linear hybridization of the qubit $|\mathrm{e}\rangle \leftrightarrow |\mathrm{g}\rangle$ transition with the bare Fabry-Perot modes. This hybridization of the flux dependent qubit transition with the cavity modes is responsible for the flux modulation of the single-particle spectrum of our effective Fabry-Perot cavity. Since, the flux modulation of the single-particle energy spectrum encodes information of the qubit, we use the experimentally measured single-particle spectrum as a function of the flux threading the superconducting loop of the qubit to extract the bare qubit parameters.

To accomplish this, we fit the single-particle mode frequencies with the energy eigenvalues of the truncated Hamiltonian of Eq 5.1, restricting the Hilbert space to the single-excitation subspace

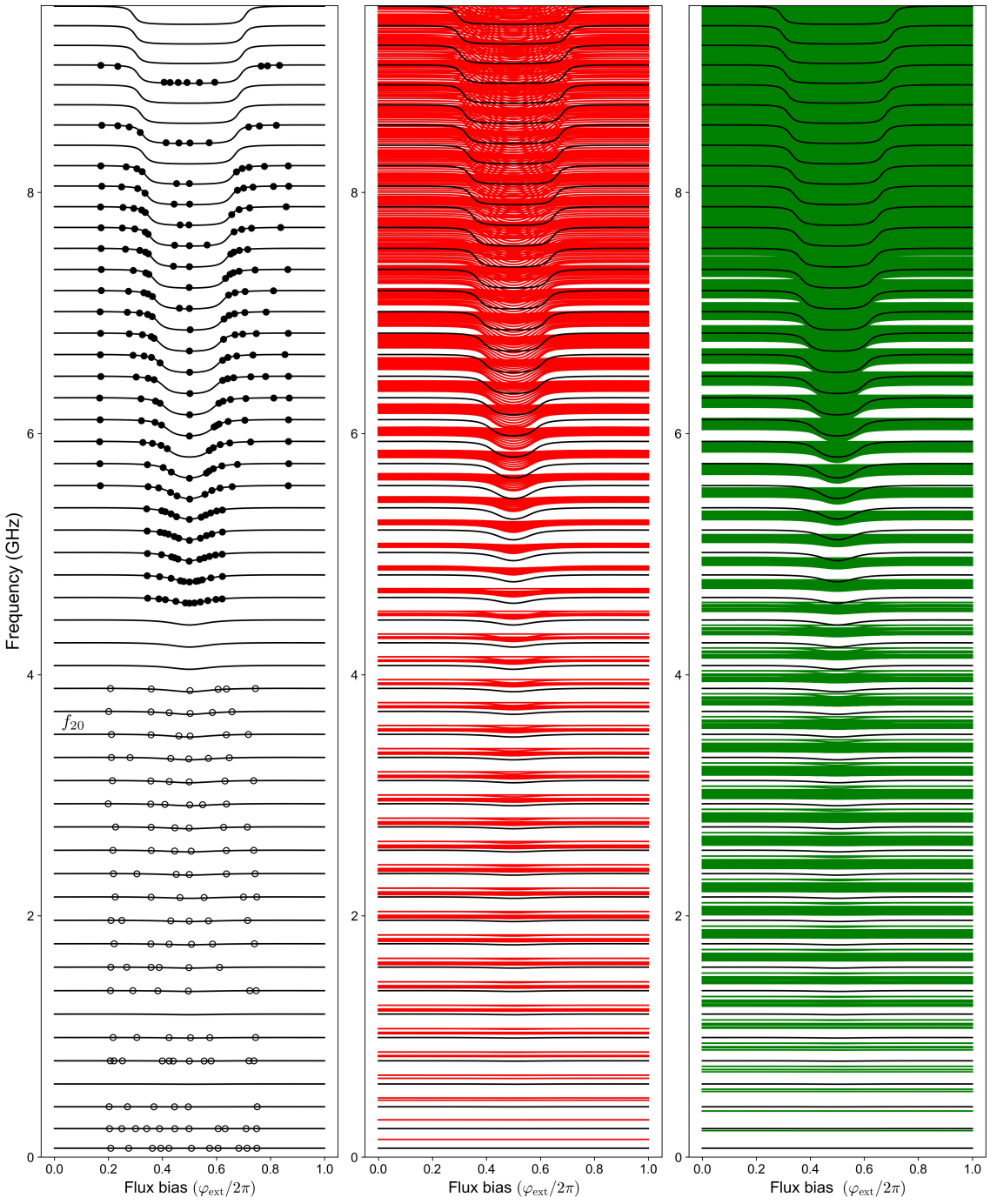

Figure 5.6: First column from the left: excitation frequency versus the applied flux bias for the single-particle eigenstates (black solid lines). The filled black circles are the experimental data used for the fitting procedure described in the text. Second column: energy of the uncoupled two-particle states (red lines). Third column: same but for the three-particle states (green lines).

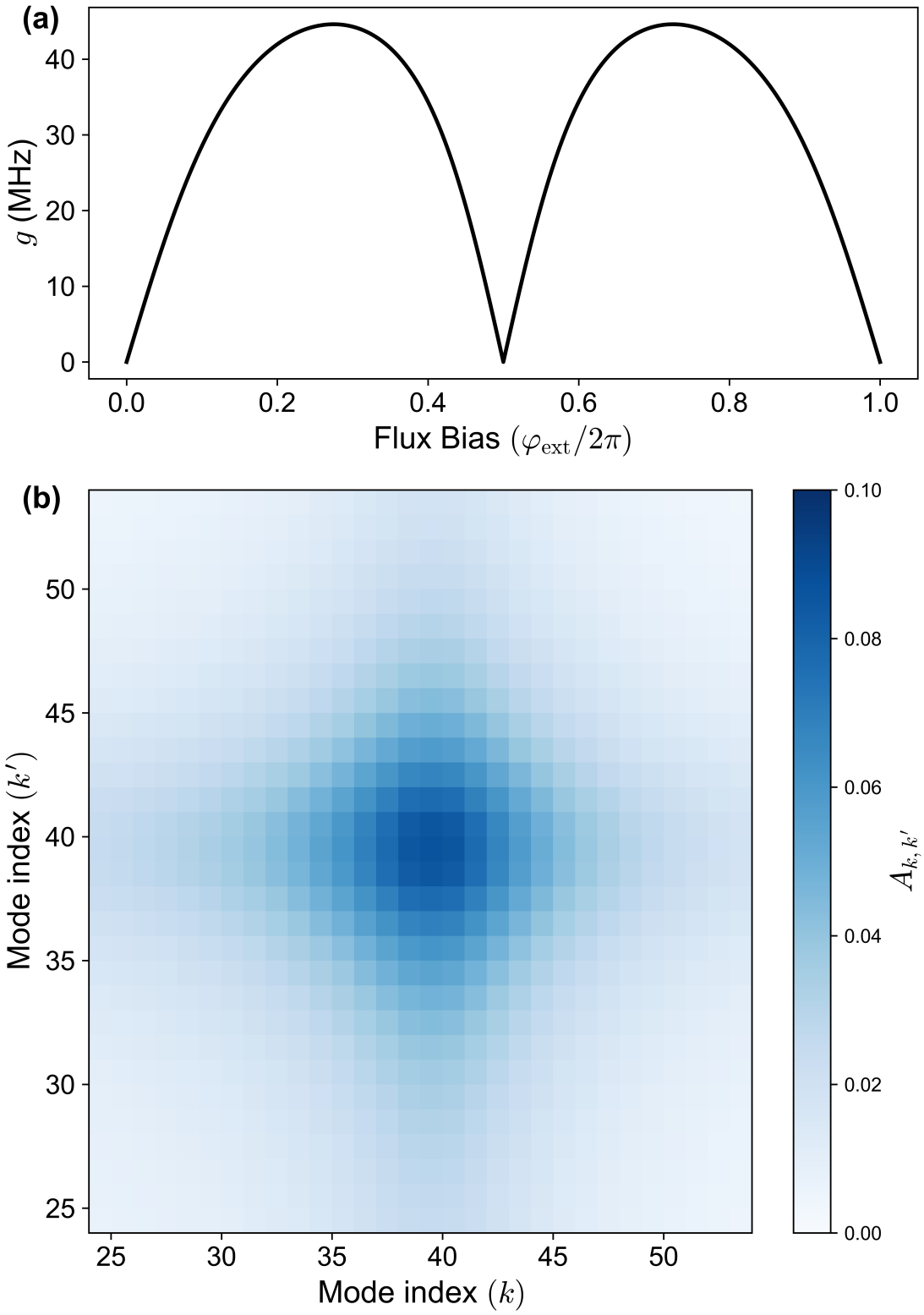

Figure 5.7: (a) Photon-photon interaction scale g as a function of the external flux. (b) Color plot of the matrix elements $A_{k,k'}$ versus the mode indices k, k' when the qubit frequency is tuned $f_{\mathrm{eg}} = 7.2\,\mathrm{GHz}$ (around mode index 39) at $\varphi_{\mathrm{ext}}/2\pi = 0.36$. Note that the width of the local maximum in $A_{k,k'}$ is given by Γ/Δ.

(see Eq. 5.7). We use a standard least mean squares minimization algorithm to find the optimal values (E_C, E_L, E_J). The data points used in the fitting algorithm are shown in Fig 5.6 (a) as filled black circles and the corresponding calculated frequencies are represented by the solid black lines. The Hamiltonian in the single-excitation subspace can then be written as $\hat{H}_0/h = \sum_{k>0} f_k \hat{a}_k^\dagger \hat{a}_k$, where $\hat{a}^\dagger(\hat{a}_k)$ denotes the normal mode creation (destruction) operator and f_k is the corresponding normal mode frequency, which is now a function of the flux threading the qubit loop. The hybrid single-particle states can now be written as a linear superposition of the qubit excited state and single photon state in one of the transmission line modes.

$$\hat{a}_k^\dagger|G\rangle = \hat{b}_k^\dagger|G\rangle\,, k \leq i_0 \tag{5.19}$$

$$\hat{a}_k^\dagger|G\rangle = W_{k,0}|\mathrm{e}\rangle|0\rangle + \sum_{k'>i_0} W_{k,k'}|\mathrm{g}\rangle\hat{b}_{k'}^\dagger|0\rangle\,, k > i_0 \tag{5.20}$$

Note that the hybridization coefficient $W_{k,0}$ goes to zero rapidly as the detuning between the normal mode frequency f_k and the qubit transition frequency f_{eg} exceeds Γ (see Fig 5.7(b)). Having the single-particle energies, we can also generate the bare two and three-particle energy spectrum, as shown in Fig 5.6 (b) and (c) respectively. Obtaining the bare Fabry-Perot and fluxonium parameters also allows us to completely reconstruct the effective Hamiltonian parameters of Eq. 5.12. The reconstructed three wave mixing strength g and the matrix elements $A_{k,k'}$ are plotted in Fig. 5.7 (a), (b) respectively.

5.6 Reflection spectroscopy

In this section we report detailed single and two tone spectroscopy of the system by measuring the reflection coefficient $|S_{11}(\omega)|$ of microwaves on the single port of the 3-D waveguide (see Chapter 3) in which the chip containing the device is housed. Our experiment consists of measuring the reflection magnitude $|S_{11}|$ at the port end of the cavity, following previously established procedures [42]. The incident power excites the cavity with less than one photon, on average, and we checked that the resulting spectra are power-independent.

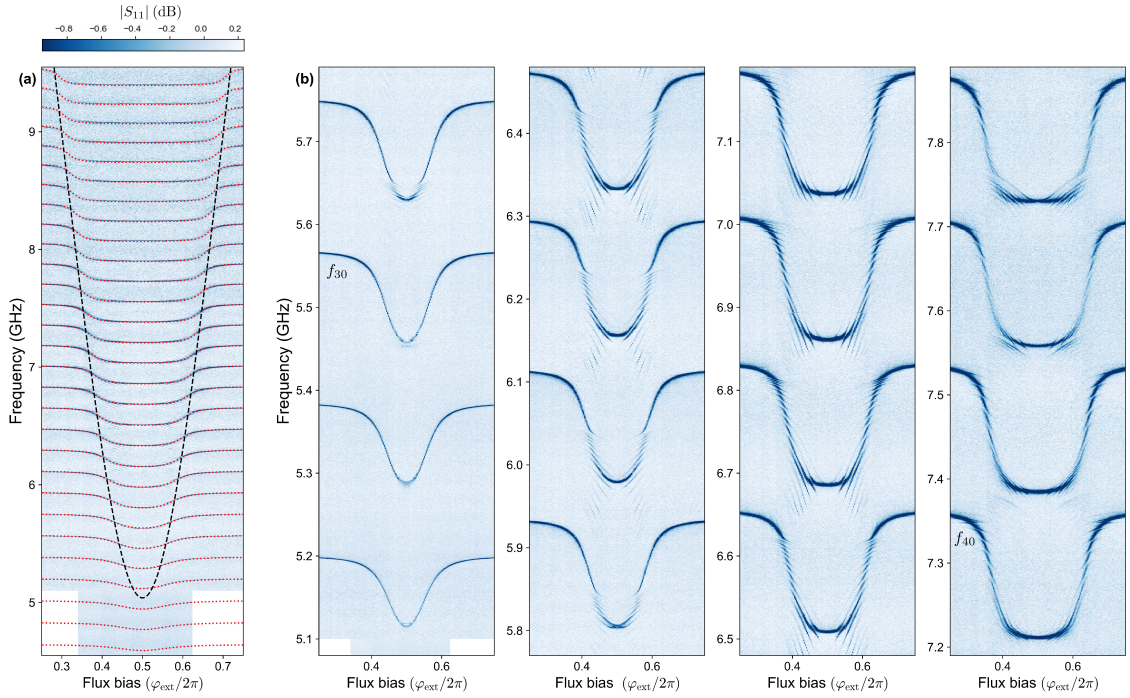

Figure 5.8: (a) Linear (low-power limit) reflection spectroscopy signal $|S_{11}|(\mathrm{dB})$ of the multi-mode circuit QED system as a function the external flux bias. The black-dashed lines show the fitted $|\mathrm{g}\rangle \leftrightarrow |\mathrm{e}\rangle$ transition frequency of the fluxonium atom, while the red-dotted lines depict the calculated energy spectrum in the single-excitation manifold. (b) Closer look at the spectra that, depending on the frequency, can display an additional fine structure with satellite resonances.

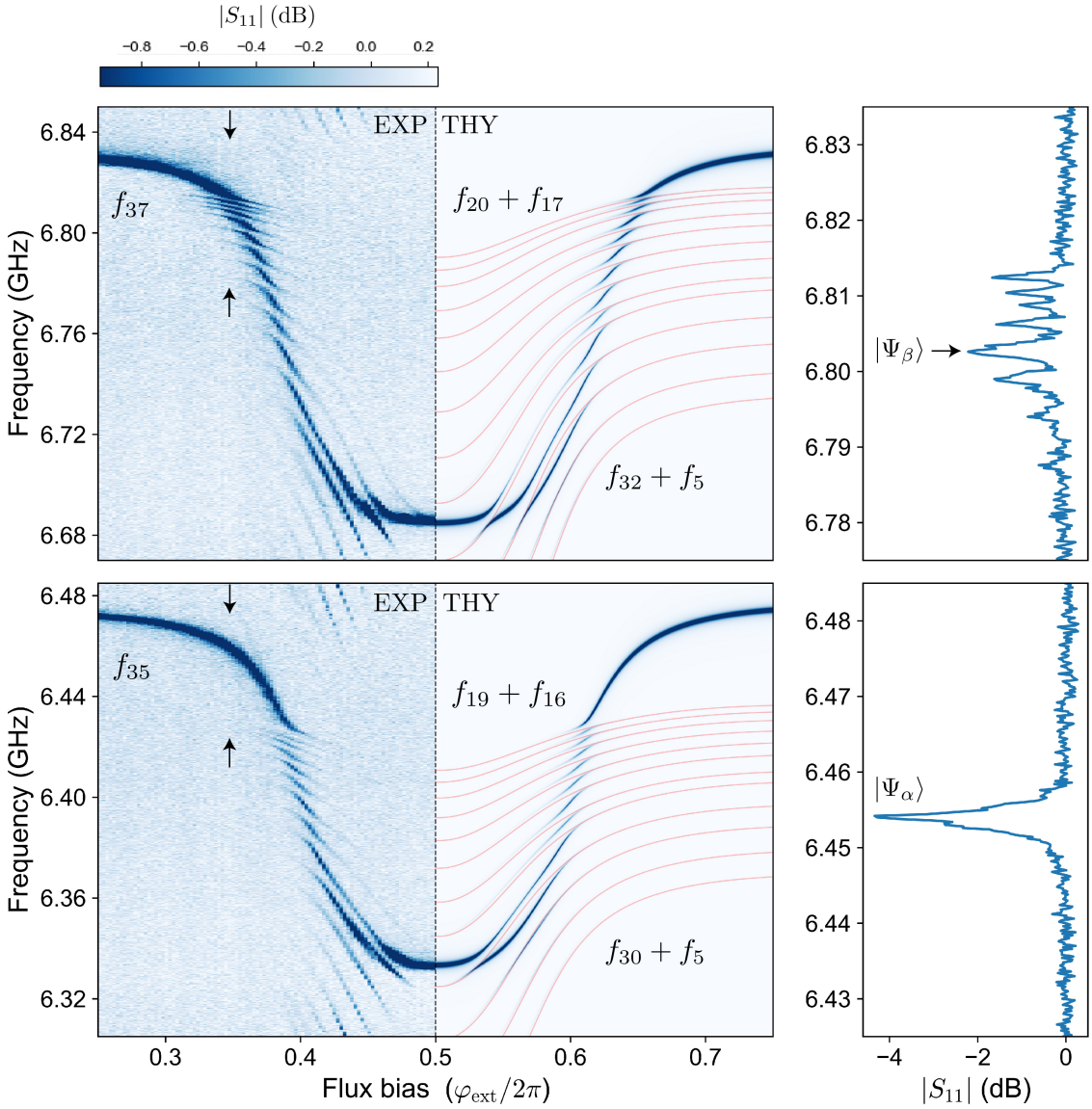

Figure 5.9: Reflection magnitude S_{11} (dB) near modes $k = 35$ and $k = 37$, data for $\varphi_{\text{ext}}/2\pi < 0.5$, theory in the two-particle approximation without adjustable parameters for $\varphi_{\text{ext}}/2\pi > 0.5$. The red lines show uncoupled two-particle energy levels taken directly from the lower-frequency data. The insets show a line cut for an illustrative flux bias $\varphi_{\text{ext}}/2\pi = 0.356$.

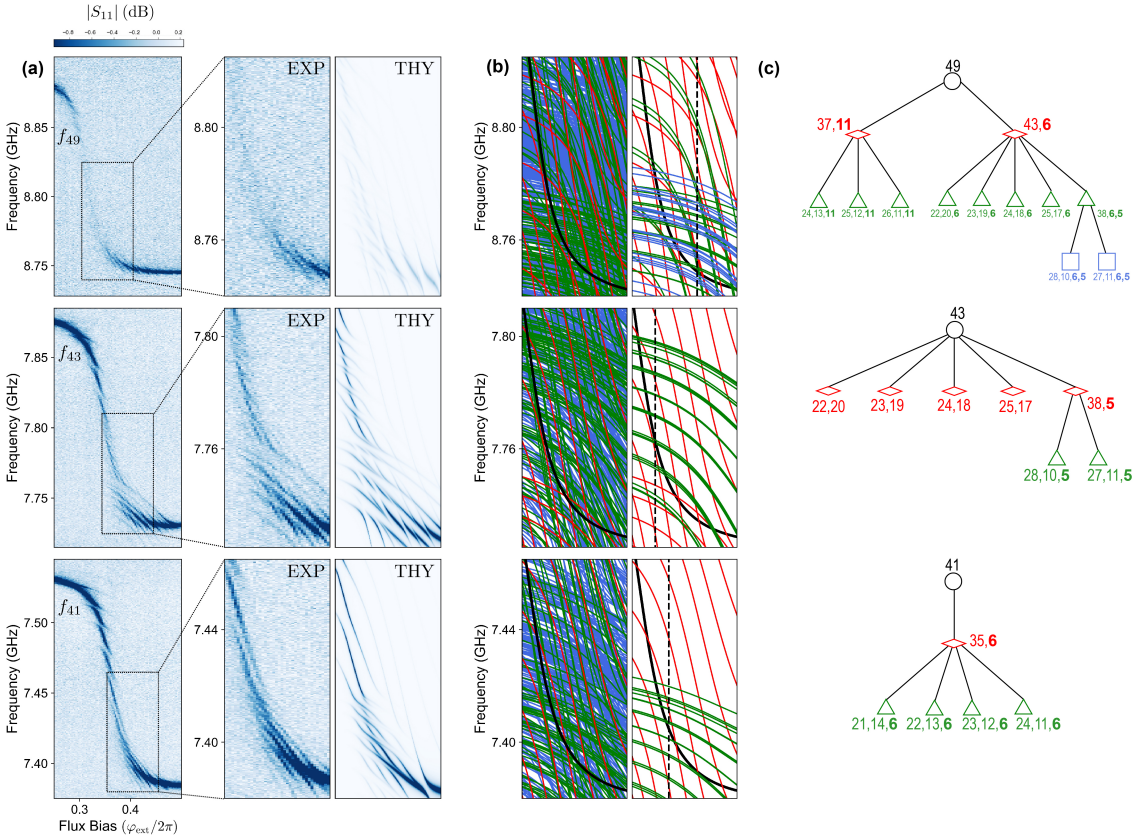

Figure 5.10: (a) Reflection magnitude $|S_{11}|(\mathrm{dB})$ near modes 49, 43 and 41. Insets (left to right): (left) zoom on the spectroscopy data in the 100 MHz wide windows; (right) calculated spectrum, no adjustable parameters. (b) Energies of all possible (left), with non-zero matrix element (right) uncoupled single-particle (black), two-particle (red), three-particle (green), and four-particle (blue) states in the $100\,\mathrm{MHz}$ window. (c) Examples of many-body Fock space trees describing the localization dynamics at selected flux values, indicated by the vertical dashed line in the insets of (a). Note, density of interconnected states is is much smaller than that of all multi-particle states.

5.7 Interpretation of spectroscopy: Many-body localization of photons

Let us first discuss the coarse frequency resolution data (Fig. 5.8 (a)). It shows the expected sequence of standing wave resonances for modes $k = 25, 26, ..., 50$, whose frequencies f_k are modulated by the magnetic flux φ_{ext} due to the qubit admixture. The flux-modulation rapidly vanishes for modes with $k < 25$. The measured values f_k agree with a single-particle (linear) hybridization model detailed in

section 5.5.2 (Fig. 5.8 (a), dotted lines). Fitting this model provides reliable estimates of all circuit parameters (see Table 5.1 in particular row with $x = 0.5$). For example, we obtain $\Gamma \approx 1.4$ GHz ($\Gamma/\Delta \approx 8$) as well as the uncoupled qubit frequency (Fig. 5.8 (a), dashed line). The flux knob can continuously modify our system, including switching off the interaction $\hat{V}$ at $\varphi_{\text{ext}} = 0, \pi$. In addition to adjusting the single-particle spectrum, we can maximize the interaction effects for a given mode k by setting $f_{\text{eg}}(\varphi_{\text{ext}}) \approx f_k \pm \Gamma$. This condition graphically corresponds to the sloped region of $f_k(\varphi_{\text{ext}})$ in Fig. 5.8 (a).

A higher resolution data reveals dramatic deviations from the single-particle picture (Fig. 5.8 (b)). Namely, the cavity resonances with $k > 30$ anticross many new flux-dependent lines. The splitting size varies from line to line, but remains much smaller than Δ. The most unusual property of these new spectral lines is that their density is much larger than $1/\Delta$, especially towards higher frequencies. Indeed, where would so many states possibly come from in a cavity excited by at most one photon? In fact, these are precisely the multi-particle states introduced in chapter 1. In fact, one can use the f_k-data to duly check that each new resonance around the modes $k = 31 - 39$ in Fig. 5.8 (b) satisfies the two-particle matching condition $f_k = f_{k'} + f_j$, for selected integer pairs $k', j < k$. For $k \leq 30$ there are no matching two-particle states in our system irrespective of the flux bias.

Zooming in to several modes ($k = 35, 37$) we find a remarkably good agreement between data and the two-particle spectrum of Hamiltonian (Eq. 5.12), produced without adjustable parameters (Fig. 3). The matrix elements of $\hat{V}$ were calculated using the circuit parameters obtained from fitting the single-particle model(see section 5.5.2). The theoretical $|S_{11}|$-signal in Fig. 5.9 involves the two-particle wavefunctions as well as the values of the intrinsic and extrinsic quality factors of the cavity resonances, which were measured at the non-interacting flux bias $\varphi_{\text{ext}} = 0$. We stress that linear spectroscopy only lights up states with a substantial single-particle component, which is why the two-particle resonances appear as a "fine structure" around the cavity mode frequencies.

The example spectra shown in Fig. 5.9 are inconsistent with the Fermi's Golden rule decay rate theory, but they have a straightforward interpretation in terms of localization in the many-body Fock space. We focus on a specific realization of our system at $\varphi_{\text{ext}}/2\pi = 0.356$ (Fig. 5.9 - insets). Thus, mode $k = 35$ appears as a single resonance (as well as all modes $k < 35$) and it is accurately

described by a single-particle wavefunction, $|\Psi_\alpha\rangle \approx \hat{a}^\dagger_{35}|0\rangle$. A photon excited in this mode does not make any attempt to split because the nearest available two-particle states are far detuned compared to the interaction scale. By contrast, a slightly higher frequency mode $k = 37$ fragments into at least eight resolved resonances. Each of them is described by a many-body localized wavefunction, for instance (as marked in Fig. 5.9 - insets), $|\Psi_\beta\rangle \approx 0.58\ \hat{a}^\dagger_{37}|0\rangle + 0.102\ \hat{a}^\dagger_{25}\hat{a}^\dagger_{12}|0\rangle + 0.184\ \hat{a}^\dagger_{24}\hat{a}^\dagger_{13}|0\rangle + 0.512\ \hat{a}^\dagger_{23}\hat{a}^\dagger_{14}|0\rangle - 0.53\ \hat{a}^\dagger_{22}\hat{a}^\dagger_{15}|0\rangle - 0.223\ \hat{a}^\dagger_{21}\hat{a}^\dagger_{16}|0\rangle - 0.125\ \hat{a}^\dagger_{20}\hat{a}^\dagger_{17}|0\rangle$. This wavefunction consists of a superposition of the original single-particle state, with a probability $0.58^2 \approx 34\%$, and several nearly-resonant two-particle states. One may say that a photon excited in mode $k = 37$ does make attempts to split, e.g. into a pair of photons in modes $22, 15$ or $23, 14$. However, since these secondary photons are stable ($k < 35$), the down-conversion dynamics localizes to a few two-particle sites in the Fock space and hence remains coherent.

The extent of localized states rapidly grows for higher-frequency modes (Fig. 5.10 (a)). In particular, the data around modes $k = 41, 43$ contains extra-fine spectral features that cannot be explained within the two-particle approximation but agree with the three-particle spectrum of Hamiltonian (Eq. 5.12). We illustrate the composition of many-body resonances using the Fock-space hopping trees. For clarity, we retain only the strongest branches, for which the hopping amplitude (the matrix element of $\hat{V}$) exceeds the energy mismatch. In the example of mode $k = 41$ (at $\varphi_{\text{ext}} = 0.39$), a single-particle state $\hat{a}^\dagger_{41}|0\rangle$ hybridizes predominantly with one two-particle state $\hat{a}^\dagger_{35}\hat{a}^\dagger_{6}|0\rangle$, which itself hybridizes with four three-particle states $\hat{a}^\dagger_{21}\hat{a}^\dagger_{14}\hat{a}^\dagger_{6}|0\rangle$, $\hat{a}^\dagger_{22}\hat{a}^\dagger_{13}\hat{a}^\dagger_{6}|0\rangle$, $\hat{a}^\dagger_{23}\hat{a}^\dagger_{12}\hat{a}^\dagger_{6}|0\rangle$, $\hat{a}^\dagger_{24}\hat{a}^\dagger_{11}\hat{a}^\dagger_{6}|0\rangle$. The tree terminates at those four three-particle states because the corresponding third-generation photons are stable (see Fig. 5.9 (b)). Same analysis applies to the spectrum around mode $k = 43$ ($\varphi_{\text{ext}}/2\pi = 0.367$), which reveals not only three-particle states but also an increasing density of two-particle states.

As the density of multi-particle states grows with energy, one may wonder if the Fermi's Golden rule recovers for higher-frequency modes. We note, though, that our system has a finite coupling to an external bath, both due to leaking of photons into the measurement apparatus and materials absorption. Therefore, as the localization extends to larger and larger number of multi-particle states, their frequency spacing would eventually become comparable to their external linewidth, which in our system is of order 1 MHz. In this case, the fine spectral structure would merge into

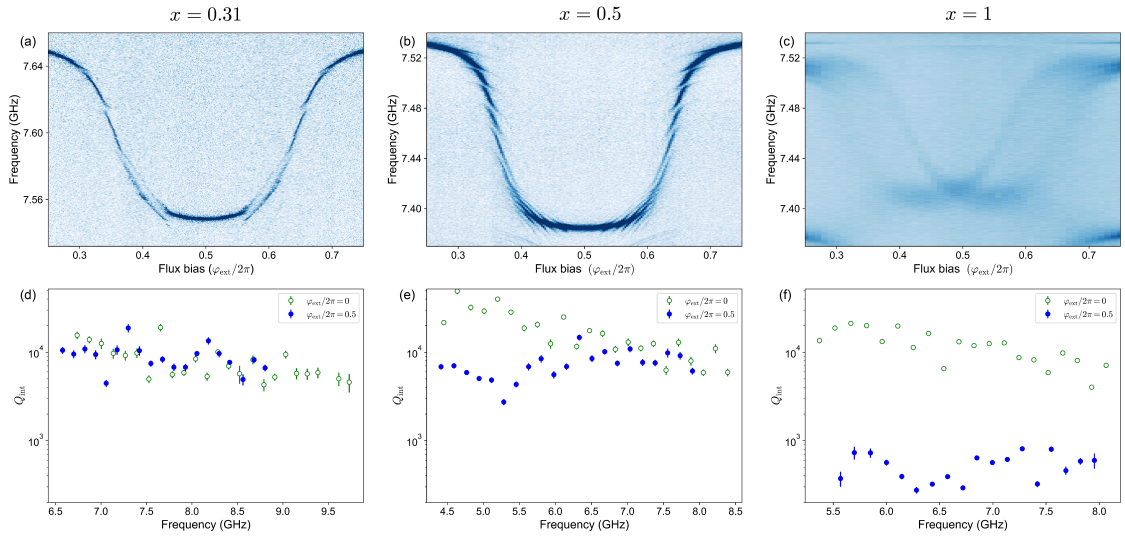

Figure 5.11: (a - c) Reflection spectroscopy signal $|S_{11}|$ (expressed in dB) near 7.5 GHz mode of the Fabry-Perot cavity for devices with geometric coupling ratio $x = 0.31$ (a), $x = 0.5$ (b) and $x = 1$ (c) . (d - f) Intrinsic quality factor measured for the standing wave modes in the same three devices as (a - c) for $\varphi_{ext}/2\pi = 0$ and $\varphi_{ext}/2\pi = 0.5$.

a single broad resonance, effectively recovering the applicability of the Fermi's Golden rule in the otherwise localized system. This fundamental effect limits our present resolution to two- and three-particle states, as can be seen by the example of mode $k = 49$, where one expects four-particle states to appear (Fig. 5.10).

5.8 Towards strongly correlated photons

In this section we describe the spectroscopy data for devices with geometric ratio $x < 0.5$ and $x > 0.5$. We observe that as we decrease x, the width of the qubit transition decreases and the qubit hybridizes with less number of modes Γ/Δ. The direct consequence of this on the spectrum is the decrease in the density of two-particle anticrossings. This is due to the fact that the matrix element decreases more rapidly as the factor $A_{k,k'}$ decreases faster as $|k - k'|$ grows. The exact opposite happens for the case of $x > 0.5$, we observe an increased density of two-particle anticrossings. As we continue increasing x, we observe that for $x = 1$, the spectrum changes qualitatively. Instead of an increased density of multi-particle anti-crossings we observe that the standing wave resonance in

this case is completely washed away into what looks like a continuum. This is the regime where the qubit width becomes comparable to $\Gamma \sim f_{\mathrm{eg}}$ and the effective Hamiltonian described in section 5.3 is no longer applicable. In this regime we can no longer make a two-band distinction between low and high-frequency modes which brakes the strict selection rule that limit the connectivity in the many-body fock space. Here the single particle state of the cavity becomes dressed in all possible multi-photon states resonant with the single particle state creating a truly strongly correlated photon state.

Additional evidence of this direct coupling of single-particle state to multi-particle states can be seen by measuring the quality factor of the cavity standing wave resonances at the external flux bias points of $\varphi_{\mathrm{ext}}/2\pi = 0$ and $\varphi_{\mathrm{ext}}/2\pi = 0.5$. At these specific flux bias points the three-wave mixing non-linearity goes to zero. The main difference between the two flux bias points is the qubit frequency. For $\varphi_{\mathrm{ext}}/2\pi = 0$ the qubit is tuned to its maximum frequency whereas for $\varphi_{\mathrm{ext}}/2\pi = 0.5$ it is tuned to its minimum frequency. We observe that when $\Gamma \ll f_{\mathrm{eg}}$ there is no difference in the intrinsic quality factors for the two flux bias points however as the Γ increases and approaches f_{eg}, we observe a more than an order of magnitude drop in the intrinsic quality factor of resonances (see Fig. 5.11). This drop in the quality factor is due to the de-localization of the single-particle excitation into the many-body Fock space. A precise theoretical model of this decay of single particle excitation is currently not available at the time of the writing of this work and is the subject of ongoing theoretical and experimental work.

5.9 Conclusion

To summarize, we showed that spontaneous down-conversion of a single photon in the quantum impurity regime of cavity QED is a many-body phenomenon and it is subject to many-body localization (MBL). Localization leads to a breakdown of Fermi's Golden rule description of the down-conversion rate, by analogy with the original prediction for a confined Fermi-liquid quasiparticle [43]. As a result, the standing wave modes fragment into a spectacular fine structure of multi-particle resonances, which unambiguously distinguishes MBL from either the delocalization regime (single interaction-broadened resonance) or the non-interacting photons (single sharp resonance).

5.10 Summary of device parameters

Device (x)	$v/10^6$(m/s)	Z_∞(kΩ)	Δ(MHz)	Γ(GHz)	E_J(GHz)	E_C(GHz)	E_L(GHz)
0.07	2.18	9.33 ± 0.5	182	< 0.2	8.12 ± 0.05	5.69 ± 0.04	1.42 ± 0.01
0.3	1.82	10.05 ± 1.04	151	0.61 ± 0.03	2.62 ± 0.10	6.97 ± 0.2	1.12 ± 0.02
0.5	2.36	8.97 ± 0.67	197	1.43 ± 0.02	8.9 ± 0.6	8.0 ± 0.4	1.39 ± 0.05
0.65	2.03	9.62 ± 0.01	169	2.10 ± 0.1	3.62 ± 0.3	6.72 ± 0.2	1.04 ± 0.01
1	1.93	10.4 ± 0.4	161	-	-	-	-

Table 5.1: Device parameters extracted by performing characterization experiments detailed in section 6.5. Note that the length of all the devices presented in this table was 6 mm.

Chapter 6

Transmon impurity galvanically coupled to multi-mode cavity

In this chapter we describe the experimental implementation and characterization of multi-mode cavity QED system where we galvanically couple a flux tunable transmon qubit to the multi-mode Fabry-Perot cavity introduced in the chapter 4. We study the elastic and inelastic scattering of microwaves off the impurity. We characterize the elastic scattering by measuring the frequency shift induced by the tranmson on the standing wave modes of the Fabry-Perot cavity. We characterize the inelastic scattering by measuring the line width of the standing wave modes. Furthermore, we derive an effective photon-photon coupling Hamiltonian for our system and explain the measurements across multiple devices using the theory.

6.1 Design of the device

The system we study in this chapter consists of a two-wire transmission line of length $\ell = 6\,\mathrm{mm}$ (except for device 0a, where $\ell = 12\,\mathrm{mm}$), characterized by its wave impedance Z_∞ and speed of light v, identical to the one shown in Fig. 4.2 (a) but with a small modification at the right end. Instead of a short circuit now we terminate this transmission line by a two junction SQuID (Superconducting Qunatum Interference Device) which forms our flux tunable transmon artificial

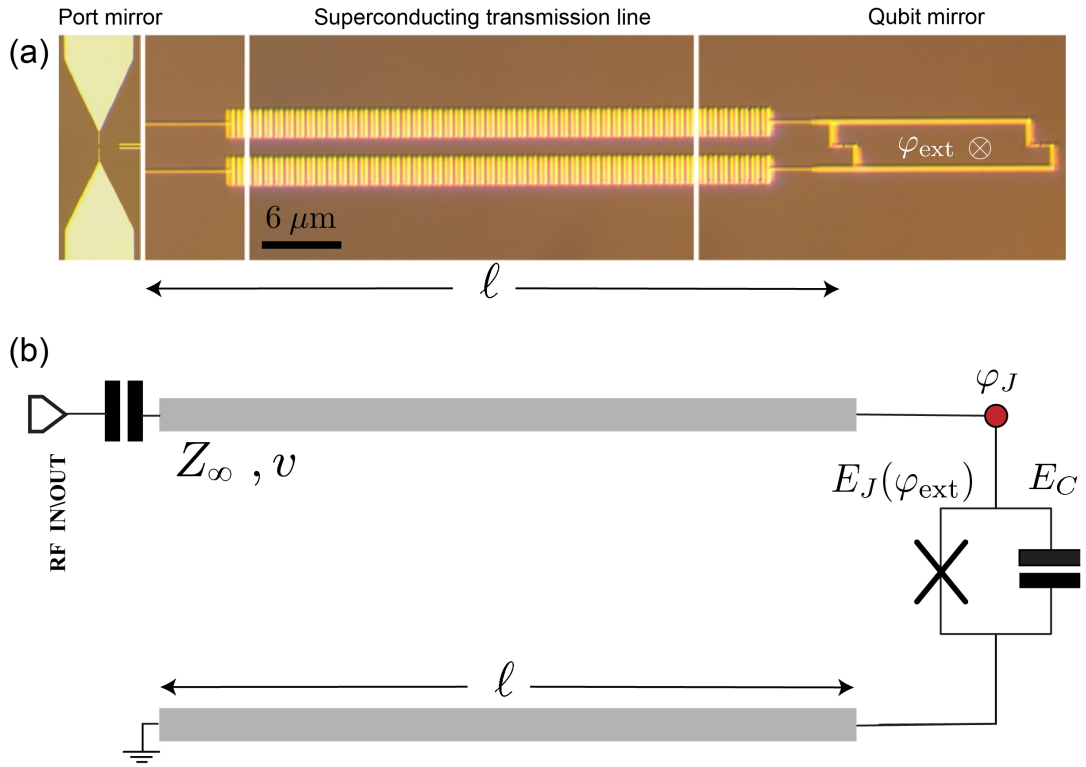

Figure 6.1: Optical micrograph (a) and circuit schematic (b) of the system showing a two-wire transmission line terminated by a superconducting transmon qubit. The transmission line is characterized by its wave impedance Z_∞, speed of light v, and length ℓ. The transmon is defined by the Josephson energy E_J, the charging energy E_C of the small junction. The two wires of the transmission line are terminated with the SQuID loop, coupling galvanically the qubit to the cavity's standing wave modes. The qubit transition frequency can be tuned by changing the external flux bias $(\hbar/2e)\varphi_{\rm ext}$ threading the SQuID loop.

atom. The SQuID geometry allows us to tune the effective Josephson energy E_J and through it the transmon resonance frequency.

6.2 Microscopic Hamiltonian

The system described in this work can be modeled as a transmon qubit coupled galvanically to a high-impedance transmission line cavity. By decomposing the extended transmission line into its lumped element foster form and using the charge gauge we can arrive at the exact microscopic Hamiltonian of our system (see section 2.4.2). The Hamiltonian consists of three terms, the first two terms define the bare transmon qubit and the bare non-interacting bosonic modes of the Fabry-Perot cavity. The third term defines the coupling between the two.

$$\hat{H} = \hat{H}_{\text{qubit}} + \hat{H}_{\text{modes}} + \hat{H}_{\text{int}}, \tag{6.1}$$

Explicitly the three terms are defined as:

$$\hat{H}_{\text{qubit}}/h = 4E_C\hat{n}_J^2 - E_J\cos(\hat{\varphi}_J), \tag{6.2}$$

$$\hat{H}_{\text{modes}}/\hbar = \sum_{i=1}^{\infty} \omega_i^{(c)} \hat{a}_i^\dagger \hat{a}_i, \tag{6.3}$$

$$\hat{H}_{\text{int}}/h = -\mathrm{i}\hat{n}_J \sum_{i=1}^{\infty} g_i^{(c)} (\hat{a}_i - \hat{a}_i^\dagger), \tag{6.4}$$

here the Hamiltonian parameters are related to an exact circuit model. The corresponding circuit model and detailed procedure to arrive at the specific Hamiltonian parameters can be found in section 2.4.1.2.

6.3 Effective Hamiltonian

In this section, we derive the effective Hamiltonian treatment that can be applied to the system in two different parameter regimes. First we will consider the parameter regime where the $E_J/E_C \gg 1$ of the transmon qubit. In this case the transmon qubit can be modelled as an harmonic oscillator with a perturbative Kerr type non-linearity. In the second case we will consider the regime where the E_J/E_C is decreased and a new type of non-linearity arises that of phase-slip across the transmon's Josephson junction.

6.3.1 Quartic non-linearity

As the transmon consists of an effective Josephson junction with $E_J/E_C \gg 1$, it can be simply replaced by an harmonic oscillator with a resonance frequency equal to the frequency of the lowest two energy levels $\omega_{\text{eg}} = \sqrt{8E_J E_C} - E_C$ and impedance $R_Q\sqrt{4E_C/\pi^2 E_J}$ with an effective Kerr non-linearity equal to E_C. In this case our system reduces to a system of coupled harmonic oscillators. We can then write the effective Hamiltonian of the system as:

$$\hat{H}_{\text{eff}}/\hbar = \omega_{\text{eg}}\hat{a}_0^\dagger\hat{a}_0 - E_C(\hat{a}_0^\dagger\hat{a}_0)^2 + \sum_{j>0}\omega_j\hat{a}_j^\dagger\hat{a}_j \tag{6.5}$$
$$-(\hat{a}_0 - \hat{a}_0^\dagger)\sum_{j>0} g_j(\hat{a}_j - \hat{a_j}^\dagger) + \Big(\sum_{j>0}\frac{g_j}{\omega_{\text{eg}}^{1/2}}(\hat{a}_j + \hat{a}_j^\dagger)\Big)^2.$$

This Hamiltonian is a textbook Caldeira-Leggett model of a quantum degree of freedom interacting with an Ohmic bath [76]. The last term is the rigorously derived "A^2"-term of quantum optics. Note that in our model $g_j^2 \sim 1/j$, which regularizes perturbative series automatically, without the need for sophisticated analysis recently proposed for a capacitively connected transmon [19, 77]. We treat the weak non-linearity of the transmon as a perturbation and diagonalize the remaining quadratic terms of the effective Hamiltonian by a Bogoliubov transformation and arrive at the following final result:

$$\hat{H}_{\text{eff}}/\hbar = \sum_{j>0}\omega_j\hat{c}_j^\dagger\hat{c}_j - \sum_{j>0}K_j(\hat{c}_j^\dagger\hat{c}_j)^2 - \sum_{i,j}\chi_{i,j}\hat{c}_i^\dagger\hat{c}_i\hat{c}_j^\dagger\hat{c}_j, \tag{6.6}$$

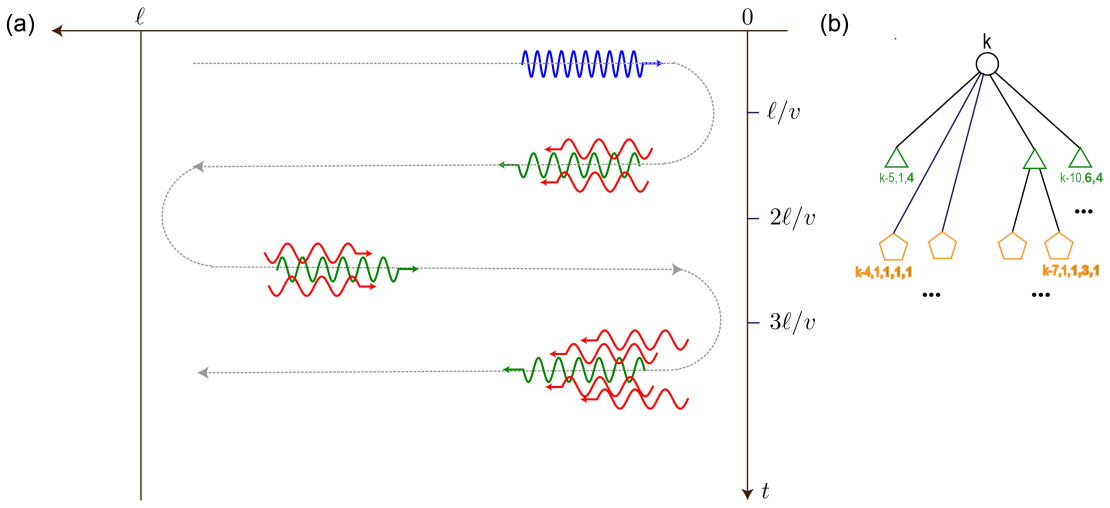

Figure 6.2: (a) Illustration showing inelastic scattering process that splits an incident single photon at $x = 0$ in one resonant photon and even number of low-frequency photons. (b) Schematic showing the coupling between many-body states induced by the transmon.

where

$$\begin{pmatrix} \hat{\boldsymbol{a}} \\ \hat{\boldsymbol{a}}^\dagger \end{pmatrix} = \begin{pmatrix} \boldsymbol{u} & \boldsymbol{v} \\ -\boldsymbol{v} & \boldsymbol{u} \end{pmatrix} \begin{pmatrix} \hat{\boldsymbol{c}} \\ \hat{\boldsymbol{c}}^\dagger \end{pmatrix}, \tag{6.7}$$

and

$$K_j = E_C(v_{1,j}^2 - u_{1,j}^2)^2/\hbar, \tag{6.8}$$
$$\chi_{i,j} = 4E_C(v_{1,j}^2 - u_{1,j}^2)(v_{1,j}^2 - u_{1,j}^2)/\hbar.$$

This effective Hamiltonian describes a new multi-mode Fabry-Perot cavity with flux dependent standing wave modes ω_j, $j = 1, 2, \ldots$ with an additional photon-photon Kerr type interaction. The flux dependence and non-linearity of the cavity are both acquired as a result of hybridization of the transmon oscillator with the bare Fabry-Perot cavity modes.

6.3.2 Phase-slip non-linearity

As we decrease the E_J/E_C of the transmon coupled to the cavity a new type of non-linearity appears from the quantum phase-slip fluctuations across the transmon junction [78, 79]. Namely, tunneling of the phase between the equivalent minima of the Josephson potential.

To derive the effective Hamiltonian we start with the microscopic Hamiltonian in the form given in Eq. 2.58. We begin by dividing the transmission line modes into two sets following a procedure similar to the one followed in section 5.3. The first set of modes consists of high-frequency modes quasi resonant with the transmon and the low frequency modes far detuned from the transmon. This two-band distinction is always possible as long as the $\omega_{\rm eg} \gg \Gamma$. Here Γ is the spontaneous emission linewidth of the transmon into the bare cavity modes in the infinite length limit of the cavity. The microscopic Hamiltonian can be re-written as:

$$\hat{H} = 4E_C(\hat{n}_J - \sum_{i\leq i_0} \hat{n}_i)^2 - E_J\cos(\hat{\varphi}_J) + \sum_{i=1}^{\infty}\left(4E_{C_i}\hat{n}_i^2 + \frac{1}{2}E_{L_i}\hat{\varphi}_i^2\right) - 8E_C\hat{n}_J\sum_{i>i_0}\hat{n}_i. \tag{6.9}$$

In the first step, we ignore for the time being the effect of the low-frequency bosonic modes of the transmission line on the transmon and diagonalize the following Hamiltonian

$$\hat{H}_0/\hbar = \omega_{\rm eg}|{\rm e}\rangle\langle{\rm e}| + \sum_{i>0}\omega_i^{(c)}\hat{b}_i^\dagger\hat{b}_i - {\rm i}\hat{n}_J\sum_{i>i_0}g_i^{(c)}(\hat{b}_i - \hat{b}_i^\dagger). \tag{6.10}$$

This Hamiltonian represents a model where the transmon resonance is hydridized with the standing wave resonances of the Fabry-Perot cavity. This Hamiltonian can be easily diagonalized to get:

$$\hat{H}_0/\hbar = \sum_{i>0}\omega_i\hat{a}_i^\dagger\hat{a}_i, \tag{6.11}$$

where now $\omega_i/2\pi$ represents the excitation frequency of the normal modes of the device which are the result of hybridization of the transmon excited state $|{\rm e}\rangle$ with the single photon states in the bare

Fabry-Perot cavity modes defined as

$$\hat{a}_k^\dagger|\mathrm{g}\rangle|0\rangle = W_{k,0}|\mathrm{e}\rangle|0\rangle + \sum_{k'>0} W_{k,k'}|\mathrm{g}\rangle\hat{b}_{k'}^\dagger|0\rangle\,, \tag{6.12}$$

Note that for $k \leq i_0$ the hybridization of the qubit with the modes is completely neglected in our model, i.e., $\hat{a}_k^\dagger = \hat{b}_k^\dagger$ and $\omega_k = \omega_k^{(c)}$.

We now include the effect of the low frequency modes. A quick comparison of the qubit part of the Hamiltonian with the charge qubit Hamiltonian reveals that the charge operators for the low frequency modes take the place of the gate charge n_g described in Eq 6.9. It is possible to calculate the sensitivity of the transmon excited state energy level (see Eq. 2.43) to this gate charge and arrive at the final effective Hamiltonian which describes the interaction between the low and high frequency modes:

$$\begin{aligned} \hat{H}_{\mathrm{eff}}/\hbar &= \sum_{k>0} \omega_k \hat{a}_k^\dagger \hat{a}_k + \hat{V}, \\ \hat{V} &= \nu|\mathrm{e}\rangle\langle\mathrm{e}|\cos(2\pi\sum_{i\leq i_0}\hat{n}_i), \\ \hat{V} &= \nu\sum_{k,k'>i_0} W_{k,0}^* W_{k',0}\hat{a}_k\hat{a}_{k'}^\dagger\cos(2\pi\sum_{i\leq i_0}\hat{n}_i). \end{aligned} \tag{6.13}$$

This interaction describes an effective non-linear Fabry-Perot cavity which allows for scattering of a photon in a high-frequency mode k to a nearly resonant high frequency mode k' while emitting or absorbing an even number of low frequency modes. The scattering rate ν is proportional to the amplitude of phase slips across the transmon small junction when the transmon is in the first excited state. The exact expression for ν is given by Eq. 2.43.

6.4 Control experiments

We perform the same control experiments as described in section 5.4 to confirm that the microwaves propagate in the full length of the transmission line and the SQuID loop is not disconnected. In the interest of space and time we skip its details here.

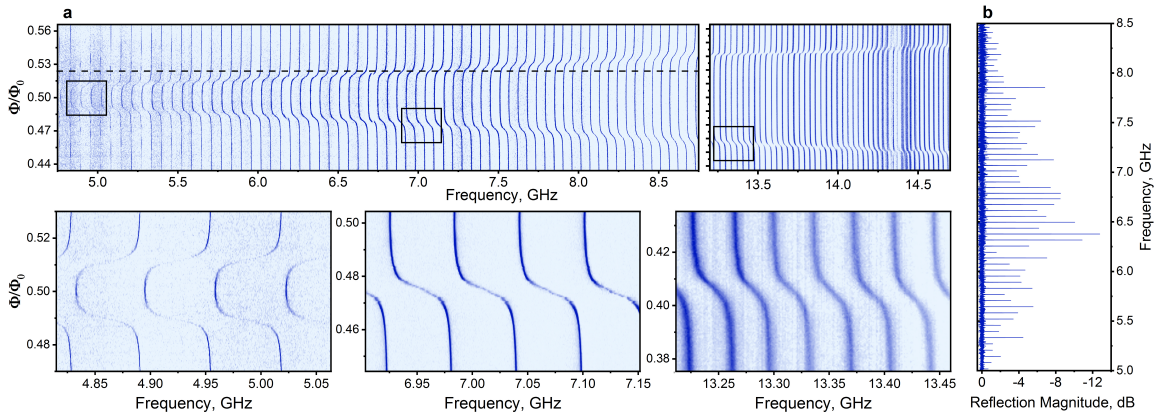

Figure 6.3: (a) Reflection magnitude as a function of probe frequency and external flux through the transmon SQuID loop. The color scale (not shown) is optimized to make the position of resonances maximally visible. The three insets have the same width along the frequency axis and correspond to the three boxed regions on the main plot. (b) An example slice of spectroscopy signal at the external flux $0.525 \times h/2e$, shown by the horizontal dashed line, where the transmon resonance is expected at around 7 GHz.

6.5 Characterization experiments

To characterize the devices we follow previously described single and two tone reflection spectroscopy techniques (see sections 4.2, 4.3.2) and use the spectroscopy data to extract the parameters for the bare Fabry-Perot cavity and the transmon qubit. In the following subsections we describe the main results of the experiments and compare them to the theory developed in the section 6.3. First we describe in detail experimental results from a device where the E_J/E_C of the SQuID junctions is large such that the phase slip amplitude is negligible. Next we will show the effect of progressively decreasing the E_J/E_C of the transmon when the phase slip amplitude becomes large and induces inelastic scattering of photons.

6.5.1 Large E_J/E_C device (0a)

6.5.1.1 Device parameters

In order to extract the parameters of the bare Fabry-Perot cavity we tune the flux threading the loop of the transmon's SQuID loop to an integer multiple of Φ_0. In this configuration the transmon resonance is tuned to the plasma cuttoff $\omega_p/2\pi$ and the modes of the bare Fabry-Perot cavity in the

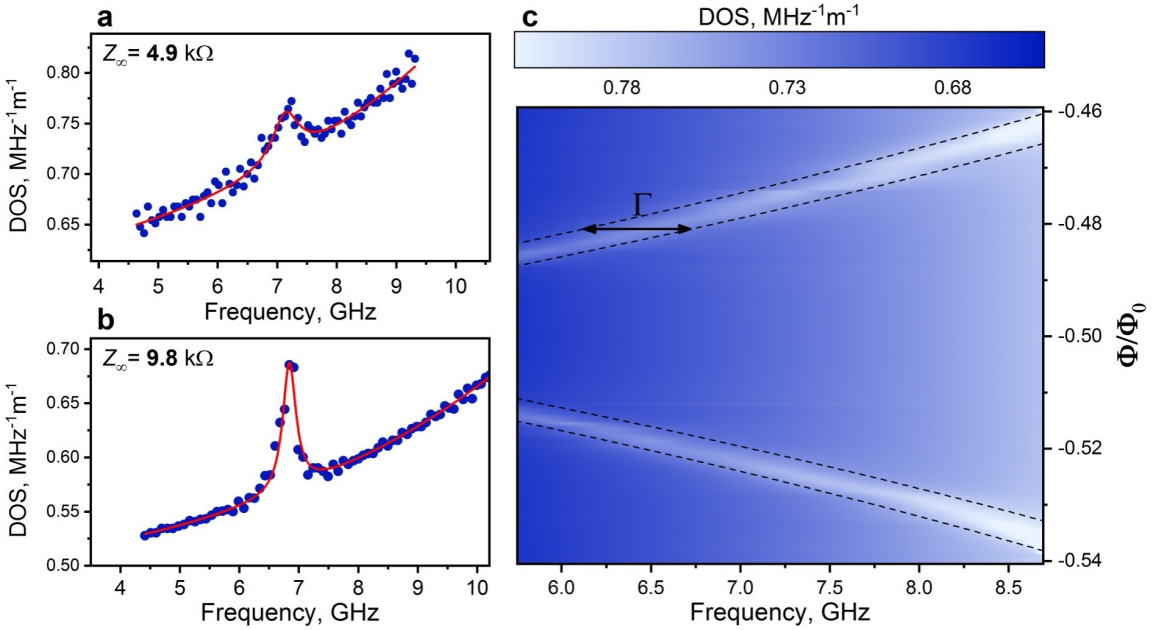

Figure 6.4: (a) Single-particle density of photon states (DOS) vs. frequency (see text). The fluctuations are reproducible and reflect a small disorder in the junction parameters. The fit (solid red line) is a combination of a Lorentzian resonance shape combined with the background transmission line DOS growing due to the van Hove singularity at the plasma frequency $\omega_p/2\pi = 22.6\,\mathrm{GHz}$. (b) DOS extracted for a device with $Z_\infty = 9.8\,\mathrm{k\Omega}$. (c) DOS as function of external flux threading the transmon SQuID loop. The two dashed lines indicate the fit to a transmon's transition and a fixed width of the DOS peak.

frequency range $0 - 15$ GHz are effectively decoupled from the transmon impurity. We use the one tone and two tone reflection spectroscopy data measured at $\varphi_{\rm ext} = 0$ to reconstruct the dispersion relation of the standing wave modes following procedure of chapter 4. We fit the dispersion of the modes to obtain the speed of light and the plasma cutoff of the cavity. The wave impedance of the cavity is estimated using the procedure detailed in section 4.3.3.

In order to characterize the properties of the impurity we perform spectroscopy as a function of flux through the transmon's SQuID loop as shown in Fig. 6.3. We observe a dense set of regularly spaced resonances, with a mode spacing of about $\Delta \approx 50$–60 MHz, which are disturbed periodically in flux (only a fraction of the period is shown). This flux-dependent disturbance is associated with the tuning of the transmon's resonance across the spectrum of the bare Fabry-Perot cavity. The unique feature of these data compared to previous multi-mode circuit experiments [23, 80] is that there are no individual vacuum Rabi splittings. In fact, at a fixed flux, the raw spectroscopy trace versus frequency contains no obvious sign of the transmon resonance (Fig. 6.3 (b)). However, upon tuning the flux, we observe that multiple resonances shift by nearly the same amount, indicating that many modes are equally sensitive to the tuning of the transmon (see three insets in Fig. 6.3).

A clear picture of an transmon simultaneously coupled to many Fabry-Perot comes from extracting the density of states (DOS) conventionally defined as $(\pi/\ell)/(\omega_{j+1} - \omega_j)$, where ω_j is the measured frequency of j^{th} mode. This quantity is readily available since every individual mode is frequency-resolved in our reflection spectroscopy. The obtained DOS has a broad peak, involving about 20 consecutive modes, and slowly increasing with frequency background (Fig. 6.4(a)). The peak line-shape fits well to a simple Lorentzian function with unit area, which correctly reflects one additional state coming from the transmon. The DOS peak position shifts with flux and perfectly follows the disconnected transmon's resonance, assuming a reasonable junction asymmetry and that the maximal plasma frequency is that of the other chain junctions (Fig. 6.4 (c)). Importantly, the fitted peak width is frequency-independent and matches the theoretical radiative linewidth $\Gamma = 1/2\pi Z_\infty C_J \approx 600$ MHz, within ± 50 MHz. In a control experiment, we have checked that a device with a twice higher wave impedance, $Z_\infty = 9.8$ kΩ, fabricated using a skinnier junction chain, narrows the DOS peak precisely by a factor of two (Fig. 6.4).

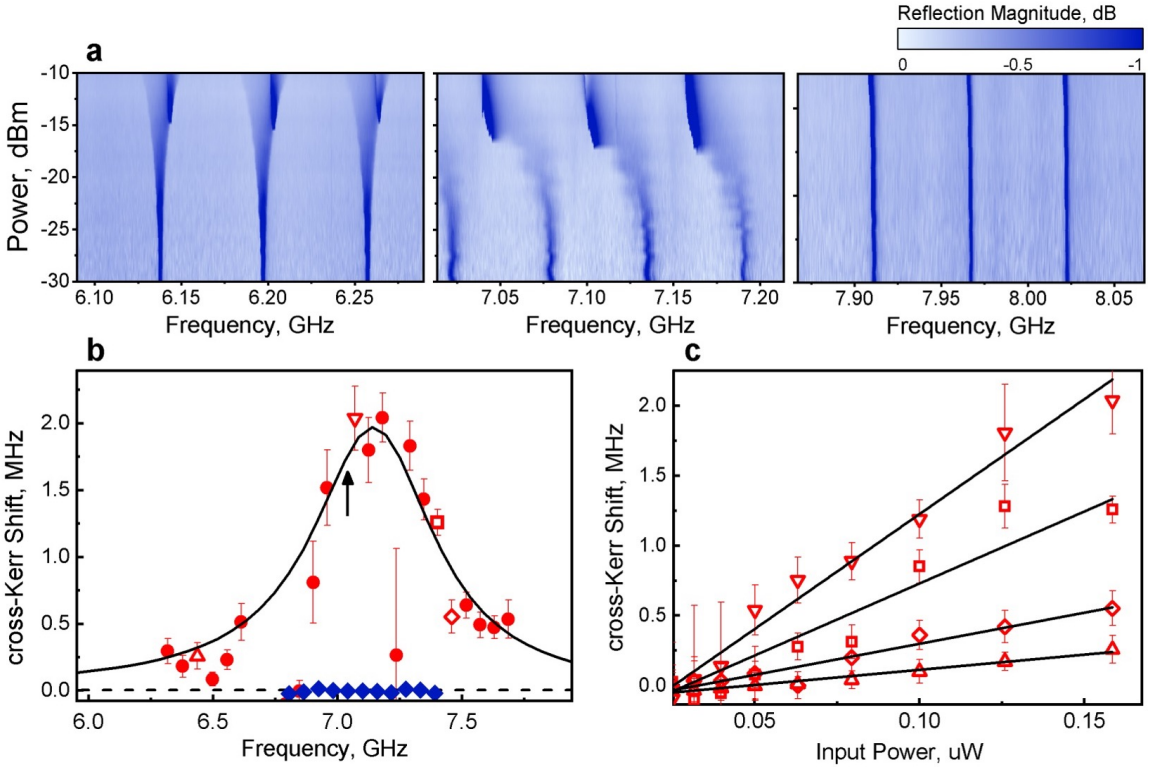

Figure 6.5: (a) Power-dependence of the spectroscopy signal for the DOS peak at 7.12 GHz. The modes inside the DOS peak shift more strongly with power than the ones outside. (b) Dispersive shifts $\chi_{i,j}$ as a function of i-modes frequencies for a fixed second-tone driving of the mode $j = 108$ at $7.014\,\mathrm{GHz}$, near the top of the DOS resonance (marked with an arrow). Blue markers indicate the same measurement for a largely detuned atom. Theory (solid and dashed lines) has no adjustable parameters except for the Y-axis scale (see section 6.5.1.2). The error bars are the standard deviations of the measured dispersive shifts. (c) Power-dependence of the shifts of selected modes indicated by matching markers

6.5.1.2 Photon-photon interactions

To test the Hamiltonian (Eq. 6.6) further, we measure the transmon induced photon-photon interactions. We verified the presence of the induced self-Kerr effect in the normal modes of the device using high power spectroscopy. The modes inside the DOS peak clearly shift much more in response to a high-power driving compared to the modes outside of it (Fig. 6.5(a)). At some threshold power, we observe that the resonances within the DOS peak snap onto their uncoupled values. This effect, standard in circuit QED [81], can be explained as the SQuID split-junction effectively acquiring an infinite inductance because the swing of its over-driven phase exceeds 2π.

The cross-Kerr interaction can be characterized more accurately. For a chosen flux bias when the transmon resonance is tuned to $7.2\,\mathrm{GHz}$, we drive a mode $j = 108$, corresponding to the peak in the DOS at a convenient atomic frequency around $7\,\mathrm{GHz}$. The power is chosen such that the mode is populated by an approximately one photon on average. Reflection measurements are then performed on the neighboring modes $i = j \pm 1, j \pm 2, \ldots$ with a second low-power drive being consecutively on or off. The mode frequency in every measurement was found from the fit of the reflection coefficient to Eq 4.19. The shift is then defined as an average mode frequency change between the on and off state of the second tone. The procedure was repeated for various second-tone powers (see Fig. 6.5 (c)). To eliminate the detrimental effects of the flux jitter, we chose the shortest possible time between two consecutive measurements. Moreover, the frequency of the second tone was modulated with a time scale much smaller than the measurement time and with an amplitude larger than the jitter amplitude. This allowed us to create a constant population of the driving mode disregarding its frequency fluctuation. This procedure allowed us to measure the dependence of $\chi_{i,j}$ on i , j and compare it with our perturbative calculation. The $\chi_{i,j}$ is maximal for the DOS peak maximum, and drops rapidly as the i-modes leave the Γ-neighborhood of the transmon resonance. Although the measured shifts have some fluctuations of presently unknown nature, the overall data match the theory well using the photon number of the second drive tone as the only adjustable parameter.

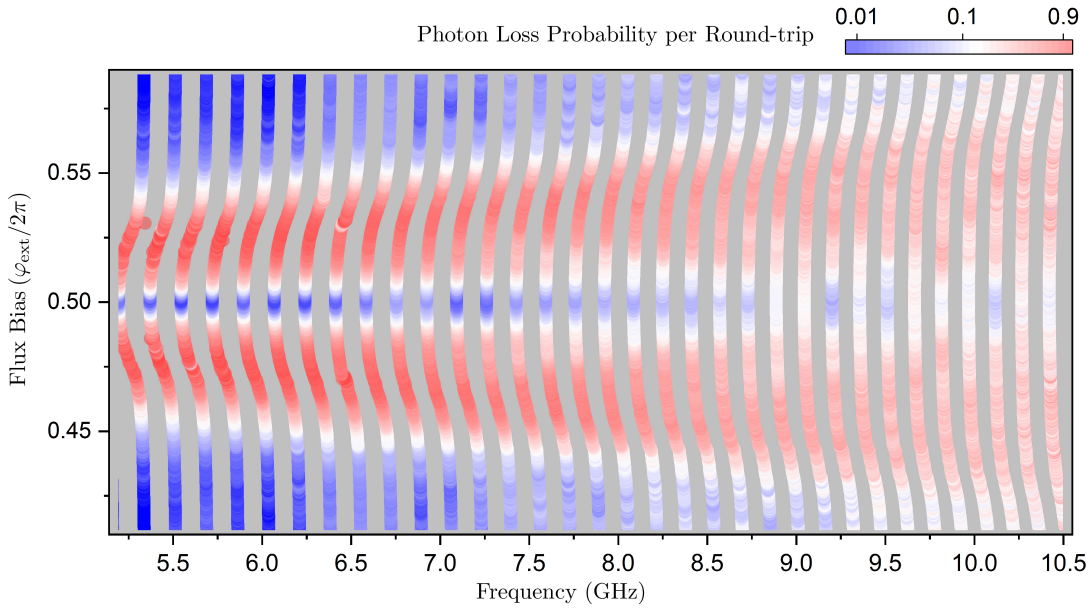

Figure 6.6: The measured positions of standing wave resonances as a function of flux through the split-junction loop in device 3a . The color shows probability to lose a single photon in one round-trip time.

6.5.2 Inelastic scattering of photon off phase-slip

In this section we describe measurements on devices where we progressively decrease the size of the transmon's SQuID junctions. This decreases the ratio of E_J/E_C of the transmon and increases the amplitude of the phase slips across its Josephson junction. To extract the parameters of the bare transmission line we follow the same procedure as the last section where we measure the standing wave resonances of the device when the reduced flux (φ_{ext}) threading the SQuID loop is set to an integer multiple of 2π. In order to extract the parameters of the transmon we measure the standing wave resonances of the cavity as a function of external flux threading the SQuID loop. We observe that multiple standing wave resonances of the cavity shift as a result of tuning the frequency of the transmon as expected. In addition, we also observe that the standing wave resonances acquire a larger linewidth when the transmon is in resonance with a given standing wave mode. This is in stark contrast to the splitting of the standing wave resonance observed in the case of a fluxonium impurity (see chapter 5).

The effect of the transmon impurity on the photons in the transmission line can be separated

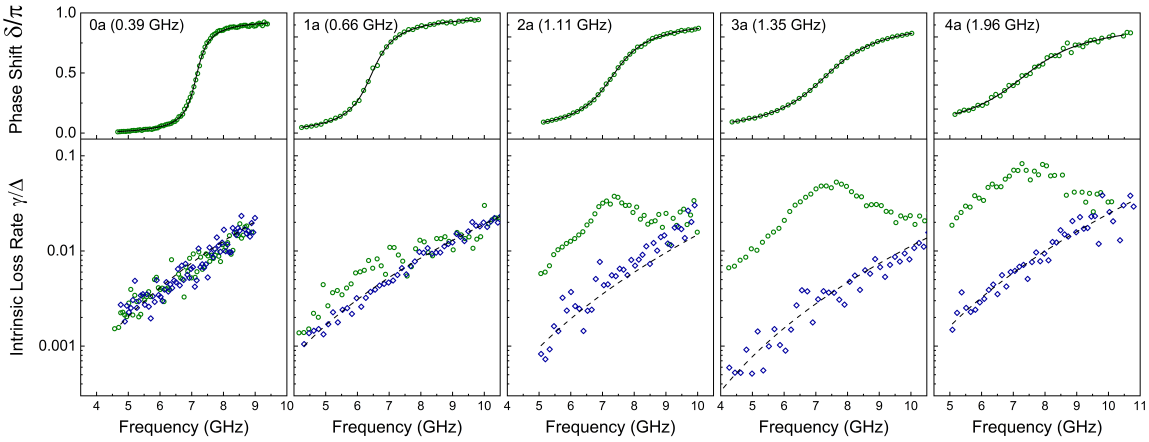

Figure 6.7: Measured elastic phase shift (top) and intristic loss rate (bottom) for devices with progressively larger charging energy E_C indicated on the plots. In each device, the external flux bias φ_{ext} is tuned such that $\omega_{\text{eg}}/2\pi \approx 6.5$–$7.5$ GHz. The blue markers show data at $\varphi_{\text{ext}} = 0$, where the impurity is effectively switched off. The dashed line represents the background dielectric loss inside the transmission line. Device parameters are given in Table 6.1.

into two parts. The first part is the elastic scattering effect where all the photons in the transmission line reflect from the transmon boundary with a phase shift $\delta(\omega)$ depending on the frequency of the incoming photons. This effect results in the shift in the standing wave mode frequencies of the Fabry-Perot cavity described in the last section. This shift can also be thought of as the result of hybridization of the transmon resonance with the bare resonances of the transmission line as described in Eq. 6.10. The shift $\delta(\omega)$ can be completely characterized by comparing the frequencies of the hybridized standing wave modes of the cavity with the bare standing wave modes of the cavity when the transmon is maximally detuned ($\varphi_{\text{ext}} = 0, 2\pi$) by the following formula:

$$\delta(\omega_k(\varphi_{\text{ext}})) = \frac{\omega_k(\varphi_{\text{ext}} = 0) - \omega_k(\varphi_{\text{ext}})}{\omega_{k+1}(\varphi_{\text{ext}} = 0) - \omega_k(\varphi_{\text{ext}} = 0)}, \tag{6.14}$$

where $\omega_k(\varphi_{\text{ext}})$ are the normal modes of the Fabry-Perot cavity at a given flux bias and $\omega_k(\varphi_{\text{ext}} = 0)$ are the bare Fabry-Perot cavity modes.

The second part is the inelastic scattering effect where a photon in mode k upon reflection from the transmon boundary down-converts from a given standing wave mode into odd number of photons in lower frequency modes. This effect is due to the interaction induced by the transmon described by the interaction Hamiltonian in Eq. 6.3.2. This interaction can be thought of as the

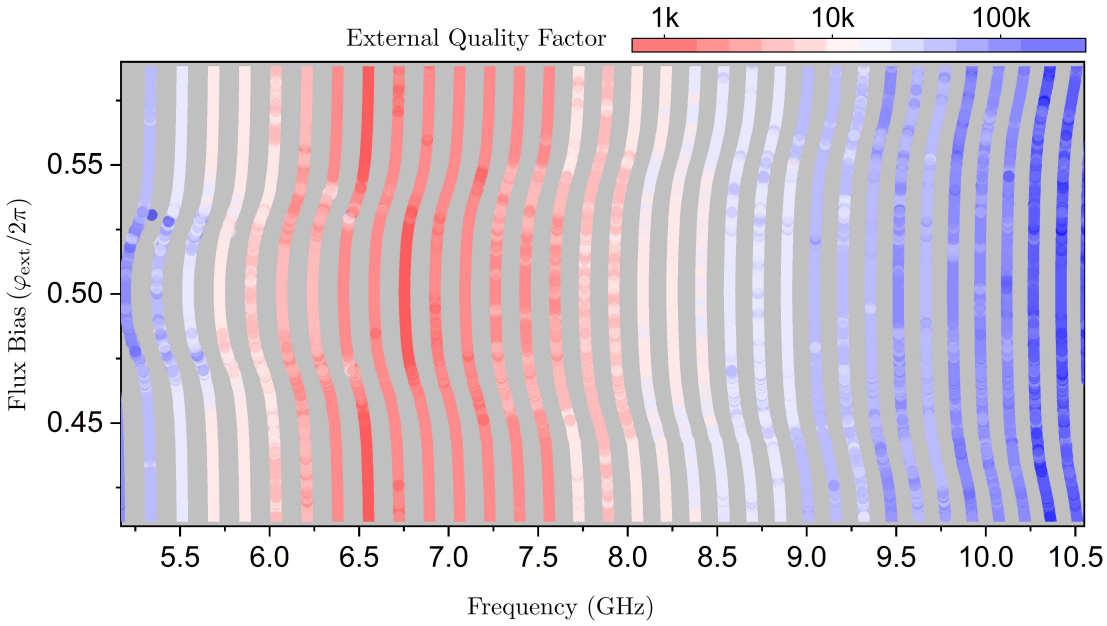

Figure 6.8: External quality factors as a function of frequency and external flux for device 3a. The strong frequency dependence of the Q_{ext} towards the lower frequencies is the result of the propagation cut-off of our copper waveguide at 7 GHz.

interaction between a single-particle state in standing wave mode k with many-particle states with one excitation in mode close to k and an even number of excitations in low frequency modes. As long as the many-body level spacing of all possible final states that a single photon can down convert into is smaller than the scattering rate into them, then this process looks like there is an intrinsic absorption mechanism for this mode. In this limit we can calculate the decay rate of each standing wave mode using the Fermi's golden rule [82]. The end result of this decay is the broadening of the standing wave modes of the Fabry-Perot cavity.

To characterize the effect of the transmon we perform reflection spectroscopy of the standing wave modes of our effective Fabry-Perot cavity as a function of the magnetic flux threading the SQuID loop of the transmon. As noted in the previous chapters these spectroscopy experiments are performed while populating the modes with less than one photon on average, and we checked that the spectroscopy response remained power independent. By fitting the reflection spectroscopy data near each resonance with Eq. 4.19, we were able to extract precisely the excitation frequency and the quality factors of each of the standing wave modes of the effective Fabry-Perot cavity. This allows

us to extract the elastic phase shift and the intrinsic loss rate of each of the standing wave modes. The elastic phase shift $\delta(\omega)$ expectedly winds by π across the transmon's resonance. Fitting this shift with the standard formula for an oscillator we also extract Γ, the spontaneous emission linewidth of the transmon. We check that this quantity remains independent of the transmon frequency. The loss rate in each standing wave mode is flux independent in device 0a with $E_C = 0.39$ GHz, and it can be explained by the background dielectric absorption in our bare Fabry-Perot cavity (see section 4.3.1). However, already for $E_C = 0.66$ GHz in device 1a, there is a noticeable deviation of $\gamma(\omega)$ from the background at $\varphi_{\rm ext} = 0$, and this deviation rapidly grows with E_C (Fig. 6.7, lower panels). The anomalous dissipation is maximal for modes located in the Γ-vicinity of the transmon resonance at $\omega_{\rm eg}$, defined in Fig. 6.7 as $\delta(\omega) = \pi/2$.

Subtracting the background loss of each device from $\gamma(\omega)$, we interpret the remaining rate $\gamma_{\rm in}(\omega)$ as the rate of photon decay due to inelastic scattering at the impurity. Several properties of $\gamma_{\rm in}$ support our interpretation. The maximal decay rate $\gamma_{\rm in}(\omega = \omega_{\rm eg})$ grows by an order of magnitude on reducing $\omega_{\rm eg}$ by only a few GHz. Such a strong frequency dependence of $\gamma_{\rm in}(\omega = \omega_{\rm eg})$ eliminates the possibility of mundane absorption due to either a lossy dielectric or quasiparticle tunneling in the impurity junction (see section 6.6). In fact, the growth of $\gamma_{\rm in}(\omega_{\rm eg})$ at lower frequencies is atypical to materials loss (see section 6.6). Furthermore, the rate $\gamma_{\rm in}(\omega_{\rm eg})$ vanishes in device 0a, which features the fastest variation of mode frequency with $\omega_{\rm eg}$ [the sharpest function $\delta(\omega)$ near $\omega = \omega_{\rm eg}$ in Fig. 6.7]. Such an observation eliminates inhomogeneous broadening mechanism due to slow fluctuations of ω_{eg} in time. We have also explicitly measured the external quality and checked that the measured port coupling is insensitive to flux bias, and γ_{in} is insensitive to increasing the port coupling (see Fig. 6.8).

Within the experimental uncertainty on model parameters, Fermi's golden rule decay calculations matches the data from all four devices with $Z_\infty > R_Q$ without adjustable parameters (see Fig. 6.9) [82, 83]. Either increasing E_C or reducing $\omega_{\rm eg}$ with the flux knob exponentially increases ν, which in turn causes a rapid growth of $\gamma_{\rm in}(\omega_{\rm eg})$. The effect of impedance is weaker but more complex. In particular, our analysis breaks down for $Z_\infty \to R_Q$, in which case photons are likely produced in the entire frequency range. Devices with $Z_\infty < R_Q$ exhibit similar, by order of magnitude, decay rates $\omega_{\rm eg}$, compared to those by devices with $Z_\infty > R_Q$ with similar values of E_C [Fig. 6.9 (left panel)

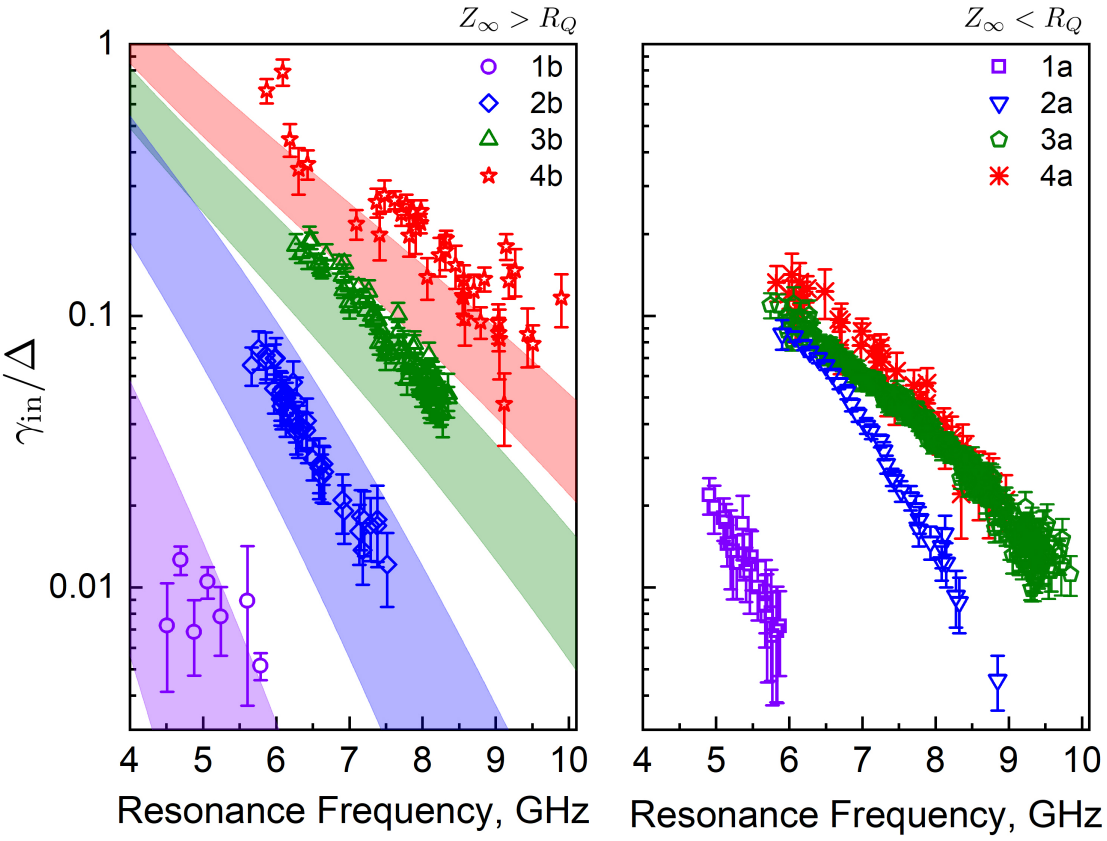

Figure 6.9: Inelastic scattering rate γ_{in}/Δ (colored markers) for devices with $Z_\infty > R_Q$ (left panel) and $Z_\infty < R_Q$ (right panel). The width of theory lines (colored bands) comes from uncertainty in the device parameters. The error bars are the standard errors of γ_{in}/Δ at the resonance. The color code represents nominally identical values of E_C.

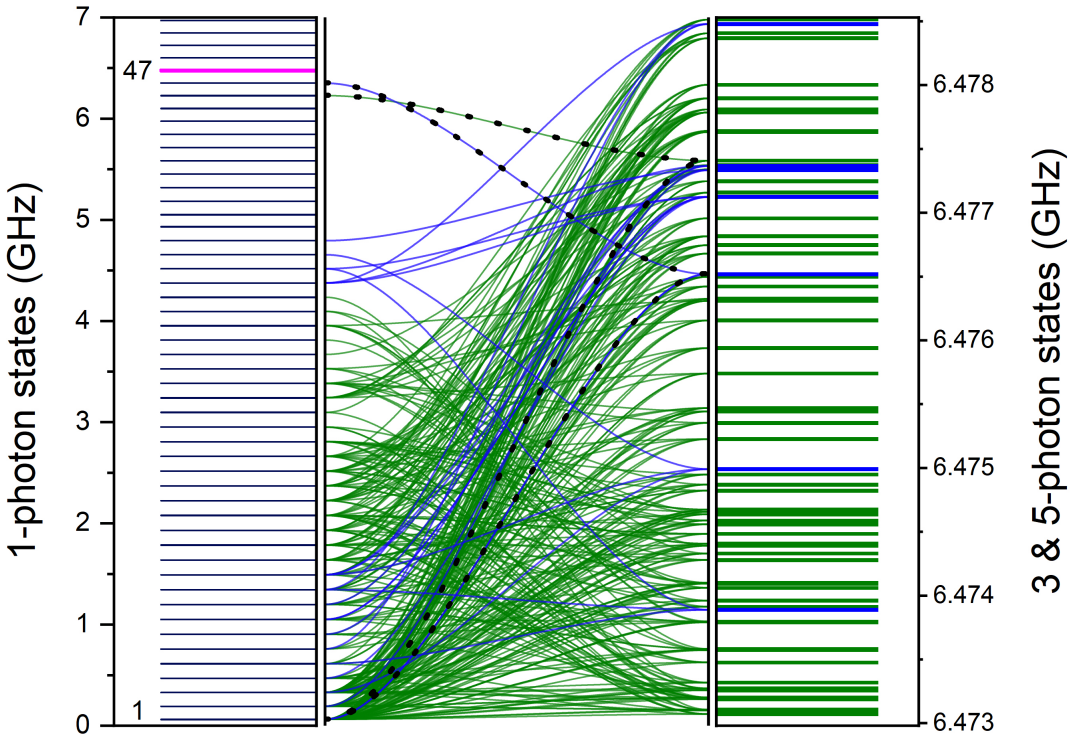

Figure 6.10: An example of the coupled many-body states satisfying energy conservation condition for the decay of the mode $k = 47$ in device 2a ($\omega_{\mathrm{eg}} = \omega_{47}$). The many-body spectrum (right) is obtained by summing all possible combinations of three (blue) and five (green) one-photon frequencies, measured experimentally (left). The frequency range in the right panel is equal to the measured half-linewidth of the $k = 47$ mode. The visualization in the central panel illustrates the composition of the multi-photon states from the measured one-photon spectrum. Note the most likely decay channels $\omega_{47} \to \omega_{46} + 2\omega_1$ and $\omega_{47} \to \omega_{45} + 4\omega_1$ involving the lowest frequency mode at $\omega_1/2\pi = 63\,\mathrm{MHz}$ are highlighted with dotted lines.

vs (right panel)]. However, a quantitative comparison in case $Z_\infty < R_Q$ requires more advanced theoretical models than those presently available at the time of writing of this thesis.

The reason for the observation of the increased linewidth of the standing wave modes instead of discrete many-body resonances as observed in chapter 5 is the delocalization of a single excitation state in the many-body Fock space. Let us illustrate the large number of decay channels available for a single photon, using an example of mode 47 in device 2a. The flux $\varphi_{\rm ext}$ is tuned such that $\omega_{\rm eg}/2\pi \approx \omega_{47}/2\pi \approx 6.476\,{\rm GHz}$, and the measured mode linewidth $\gamma_{47} = 11\,{\rm MHz}$. Using extended spectroscopy data (Fig. 6.10, left panel), we identified those three-photon and five-photon combinations, whose energy matches $\hbar\omega_{47}/2\pi$ within the half-linewidth $h \times 5.5$ MHz. This construction reveals a large number of states with a relatively uniform three-photon [$\Delta^{(3)}1{\rm MHz}$, Fig. 6.10, blue states] and five-photon [$\Delta^{(5)}50$ kHz, Fig. 6.10, green states] level spacing. Final states involving higher number of photons are also available and they would form even denser spectrum. We checked that most three-photon states with energies $(\omega_i + \omega_j + \omega_k)$ couple relatively uniformly, and same applies to five-photon states. The energy uniformity property comes from a small amount of disorder and dispersion in the single-particle spectrum (see chapter 4 section 4.3.2), which breaks the otherwise massive degeneracy of multi-photon states. These observations justify the treatment of our finite-size transmission line as an infinite one and apply Fermi's golden rule to calculate the lifetime of the standing wave modes.

6.6 Comparison to material related losses

As was already mentioned earlier, the observed inelastic rate and its behavior are inconsistent with the material-related loss mechanisms. To make this point more clear, Fig. 6.11 compares the measured $\gamma_{\rm in}/\Delta$ to the predictions for the dielectric loss and quasiparticles induced loss. To make such a comparison, we modeled the dissipation as a resistor R_s connected to the end of the transmission line, in parallel with the transmon. The value of R_s at a frequency ω_s can be found by matching the model predictions to the observed inelastic rate at this frequency. By assuming that the resistance comes either from the dielectric $R_s = 1/(\omega_s C_J \tan\delta)$, or from quasiparticle tunneling

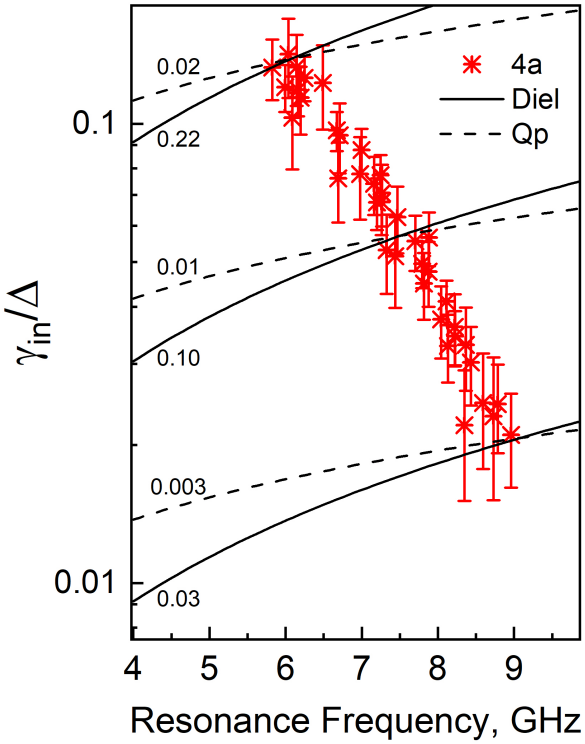

Figure 6.11: γ_{in}/Δ at resonance with the transmon as a fuction of the transmon frequency (star markers) and predictions for the dielectric (solid line) and quasiparticle induced loss (dashed line) in the transmon junction. Numbers on the lines indicate the values of loss tangent $\tan\delta$ and quasiparticle density x_{qp}.

$R_s = R_Q/(2x_{qp})EC/\sqrt{2\Delta_{sc}\omega_s}$, we can estimate the dielectric loss tangent $\tan\delta$ and the quasiparticle density x_{qp}. Δ_{sc} is the superconducting gap of aluminum. We see in Fig. 6.11, that both mechanisms demonstrate a frequency dependence opposite to the observed one. Moreover, the inelastic rate around $7.4\,\mathrm{GHz}$ translates to loss tangent $\tan\Delta \approx 0.1$ or quasiparticle density $x_{qp} \approx 0.01$. Matching the data to the material-related loss at lower frequencies will result in even higher $\tan\delta$ and x_{qp}. Such numbers are unrealistically high, taking into account the fact that the same junctions and a similar RF setup are used in fabrication and measurements of high-coherence qubits [68] [69].

6.7 Conclusion

In summary, we engineered a multi-mode circuit QED setup in the quantum impurity regime where the transmon impurity induces interaction between all odd-order multi-photon states. This interaction can split a single incident photon into a large number of lower-energy photons with probability near unity. Inserting such an efficient inelastic scattering center inside a closed Fabry Perot resonator makes the photon lifetime comparable to the round-trip time, in which case the standing-wave resonances are damped by the photon-photon interaction to the degree prohibiting the use of free-photon description of the quantum electromagnetic field in the resonator.

6.8 Summary of device parameters

Device	$v/10^6(\mathrm{m/s})$	$\omega_p/2\pi(\mathrm{GHz})$	$Z_\infty(\mathrm{k\Omega})$	$\Delta(\mathrm{MHz})$	$\Gamma(\mathrm{GHz})$	$E_C(\mathrm{GHz})$
0a	1.65	22.6	5.36 ± 0.67	137	0.6 ± 0.02	0.39 ± 0.05
1a	1.93	23.0	5.26 ± 0.4	161	1.03 ± 0.03	0.66 ± 0.05
2a	1.78	22.5	5.36 ± 0.05	149	1.70 ± 0.02	1.11 ± 0.01
3a	2.25	27.3	4.44 ± 0.24	188	2.50 ± 0.04	1.35 ± 0.08
4a	1.89	23.2	5.22 ± 0.21	158	3.10 ± 0.09	1.96 ± 0.1
0b	1.99	24.5	9.82 ± 0.04	166	0.32 ± 0.03	0.38 ± 0.03
1b	2.32	26.2	9.25 ± 1.16	194	0.66 ± 0.02	0.74 ± 0.10
2b	1.37	17.5	13.61 ± 0.92	114	0.63 ± 0.02	1.05 ± 0.08
3b	1.75	22.0	10.89 ± 0.42	146	1.18 ± 0.04	1.56 ± 0.08
4b	1.72	21.0	11.38 ± 0.01	143	1.32 ± 0.07	1.83 ± 0.1

Table 6.1: Device parameters extracted by performing characterization experiments detailed in section 6.5. Note that the length of all the devices presented in this table was $6\,\mathrm{mm}$, except for Devices 0a and 0b which were twice longer.

Chapter 7

Summary and Outlook

7.1 Summary of Results

In this thesis, we presented a series of experiments where we engineered the quantum regime of cavity quantum electrodynamics. We achieved this by coupling superconducting Josephson atoms to a multi-mode Fabry-Perot cavity. By leveraging the high kinetic inductance of electrons and galvanic coupling we were able to enter a regime of light-matter interaction where a single atom interacts with multiple modes of the cavity simultaneously. In this regime we found that the decay of a single photon becomes a problem of many-body physics as the atom acting as an impurity mediates interactions between many-body states of radiation. In particular we experimentally implemented this regime for the case of two different impurity atoms.

In the first experiment we coupled a fluxonium artificial atom to the cavity. In this case our experiments revealed that the atom mediates a three-wave mixing interactions between the modes of the multi-mode cavity. This interaction attempts to down convert a single excitation in a high frequency mode of the cavity into lower frequency excitations but fails due to lack of connectivity in the many-body Fock space. Many-body localization of photons manifests itself as the violation of Fermi's golden rule and the splitting of the standing wave resonance into discrete well resolved peaks due to the coherent hybridization of many-body states of radiation with a single particle state. We directly measure this spectrum of many-body states of radiation and identify each peak with its

wavefunction composed of a specific many-body content.

In the second experiment we coupled a transmon artificial atom to the cavity. In this case we found that for large E_J/E_C the main effect of the transmon on the standing wave modes of the cavity was a frequency dependent phase shift. The photon-photon interactions were suppressed because of the transmon's weak anharmonicity. However, we observed that by decreasing the E_J/E_C of the transmon turns on another kind of non-linearity that of phase slips across the small junction of the transmon. In addition, we also observed that this non-linearity induces interactions between all many-body states of radiation of odd parity which splits a single photon excitation into a large number of lower frequency photons. In stark contrast with the case of the fluxonium impurity here, the single excitation diffuses into the many-body Fock space and the only measurable consequence of this effect is an increased linewidth of the standing wave modes of the Fabry-Perot cavity.

7.2 Tunable platform to study MBL physics in 1-D

Our experiments puts forward multi-mode circuit quantum electrodynamics as a possibly useful experimental platform to further explore fundamentals of MBL. In comparison to spin chains or lattice fermions, here the frequency space takes the role of the real space, the number of participating degrees of freedom is set by the excitation frequency, and the connectivity of the many-body Fock space can be tailored by varying the properties of the qubit circuit, serving as one of the cavity mirrors. In the experiments presented in this thesis, we implemented a local tree-like connectivity by harnessing the inversion symmetry breaking and the strong anharmonicity properties of fluxoniums. At the opposite extreme we also engineered a quantum phase-slip impurity, which can maximize the Fock-space connectivity, in which case the down-conversion rate indeed accurately obeys the Fermi's Golden Rule [84]. In future experiments, the disorder can be tailored via nanofabrication, the interaction can be quenched by rapidly tuning the flux knob, and multi-mode tomography techniques, developed for bosonic qubits [85], can be applied here to monitor the entanglement dynamics in the time-domain.

In addition, future experiments can probe the cross-over of our system from many-body localized to de-localized regime. One proposal to implement this could be by adding a tunable boundary

condition to the left end of the device discussed in chapter 5. To understand this lets consider the spectrum of many-body states near a single particle state $k \gg 1$. For the case of an open boundary condition on the other end of the impurity will result in a spectrum where the n and $n+1$ particle subspaces will be maximally detuned which would result in the localization of a single particle excitation state similar to the case described in detail in chapter 5. However, for the case of a short boundary at the other end of the impurity will result in all n and $n+1$ particle states to be in resonance, this will result in de-localization. The ability to tune this boundary condition in situ via a large area SQuID can implement this transition in a single device.

7.3 Implementation of Q-RAM

The devices presented in chapters 5 and 6 also have a direct application for the purposes of quantum information processing. In particular, the small mode volumes and high quality factors make the standing wave modes in the Josephson junction transmission line ideal as quantum memories. In addition, by coupling the transmon and fluxonium qubits in the strong dispersive regime, all to all interactions can be induced between the memory modes by applying off-resonant drives on the qubits [86]. In comparison to existing proposals that involve directly exciting the qubit, this scheme can offer a substantial improvement in gate fidelity. The ability to engineer mode frequencies via nano-fabrication to obtain non-uniform mode spacing also makes this platform attractive for practical proposes.

The experimental realization of quantum information processing using multi-mode cQED has the potential to solve two of the most pressing challenges in continuous variable quantum computation namely scaling and slow gate speeds. The all to all connectivity in this architecture also paves the way to realize quantum random access memories which is a prerequisite in important quantum algorithms like the Grover's search [87].

Appendices

Appendix A

Benchmnarking

In this appendix we benchmark the effective Hamiltonian and the procedure to calculate the eigen-spectrum for a multi-mode cavity QED system described in chapter 5 in Eq. (5.12) in the mixed gauge, against brute-force diagonalization for finite-size systems.A full numerical diagonalization of the Hamiltonian in Eq. (2.49) rapidly becomes a daunting task, because the Hilbert space size grows exponentially with the number N of bosonic modes and the number of photons involved. Here we present results for a system with $N = 6$ bosonic modes. Moreover, we also report results in the other two gauges (charge and flux gauge) including multiple fluxonium levels and show that the same results can be obtained by approximating the fluxonium as a two-level system in the mixed gauge.

In our numerical calculations, we consider a fluxonium atom described by the parameters $E_J = 8.12$ GHz, $E_C = 5.69$ GHz, $E_L = 1.42$ GHz. For the cavity resonator, we consider a two-wire transmission line with parameters $Z_\infty = 9865\,\mathrm{k}\Omega, v = 2.18 \times 10^6\,\mathrm{m/s}, \ell = 300\,\mu\mathrm{m}$. In this example the line shares a fraction $x = 0.2$ of the inductance with the fluxonium. The unequal spacing of the modes in the transmission line is achieved simply by introducing the ultra-violet cutoff due to the plasma frequency ω_p for wave propagation in the transmission line. The unequal mode spacing breaks the degeneracy of different multi-photon states and isolate anti-crossings between any two given states in the many-body spectrum of the system.

Note that we have also derived the circuit Hamiltonian of the system in both the flux and the

charge gauges following the procedure described in section 2.4.2. We have diagonalized the circuit Hamiltonian in both gauges using the lowest 40 levels of the uncoupled photonic modes of the transmission line and the 7 lowest-energy levels of the fluxonium. In Fig. A.1 (a), we report the energy eigenvalues in such two gauges with the prediction of the effective Hamiltonian (mixed gauge, two-level approximation for the fluxonium). The excellent agreement between the three gauges in Fig A.1 (a)) not only illustrates the gauge invariance of our multi-mode cQED model, but also serves as the additional proof that we have used a large enough Hilbert space in diagonalizing the Hamiltonian. In particular, it also validates the two-level approximation for the fluxonium in the mixed gauge. A zoom in of the eigenspectrum plot near the vacuum Rabi splitting of the third photonic mode reveals an additional anti-crossing. This anti-crossing can be explained as the spectral manifestation of the hybridization between the single-particle state $\hat{a}_4^\dagger|G\rangle$ and the two-photon state with one excitation in polariton mode $k=3$ and one excitation in mode $k=1$, namely the state $\hat{a}_3^\dagger\hat{a}_1^\dagger|G\rangle$. To reproduce these spectral features with the effective Hamiltonian derived in section 5.3, first we diagonalize the Hamiltonian only in the single-excitation subspace, where we ignore the coupling of the fluxonium to the lowest transmission line mode, and obtain the polaritonic frequencies ω_k for $k>1$. Then we include the effect of the coupling of the lowest mode by expanding the Hilbert space to include the two-photon and three-photon states. We finally calculate the spectrum by diagonalizing the following 7×7 matrix:

$$H_{\text{eff}} = \tag{A.1}$$

$$\begin{pmatrix}
\Omega_3/2\pi & 0 & 0 & g_1^{(m,f)}A_{3,3} & g_1^{(m,f)}A_{3,4} & 0 & 0 \\
0 & \Omega_4/2\pi & 0 & g_1^{(m,f)}A_{4,3} & g_1^{(m,f)}A_{4,4} & 0 & 0 \\
0 & 0 & \Omega_5/2\pi & g_1^{(m,f)}A_{5,3} & g_1^{(m,f)}A_{5,4} & 0 & 0 \\
g_1^{(m,f)}A_{3,3} & g_1^{(m,f)}A_{3,4} & g_1^{(m,f)}A_{3,5} & \Omega_3/2\pi+\omega_1/2\pi & 0 & \sqrt{2}g_1^{(m,f)}A_{3,2} & \sqrt{2}g_1^{(m,f)}A_{3,3} \\
g_1^{(m,f)}A_{4,3} & g_1^{(m,f)}A_{4,4} & g_1^{(m,f)}A_{4,5} & \Omega_4/2\pi+\omega_1/2\pi & 0 & \sqrt{2}g_1^{(m,f)}A_{4,2} & \sqrt{2}g_1^{(m,f)}A_{4,3} \\
0 & 0 & 0 & \sqrt{2}g_1^{(m,f)}A_{2,3} & \sqrt{2}g_1^{(m,f)}A_{2,4} & \Omega_2/2\pi+2\times\omega_1/2\pi & 0 \\
0 & 0 & 0 & \sqrt{2}g_1^{(m,f)}A_{3,3} & \sqrt{2}g_1^{(m,f)}A_{3,4} & 0 & \Omega_3/2\pi+2\times\omega_1/2\pi
\end{pmatrix}$$

. (A.2)

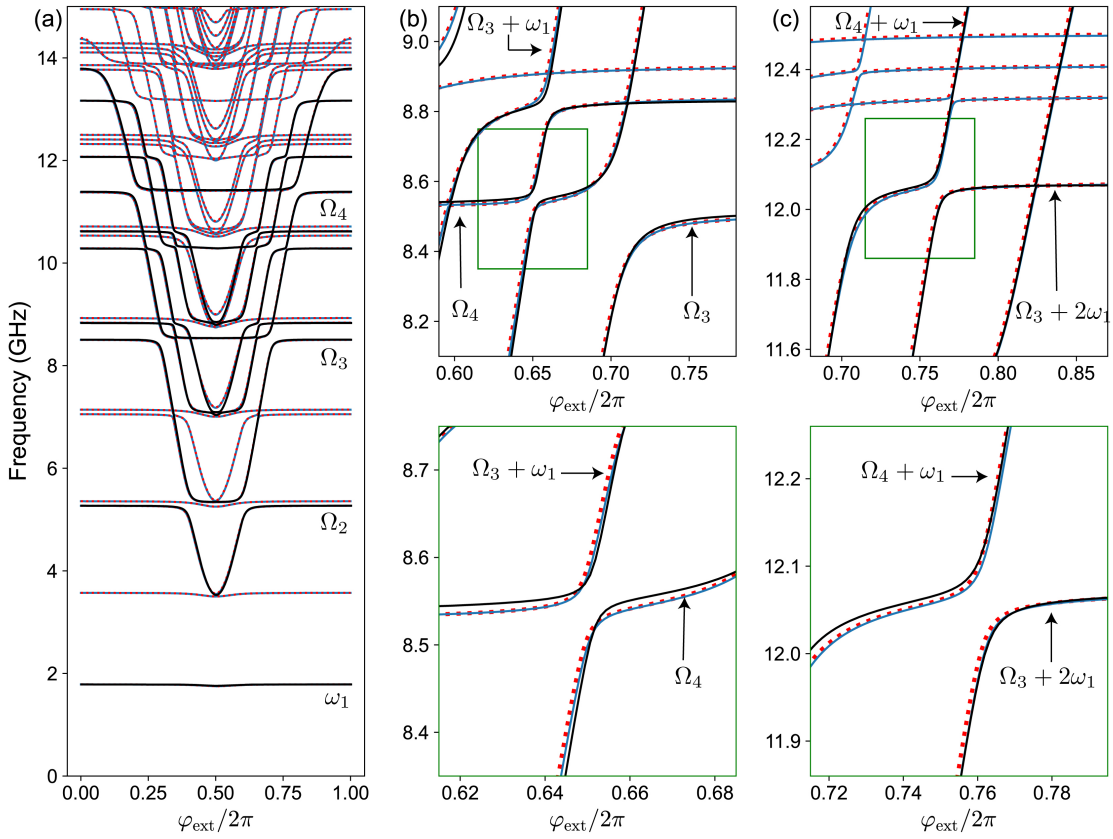

Figure A.1: (a) Excitation spectrum of the multi-mode circuit QED system (parameters of cavity and fluxonium in the text) for $N = 6$ unequally spaced modes obtained by numerical diagonalization in the charge (red dotted lines) and flux (solid blue lines) gauge. These results have been obtained by including the 7 lowest-energy fluxonium eigenstates. The spectrum obtained with the effective Hamiltonian 5.12 in the mixed gauge is displayed by the solid black lines. Note that the curves in the three gauges excellently overlap. (b) Zoom in of the spectrum near the anticrossing of mode $k = 3$ with the bare $|\mathrm{e}\rangle \rightarrow |\mathrm{g}\rangle$ transition, showing hybridization between the two-photon state with frequency $(\Omega_3 + \omega_1)$ and a single-polariton state with frequency Ω_4. The red dotted line is the result in the charge gauge with 7 levels, while the black solid line shows the energy levels calculated using the effective Hamiltonian described in Eq. (5.12) (mixed gauge, two-level approximation for the fluxonium). (c) Same as in (b), but this time showing the anti-crossing between the two-photon state with frequency $(\Omega_4 + \omega_1)$ and the three-photon state with frequency $(\Omega_3 + 2\omega_1)$.

The red dashed line in Fig. A.1 (b,c) shows the corresponding results, which are in excellent agreement with the full numerical diagonalization result. The figure shows the anticrossing due to the hybridization between the single-polariton state $\hat{a}_4^\dagger|G\rangle$ and the two-photon state consisting

of one excitation in polariton mode $k = 3$ and one excitation in the low-frequency mode $k = 1$, namely $\hat{a}_3^\dagger \hat{a}_1^\dagger |G\rangle$. The results display also an anticrossing between the two-photon state $\hat{a}_4^\dagger \hat{a}_1^\dagger |G\rangle$ and three-photon state $\hat{a}_3^\dagger (\hat{a}_1^\dagger)^2 |G\rangle$.

Appendix B

Calculation of the reflection coefficient

In this appendix we summarize the procedure to theoretically generate the refection spectra of the multi-mode cavity QED device presented in chapter 5. In order to theoretically calculate the linear microwave reflection spectra, we first consider the expression for the bare transmission line modes:

$$S_{11}(f) = \prod_{i=1}^{N} \frac{2\mathrm{i}\left(\frac{f-f_i^{(\mathrm{bare})}}{f_i^{(\mathrm{bare})}}\right) - \frac{1}{Q_i^{\mathrm{ext}}} + \frac{1}{Q_i^{\mathrm{int}}}}{2\mathrm{i}\left(\frac{f-f_i^{(\mathrm{bare})}}{f_i^{(\mathrm{bare})}}\right) + \frac{1}{Q_i^{\mathrm{ext}}} + \frac{1}{Q_i^{\mathrm{int}}}}, \tag{B.1}$$

where Q_i^{int} and Q_i^{ext} are respectively the internal and external quality factors of the bare transmission line modes. To calculate the reflection coefficient in the presence of the qubit, the expression is replaced by the product over the many-body eigenstates of the effective Hamiltonian in Eq. 5.12 of the main text:

$$S_{11}(f) = \prod_{i=1}^{N^{(s)}} \frac{2\mathrm{i}\left(\frac{f-f_i^{(\mathrm{many-body})}}{f_i^{(\mathrm{many-body})}}\right) - \frac{1}{\tilde{Q}_i^{\mathrm{ext}}} + \frac{1}{\tilde{Q}_i^{\mathrm{int}}}}{2\mathrm{i}\left(\frac{f-f_i^{(\mathrm{many-body})}}{f_i^{(\mathrm{many-body})}}\right) + \frac{1}{\tilde{Q}_i^{\mathrm{ext}}} + \frac{1}{\tilde{Q}_i^{\mathrm{int}}}}, \tag{B.2}$$

where $f_i^{(\mathrm{many-body})}$ are the excitation frequencies (with respect to the ground state) with corresponding eigenfunctions $|\Psi_i\rangle$ and $N^{(s)}$ are the total number of eigenstates of the Hamiltonian in the s-particle Hilbert subspace. Note that the external ($\tilde{Q}_i^{\mathrm{ext}}$) and internal ($\tilde{Q}_i^{\mathrm{int}}$) quality factors of the

the many-body states depend on the single-particle weight in the many-body eigenstate. This can be calculated by weighing the eigenstate quality factors with their single-particle fractions, namely:

$$(\tilde{Q}_i^{\mathrm{int(ext)}})^{-1} = \sum_{k>i_0} |\langle \Psi_i | \hat{a}_k^\dagger | 0 \rangle|^2 (Q'^{\mathrm{int(ext)}}_k)^{-1} \,. \tag{B.3}$$

Here the single-particle quality factors depend on the bare transmission line mode quality factors given by:

$$(Q'^{\mathrm{int(ext)}}_k)^{-1} = \sum_{i>i_0} |W_{k,i}|^2 (Q_i^{\mathrm{int(ext)}})^{-1} \,. \tag{B.4}$$

Bibliography

[1] Richard P. Feynman. *Quantum Electrodynamics*. New Edition, Westview Press, 03 1998.

[2] Peter W. Milonni. *The Quantum Vacuum*. Academic Press, 10 1994.

[3] Claude Cohen-Tannoudji, Jacques Dupont-Roc, and Gilbert Grynberg. *Photons and Atoms*. Wiley, 03 1997.

[4] Frank Arute, Kunal Arya, Ryan Babbush, Dave Bacon, Joseph C Bardin, Rami Barends, Rupak Biswas, Sergio Boixo, Fernando GSL Brandao, David A Buell, et al. Quantum supremacy using a programmable superconducting processor. *Nature*, 574(7779):505–510, 2019.

[5] Leonardo DiCarlo, Jerry M Chow, Jay M Gambetta, Lev S Bishop, Blake R Johnson, DI Schuster, J Majer, Alexandre Blais, Luigi Frunzio, SM Girvin, et al. Demonstration of two-qubit algorithms with a superconducting quantum processor. *Nature*, 460(7252):240–244, 2009.

[6] Serge Haroche and Jean-Michel Raimond. *Exploring the Quantum*. Oxford University Press, August 2006.

[7] Cristiano Ciuti, Gérald Bastard, and Iacopo Carusotto. Quantum vacuum properties of the intersubband cavity polariton field. *Phys. Rev. B*, 72:115303, Sep 2005.

[8] M.H. Devoret, Steven Girvin, and Robert Schoelkopf. Circuit-QED: How strong can the coupling between a josephson junction atom and a transmission line resonator be? *Annalen der Physik*, 16(10-11):767–779, oct 2007.

[9] J. Bourassa, J. M. Gambetta, A. A. Abdumalikov, O. Astafiev, Y. Nakamura, and A. Blais. Ultrastrong coupling regime of cavity qed with phase-biased flux qubits. *Phys. Rev. A*, 80:032109, Sep 2009.

[10] Vladimir E Manucharyan, Alexandre Baksic, and Cristiano Ciuti. Resilience of the quantum rabi model in circuit QED. *Journal of Physics A: Mathematical and Theoretical*, 50(29):294001, jun 2017.

[11] P. Forn-Díaz, L. Lamata, E. Rico, J. Kono, and E. Solano. Ultrastrong coupling regimes of light-matter interaction. *Rev. Mod. Phys.*, 91:025005, Jun 2019.

[12] Anton Frisk Kockum, Adam Miranowicz, Simone De Liberato, Salvatore Savasta, and Franco Nori. Ultrastrong coupling between light and matter. *Nature Reviews Physics*, 1(1):19–40, jan 2019.

[13] Francisco J. Garcia-Vidal, Cristiano Ciuti, and Thomas W. Ebbesen. Manipulating matter by strong coupling to vacuum fields. *Science*, 373(6551), July 2021.

[14] Y. Todorov, A. M. Andrews, R. Colombelli, S. De Liberato, C. Ciuti, P. Klang, G. Strasser, and C. Sirtori. Ultrastrong light-matter coupling regime with polariton dots. *Phys. Rev. Lett.*, 105:196402, Nov 2010.

[15] G. Scalari, C. Maissen, D. Turcinkova, D. Hagenmuller, S. De Liberato, C. Ciuti, C. Reichl, D. Schuh, W. Wegscheider, M. Beck, and J. Faist. Ultrastrong coupling of the cyclotron transition of a 2d electron gas to a THz metamaterial. *Science*, 335(6074):1323–1326, mar 2012.

[16] T. Niemczyk, F. Deppe, H. Huebl, E. P. Menzel, F. Hocke, M. J. Schwarz, J. J. Garcia-Ripoll, D. Zueco, T. Hümmer, E. Solano, A. Marx, and R. Gross. Circuit quantum electrodynamics in the ultrastrong-coupling regime. *Nature Physics*, 6(10):772–776, jul 2010.

[17] Fumiki Yoshihara, Tomoko Fuse, Sahel Ashhab, Kosuke Kakuyanagi, Shiro Saito, and Kouichi Semba. Superconducting qubit–oscillator circuit beyond the ultrastrong-coupling regime. *Nature Physics*, 13(1):44–47, oct 2016.

[18] D. Meiser and P. Meystre. Superstrong coupling regime of cavity quantum electrodynamics. *Phys. Rev. A*, 74:065801, Dec 2006.

[19] Mario F. Gely, Adrian Parra-Rodriguez, Daniel Bothner, Ya. M. Blanter, Sal J. Bosman, Enrique Solano, and Gary A. Steele. Convergence of the multimode quantum rabi model of circuit quantum electrodynamics. *Phys. Rev. B*, 95:245115, Jun 2017.

[20] Roman Kuzmin, Nitish Mehta, Nicholas Grabon, Raymond Mencia, and Vladimir E. Manucharyan. Superstrong coupling in circuit quantum electrodynamics. *npj Quantum Information*, 5(1), feb 2019.

[21] Javier Puertas Martínez, Sébastien Léger, Nicolas Gheeraert, Rémy Dassonneville, Luca Planat, Farshad Foroughi, Yuriy Krupko, Olivier Buisson, Cécile Naud, Wiebke Hasch-Guichard, Serge Florens, Izak Snyman, and Nicolas Roch. A tunable josephson platform to explore many-body quantum optics in circuit-QED. *npj Quantum Information*, 5(1), feb 2019.

[22] J. J. Hopfield. Theory of the contribution of excitons to the complex dielectric constant of crystals. *Phys. Rev.*, 112:1555–1567, Dec 1958.

[23] Neereja M. Sundaresan, Yanbing Liu, Darius Sadri, László J. Szőcs, Devin L. Underwood, Moein Malekakhlagh, Hakan E. Türeci, and Andrew A. Houck. Beyond strong coupling in a multimode cavity. *Phys. Rev. X*, 5:021035, Jun 2015.

[24] Steven M. Girvin and Kun Yang. *Modern Condensed Matter Physics*. Cambridge University Press, 02 2019.

[25] Leo Kouwenhoven and Leonid Glazman. Revival of the kondo effect. *Physics World*, 14(1):33–38, January 2001.

[26] Alexander O Gogolin, Alexander A Nersesyan, and Alexei M Tsvelik. *Bosonization and strongly correlated systems*. Cambridge university press, 2004.

[27] Moshe Goldstein, Michel H. Devoret, Manuel Houzet, and Leonid I. Glazman. Inelastic microwave photon scattering off a quantum impurity in a josephson-junction array. *Phys. Rev. Lett.*, 110:017002, Jan 2013.

[28] Nicolas Gheeraert, Xin HH Zhang, Théo Sépulcre, Soumya Bera, Nicolas Roch, Harold U Baranger, and Serge Florens. Particle production in ultrastrong-coupling waveguide qed. *Physical Review A*, 98(4):043816, 2018.

[29] Alexander Cyril Hewson. *The Kondo problem to heavy fermions*. Number 2. Cambridge university press, 1997.

[30] Jun Kondo. Resistance minimum in dilute magnetic alloys. *Progress of theoretical physics*, 32(1):37–49, 1964.

[31] Thierry Giamarchi. *Quantum physics in one dimension*, volume 121. Clarendon press, 2003.

[32] Sergey Bravyi and David Gosset. Complexity of quantum impurity problems. *Communications in Mathematical Physics*, 356(2):451–500, 2017.

[33] Michael Schreiber, Sean S. Hodgman, Pranjal Bordia, Henrik P. Lüschen, Mark H. Fischer, Ronen Vosk, Ehud Altman, Ulrich Schneider, and Immanuel Bloch. Observation of many-body localization of interacting fermions in a quasirandom optical lattice. *Science*, 349(6250):842–845, August 2015.

[34] Jae yoon Choi, Sebastian Hild, Johannes Zeiher, Peter Schauß, Antonio Rubio-Abadal, Tarik Yefsah, Vedika Khemani, David A. Huse, Immanuel Bloch, and Christian Gross. Exploring the many-body localization transition in two dimensions. *Science*, 352(6293):1547–1552, June 2016.

[35] J. Smith, A. Lee, P. Richerme, B. Neyenhuis, P. W. Hess, P. Hauke, M. Heyl, D. A. Huse, and C. Monroe. Many-body localization in a quantum simulator with programmable random disorder. *Nature Physics*, 12(10):907–911, June 2016.

[36] P. Roushan, C. Neill, J. Tangpanitanon, V. M. Bastidas, A. Megrant, R. Barends, Y. Chen, Z. Chen, B. Chiaro, A. Dunsworth, A. Fowler, B. Foxen, M. Giustina, E. Jeffrey, J. Kelly, E. Lucero, J. Mutus, M. Neeley, C. Quintana, D. Sank, A. Vainsencher, J. Wenner, T. White, H. Neven, D. G. Angelakis, and J. Martinis. Spectroscopic signatures of localization with interacting photons in superconducting qubits. *Science*, 358(6367):1175–1179, December 2017.

[37] Kai Xu, Jin-Jun Chen, Yu Zeng, Yu-Ran Zhang, Chao Song, Wuxin Liu, Qiujiang Guo, Pengfei Zhang, Da Xu, Hui Deng, Keqiang Huang, H. Wang, Xiaobo Zhu, Dongning Zheng, and Heng Fan. Emulating many-body localization with a superconducting quantum processor. *Phys. Rev. Lett.*, 120:050507, Feb 2018.

[38] Alexander Lukin, Matthew Rispoli, Robert Schittko, M. Eric Tai, Adam M. Kaufman, Soonwon Choi, Vedika Khemani, Julian Léonard, and Markus Greiner. Probing entanglement in a many-body–localized system. *Science*, 364(6437):256–260, April 2019.

[39] D. Bluvstein, A. Omran, H. Levine, A. Keesling, G. Semeghini, S. Ebadi, T. T. Wang, A. A. Michailidis, N. Maskara, W. W. Ho, S. Choi, M. Serbyn, M. Greiner, V. Vuletić, and M. D. Lukin. Controlling quantum many-body dynamics in driven Rydberg atom arrays. *Science*, 371(6536):1355–1359, 2021.

[40] William Morong, Fangli Liu, Patrick Becker, KS Collins, Lei Feng, Antonis Kyprianidis, Guido Pagano, Tianyu You, AV Gorshkov, and Christopher Monroe. Observation of stark many-body localization without disorder. *Nature*, 599(7885):393–398, 2021.

[41] Qiujiang Guo, Chen Cheng, Zheng-Hang Sun, Zixuan Song, Hekang Li, Zhen Wang, Wenhui Ren, Hang Dong, Dongning Zheng, Yu-Ran Zhang, et al. Observation of energy-resolved many-body localization. *Nature Physics*, 17(2):234–239, 2021.

[42] Roman Kuzmin, Nitish Mehta, Nicholas Grabon, Raymond Mencia, and Vladimir E Manucharyan. Superstrong coupling in circuit quantum electrodynamics. *npj Quantum Information*, 5(1):1–6, 2019.

[43] Boris L. Altshuler, Yuval Gefen, Alex Kamenev, and Leonid S. Levitov. Quasiparticle lifetime in a finite system: A nonperturbative approach. *Phys. Rev. Lett.*, 78:2803–2806, Apr 1997.

[44] Paul Adrien Maurice Dirac. The quantum theory of the emission and absorption of radiation. *Proceedings of the Royal Society of London. Series A, Containing Papers of a Mathematical and Physical Character*, 114(767):243–265, 1927.

[45] D.M. Basko, I.L. Aleiner, and B.L. Altshuler. Metal–insulator transition in a weakly interacting many-electron system with localized single-particle states. *Annals of Physics*, 321(5):1126–1205, May 2006.

[46] Vadim Oganesyan and David A. Huse. Localization of interacting fermions at high temperature. *Phys. Rev. B*, 75:155111, Apr 2007.

[47] Maksym Serbyn, Z. Papić, and Dmitry A. Abanin. Local conservation laws and the structure of the many-body localized states. *Phys. Rev. Lett.*, 111:127201, Sep 2013.

[48] David A. Huse, Rahul Nandkishore, and Vadim Oganesyan. Phenomenology of fully many-body-localized systems. *Phys. Rev. B*, 90:174202, Nov 2014.

[49] Rahul Nandkishore and David A. Huse. Many-body localization and thermalization in quantum statistical mechanics. *Annual Review of Condensed Matter Physics*, 6(1):15–38, 2015.

[50] Dmitry A. Abanin, Ehud Altman, Immanuel Bloch, and Maksym Serbyn. Colloquium: Many-body localization, thermalization, and entanglement. *Rev. Mod. Phys.*, 91:021001, May 2019.

[51] Juan José García-Ripoll, Enrique Solano, and Miguel Angel Martin-Delgado. Quantum simulation of anderson and kondo lattices with superconducting qubits. *Physical Review B*, 77(2):024522, 2008.

[52] Aisling Johnson, Martin Blaha, Alexander E. Ulanov, Arno Rauschenbeutel, Philipp Schneeweiss, and Jürgen Volz. Observation of collective superstrong coupling of cold atoms to a 30-m long optical resonator. *Phys. Rev. Lett.*, 123:243602, Dec 2019.

[53] Michel H Devoret and Robert J Schoelkopf. Superconducting circuits for quantum information: an outlook. *Science*, 339(6124):1169–1174, 2013.

[54] Alexandre Blais, Steven M Girvin, and William D Oliver. Quantum information processing and quantum optics with circuit quantum electrodynamics. *Nature Physics*, 16(3):247–256, 2020.

[55] Philip Krantz, Morten Kjaergaard, Fei Yan, Terry P Orlando, Simon Gustavsson, and William D Oliver. A quantum engineer's guide to superconducting qubits. *Applied Physics Reviews*, 6(2):021318, 2019.

[56] Morten Kjaergaard, Mollie E Schwartz, Jochen Braumüller, Philip Krantz, Joel I-J Wang, Simon Gustavsson, and William D Oliver. Superconducting qubits: Current state of play. *Annual Review of Condensed Matter Physics*, 11:369–395, 2020.

[57] Steven M Girvin. Superconducting qubits and circuits: Artificial atoms coupled to microwave photons. *Lectures delivered at Ecole d'Eté Les Houches*, 2011.

[58] Uri Vool and Michel Devoret. Introduction to quantum electromagnetic circuits. *International Journal of Circuit Theory and Applications*, 45(7):897–934, 2017.

[59] Michel H Devoret et al. Quantum fluctuations in electrical circuits. *Les Houches, Session LXIII*, 7(8):133–135, 1995.

[60] Brian David Josephson. Supercurrents through barriers. *Advances in Physics*, 14(56):419–451, 1965.

[61] Michael Tinkham. *Introduction to superconductivity*. Courier Corporation, 2004.

[62] R. M. Foster. A reactance theorem. *The Bell System Technical Journal*, 3(2):259–267, 1924.

[63] David M Pozar. *Microwave engineering; 3rd ed.* Wiley, Hoboken, NJ, 2005.

[64] Jens Koch, M Yu Terri, Jay Gambetta, Andrew A Houck, David Isaac Schuster, Johannes Majer, Alexandre Blais, Michel H Devoret, Steven M Girvin, and Robert J Schoelkopf. Charge-insensitive qubit design derived from the cooper pair box. *Physical Review A*, 76(4):042319, 2007.

[65] Irinel Chiorescu, Y Nakamura, CJP Ma Harmans, and JE Mooij. Coherent quantum dynamics of a superconducting flux qubit. *Science*, 299(5614):1869–1871, 2003.

[66] Fei Yan, Simon Gustavsson, Archana Kamal, Jeffrey Birenbaum, Adam P Sears, David Hover, Ted J Gudmundsen, Danna Rosenberg, Gabriel Samach, Steven Weber, et al. The flux qubit revisited to enhance coherence and reproducibility. *Nature communications*, 7(1):1–9, 2016.

[67] Vladimir E Manucharyan, Jens Koch, Leonid I Glazman, and Michel H Devoret. Fluxonium: Single cooper-pair circuit free of charge offsets. *Science*, 326(5949):113–116, 2009.

[68] Long B. Nguyen, Yen-Hsiang Lin, Aaron Somoroff, Raymond Mencia, Nicholas Grabon, and Vladimir E. Manucharyan. High-coherence fluxonium qubit. *Phys. Rev. X*, 9:041041, Nov 2019.

[69] Aaron Somoroff, Quentin Ficheux, Raymond A Mencia, Haonan Xiong, Roman V Kuzmin, and Vladimir E Manucharyan. Millisecond coherence in a superconducting qubit. *arXiv preprint arXiv:2103.08578*, 2021.

[70] L. Frunzio, A. Wallraff, D. Schuster, J. Majer, and R. Schoelkopf. Fabrication and characterization of superconducting circuit qed devices for quantum computation. *IEEE Transactions on Applied Superconductivity*, 15(2):860–863, 2005.

[71] Chen Wang, Christopher Axline, Yvonne Y Gao, Teresa Brecht, Yiwen Chu, Luigi Frunzio, MH Devoret, and Robert J Schoelkopf. Surface participation and dielectric loss in superconducting qubits. *Applied Physics Letters*, 107(16):162601, 2015.

[72] GJ Dolan. Offset masks for lift-off photoprocessing. *Applied Physics Letters*, 31(5):337–339, 1977.

[73] T. Weißl, B. Küng, E. Dumur, A. K. Feofanov, I. Matei, C. Naud, O. Buisson, F. W. J. Hekking, and W. Guichard. Kerr coefficients of plasma resonances in josephson junction chains. *Phys. Rev. B*, 92:104508, Sep 2015.

[74] DM Basko and Frank WJ Hekking. Disordered josephson junction chains: Anderson localization of normal modes and impedance fluctuations. *Physical Review B*, 88(9):094507, 2013.

[75] David Gunnarsson, Juha-Matti Pirkkalainen, Jian Li, Gheorghe Sorin Paraoanu, Pertti Hakonen, Mika Sillanpää, and Mika Prunnila. Dielectric losses in multi-layer josephson junction qubits. *Superconductor Science and Technology*, 26(8):085010, 2013.

[76] Amir O Caldeira and Anthony J Leggett. Influence of dissipation on quantum tunneling in macroscopic systems. *Physical Review Letters*, 46(4):211, 1981.

[77] Moein Malekakhlagh, Alexandru Petrescu, and Hakan E. Türeci. Cutoff-free circuit quantum electrodynamics. *Phys. Rev. Lett.*, 119:073601, Aug 2017.

[78] KA Matveev, AI Larkin, and LI Glazman. Persistent current in superconducting nanorings. *Physical review letters*, 89(9):096802, 2002.

[79] Gianluca Rastelli, Ioan M Pop, and Frank WJ Hekking. Quantum phase slips in josephson junction rings. *Physical Review B*, 87(17):174513, 2013.

[80] Xu Han, Chang-Ling Zou, and Hong X. Tang. Multimode strong coupling in superconducting cavity piezoelectromechanics. *Phys. Rev. Lett.*, 117:123603, Sep 2016.

[81] Lev S. Bishop, Eran Ginossar, and S. M. Girvin. Response of the strongly driven jaynes-cummings oscillator. *Phys. Rev. Lett.*, 105:100505, Sep 2010.

[82] M. Houzet and L. I. Glazman. Critical fluorescence of a transmon at the schmid transition. *Phys. Rev. Lett.*, 125:267701, Dec 2020.

[83] Amir Burshtein, Roman Kuzmin, Vladimir E. Manucharyan, and Moshe Goldstein. Photon-instanton collider implemented by a superconducting circuit. *Phys. Rev. Lett.*, 126:137701, Mar 2021.

[84] R. Kuzmin, N. Grabon, N. Mehta, A. Burshtein, M. Goldstein, M. Houzet, L. I. Glazman, and V. E. Manucharyan. Inelastic scattering of a photon by a quantum phase slip. *Phys. Rev. Lett.*, 126:197701, May 2021.

[85] Yvonne Y Gao, Brian J Lester, Kevin S Chou, Luigi Frunzio, Michel H Devoret, Liang Jiang, SM Girvin, and Robert J Schoelkopf. Entanglement of bosonic modes through an engineered exchange interaction. *Nature*, 566(7745):509–512, 2019.

[86] Connor T. Hann, Chang-Ling Zou, Yaxing Zhang, Yiwen Chu, Robert J. Schoelkopf, S. M. Girvin, and Liang Jiang. Hardware-efficient quantum random access memory with hybrid quantum acoustic systems. *Phys. Rev. Lett.*, 123:250501, Dec 2019.

[87] Lov K. Grover. A fast quantum mechanical algorithm for database search. In *Proceedings of the Twenty-Eighth Annual ACM Symposium on Theory of Computing*, STOC '96, page 212–219, New York, NY, USA, 1996. Association for Computing Machinery.